



31st Annual European Meeting on Atmospheric Studies by Optical Methods

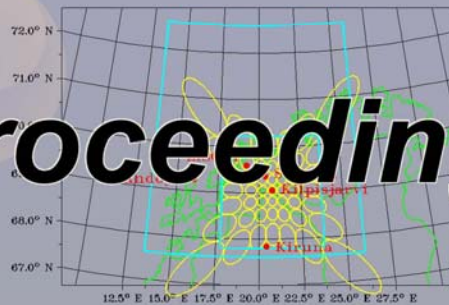


Jointly with 1st International Riometer Workshop



22nd to 28th of August 2004

Proceedings



Ambleside, The Lake District, UK



Preface

The 31st Annual European Meeting on Atmospheric Studies by Optical Methods was held in Ambleside in the Lake District in north-west England on 23-26 August 2004. The meeting had 41 attendees and 51 contributors. Of the 56 scientific contributions, there were 40 oral presentations and 16 posters. The range of topics was diverse, including history, in-situ and remote optical observations, artificially stimulated optical emissions, riometry, modeling, calibration and the latest technical developments. In addition, the conference was not limited to the study of the Earth's atmosphere and near space environment only. As usual, the conference proceeded in a friendly atmosphere culminating with most attendees participating actively in the Barn Dance. The 31st Annual Optical Meeting had three unique features. First, it was combined with the 1st International Riometer Workshop in order to broaden the scope and provide an opportunity for the different communities to get together. A major outcome was the Global Riometer Array initiative (GLORIA), where global riometer data will be shared via a single data base. Second, the 32nd Annual Optical Meeting was voted by the participants, as is traditional, to meet off the European continent for the first time in the meeting's history. Friends from the University of Western Ontario in London, Canada, will host the 2005 meeting. Third, with extraordinary forward planning, the 33rd Annual Optical Meeting will take place at the Swedish Institute of Space Physics in Kiruna, northern Sweden in 2006. In addition, having got the ball rolling, the 2nd International Riometer Workshop will be hosted by the University of Calgary and will meet in Canada in 2006. The long, and almost unbroken, series of Annual Optical Meetings is vibrant and shows little sign of ever stopping. We hope this remains the case. The organizers of the combined 2004 meetings thank all those who participated, without whom the meeting could not have been the success it was.



M.J. Kosch
Communication Systems
Lancaster University
United Kingdom

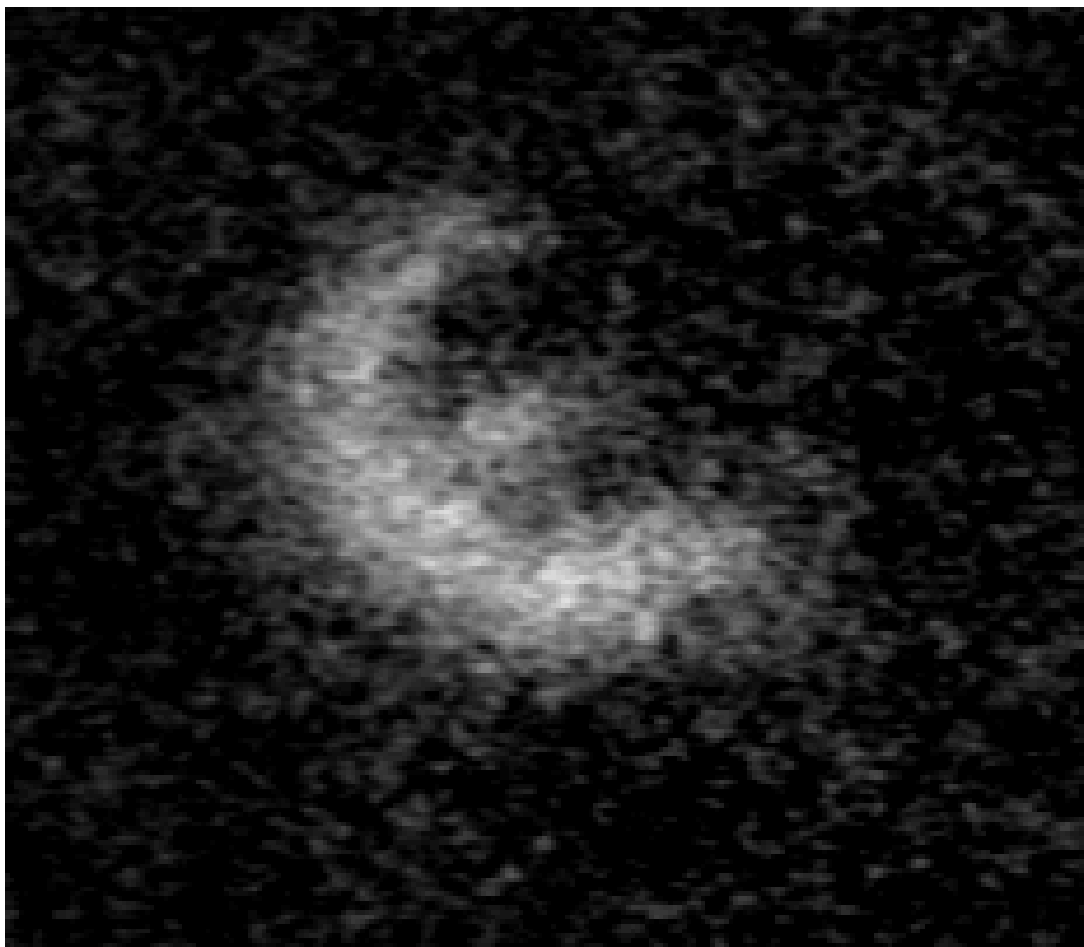
December 2005

31AM Group Photograph



Sky-painting produces the world's first

EURORA



This unique artificial aurora formation was unexpectedly generated by the EISCAT super-Heater, located at 69.59° N and 19.23° E in northern Norway, operating at 630 MW effective radiated power, on 12 November 2001 at 16:41:20 UT with the beam tilted 9° south of vertical. The image wavelength is 557.7 nm and the integration time is 5 seconds. The altitude of the phenomenon is estimated to be ~ 220 km from bi-static triangulation.

Annales Geophysicae Special Issue

The following articles appeared in the Volume 23, Number 5, 2005 special issue of Annales Geophysicae:

1. Preface "Atmospheric studies by optical methods"

Kosch, M. J. and Honary, F.

Page(s) 1521-1521. SRef-ID: 1432-0576/ag/2005-23-1521

2. World first complex optical instrumental observations of aurora in the Arctic in 1899-1900

Chernouss, S. A. , Starkov, G. V., and Yevlashin, L. S.

Page(s) 1523-1531. SRef-ID: 1432-0576/ag/2005-23-1523

3. Pc5 modulation of high energy electron precipitation: particle interaction regions and scattering efficiency

Spanswick, E. , Donovan, E., and Baker, G.

Page(s) 1533-1542. SRef-ID: 1432-0576/ag/2005-23-1533

4. Correlation between cosmic noise absorption and VHF coherent echo intensity

Makarevitch, R. A. and Honary, F.

Page(s) 1543-1553. SRef-ID: 1432-0576/ag/2005-23-1543

5. Comparison between CNA and energetic electron precipitation: simultaneous observation by Poker Flat Imaging Riometer and NOAA satellite

Tanaka, Y. -M. , Ishii, M., Murayama, Y., Kubota, M., Mori, H., Yamamoto, M. -Y., Kadokura, A., Lummerzheim, D., Desrochers, J., and Evans, D. S.

Page(s) 1555-1563. SRef-ID: 1432-0576/ag/2005-23-1555

6. Zonal wave numbers 1-5 in planetary waves from the TOMS total ozone at 65 S

Grytsai, A. , Grytsai, Z., Evtushevsky, A., Milinevsky, G., and Leonov, N.

Page(s) 1565-1573. SRef-ID: 1432-0576/ag/2005-23-1565

7. Effects of D-region RF heating studied with the Sodankylä Ion Chemistry model

Enell, C. -F. , Kero, A., Turunen, E., Ulich, Th., Verronen, P. T., Seppälä, A., Marple, S., Honary, F., and Senior, A.

Page(s) 1575-1583. SRef-ID: 1432-0576/ag/2005-23-1575

8. Artificial optical emissions at HAARP for pump frequencies near the third and second electron gyro-harmonic

Kosch, M. J. , Pedersen, T., Hughes, J., Marshall, R., Gerken, E., Senior, A., Sentman, D., McCarrick, M., and Djuth, F. T.

Page(s) 1585-1592. SRef-ID: 1432-0576/ag/2005-23-1585

9. The red-sky enigma over Svalbard in December 2002

Sigernes, F. , Lloyd, N., Lorentzen, D. A., Neuber, R., Hoppe, U. -P., Degenstein, D., Shumilov, N., Moen, J., Gjessing, Y., Havnes, O., Skartveit, A., Raustein, E., Ørbæk, J. B., and Deehr, C. S.

Page(s) 1593-1602. SRef-ID: 1432-0576/ag/2005-23-1593

10. The red sky enigma over Svalbard in December 2002: a model using polar stratospheric clouds

Lloyd, N. D. , Degenstein, D. A., Sigernes, F., Llewellyn, E. J., and Lorentzen, D. A.

Page(s) 1603-1610. SRef-ID: 1432-0576/ag/2005-23-1603

11. Relative drift between black aurora and the ionospheric plasma

Blixt, E. M. , Kosch, M. J., and Semeter, J.

Page(s) 1611-1621. SRef-ID: 1432-0576/ag/2005-23-1611

12. Variations of auroral hydrogen emission near substorm onset

Borovkov, L. P. , Kozelov, B. V., Yevlashin, L. S., and Chernouss, S. A.

Page(s) 1623-1635. SRef-ID: 1432-0576/ag/2005-23-1623

Other Publications

The following articles appeared elsewhere:

1. Low-cost multi-band ground-based imaging of the aurora

Syrjasuo, M. T., Jackel, B. J., Donovan, E. F., Trondsen, T. S., and Greffen, M.

Proceedings SPIE, Volume 5901, Page(s) 113-123, Solar Physics and Space Weather Instrumentation, Editors: Fineschi, S., and Viereck, R. A., 2005

2. Auroral optical emissions related to imaging riometer observations

Stoker, P. H., and Bijker, J.

South African Journal of Science, Volume 101, Number 5/6, Page(s) 281-284, May/June 2005

3. OSIRIS Observations of Mesospheric OH A²Σ⁺-X²Π Resonance Emissions

Degenstein, D. A., Gattinger, R. L., Llewellyn, E. J., and Lloyd, N. D.

Submitted to Journal of Geophysical Research, 2005

Cover Image Annales Geophysicae May 2005 special issue

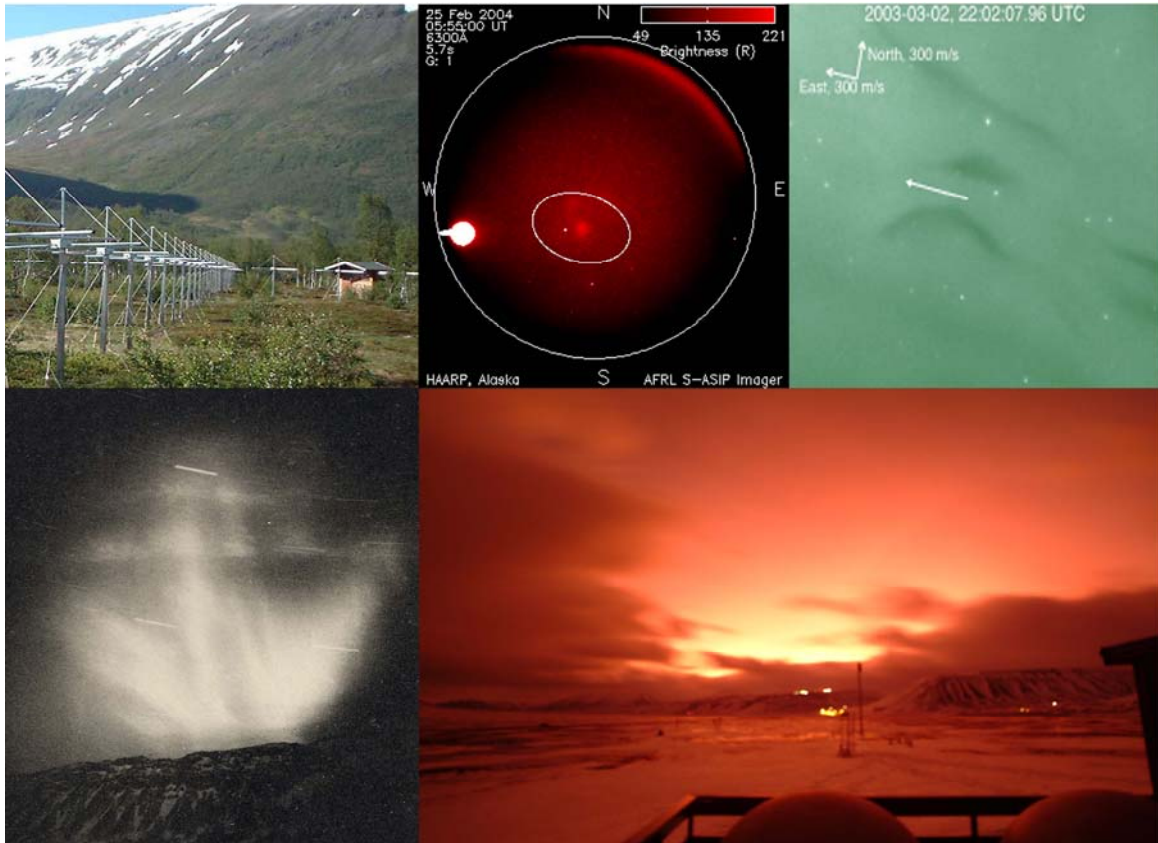


Figure caption: (1) Top left: The Mill's cross antenna array of the new digital Advanced Rio-Imaging Experiment in Scandinavia (ARIES) located near EISCAT in northern Norway. (2) Top middle: An artificial optical emission at 630 nm generated by the HAARP facility in Alaska on 25/02/2004 with the pump beam overlaid. The pump frequency was close to the second electron gyro-harmonic. A natural arc and the moon are also visible. (3) Top right: A TV optical image of black aurorae in a diffuse background taken on 02/03/2003. The EISCAT ionospheric plasma flow vector is overlaid. (4) Bottom left: The first auroral photograph obtained from the Spitzbergen Archipelago in 1899 by the Russian-Swedish expedition. (5) Bottom right: The Red Sky Enigma on 06/12/2002 from Longyearbyen, Svalbard. The phenomenon was caused by two-stage scattering of sunlight by polar stratospheric clouds.

31AM Proceedings

The following papers are published within the 31AM proceedings:

1. Height triangulation of artificial optical emissions in the F-layer
Ashrafi, M., Kosch, M. J., and Kaila, K.
Page(s) 8-16
2. The Novel Programmable Riometer for in-depth Ionospheric And Magnetospheric ObservationS (PRIAMOS) Using Direct Sampling DSP Techniques
Dekoulis, G., and Honary, F.
Page(s) 17-22
3. Two New Approaches to Spatial Interpolation with Inherent Sidelobe Suppression for Imaging Riometers
Grill, M., Senior, A., and Honary, F.
Page(s) 23-36
4. Calibration of TV all-sky data by simultaneous observations of scanning photometer
Kozelov, B. V.
Page(s) 37-41
5. Irregular pulsations in simultaneous TV, IRIS and VLF observations
Kozelov, B. V., Titova, E. E., Manninen, J., Honary, F., Marple, S., and Turunen, T.
Page(s) 42-49
6. Aurora, currents and particle dynamics in the inner magnetosphere: case study of multiple-onset substorm of March 12, 1991
Lazutin, L., Kozelova, T., Danielides, M. A., Meredith, N., Kozelov, B., Jussila, J., and Korth, A.
Page(s) 50-72
7. Aurora optical emissions related to imaging riometer observations
Stoker, P. H., and Bijker, J.
Page(s) 73-82
8. All-Sky camera network management of Finnish Meteorological Institute
Sukuvaara, T., Mattanen, J. and Mäkinen, S.
Page(s) 83-94

Height triangulation of artificial optical emissions in the F-layer

M. Ashrafi and M. J. Kosch

Department of Communications Systems, Lancaster University, Lancaster, LA1-4WA, UK

K. Kaila

Department of Physical Sciences, University of Oulu, Oulu, FIN-90570, Finland

Abstract.

Using the EISCAT high gain high frequency (HF) Heating facility located in northern Scandinavia (69.59° N, 19.23° E), HF-induced artificial auroral emissions can be produced at ionospheric F-region altitudes. On 12th November 2001, the EISCAT Heating facility, pumping with O-mode at 5.423 MHz and 550 MW effective radiative power (ERP), produced artificial optical rings which appeared immediately at pump-on and collapsed into blobs after ~ 60 s whilst descending in altitude. Observations were made using cameras in two different locations, one looking into the magnetic zenith over EISCAT recording in white-light, and the other pointing to the local zenith ~ 50 km from EISCAT in 630.0 and 557.7 nm (Skibotn, 69.35° N, 20.36° E). The altitudes of the initial optical ring and steady-state blob have been estimated by height triangulation. The change in height of all the optical structures during each Heater on cycle has been calculated using two-dimensional cross-correlation of the bi-static images. Consistent descent of the optical signature is similar to the lowering of other effects from ionospheric heating such as the EISCAT UHF radar ion line enhancements and stimulated electromagnetic emissions. We describe the details of the height triangulation technique used.

1 Introduction

Accelerated electrons resulting from ionospheric pumping with high frequency (HF) high power radio waves can cause excitation of the atomic oxygen and lead to the artificial green (557.7 nm) and red line (630.0 nm) emissions in the F layer. The phenomena has been observed at low and middle latitudes, for example at Arecibo (Sipler et al., 2001; Bernhardt et al., 1988, 1989), Platteville (Haslett and Megill, 1974) and in Russia at the SURA facility (Bernhardt et al., 1991), for a long time. There was no report of such observations at high latitudes until recently when observations of artificial optical emissions were made in Scandinavia and Alaska (Brändström et al., 1999; Kosch et al., 2000; Leyser et al., 2000; Pedersen and Carlson, 2001; Gustavsson et al., 2001). The phenomenon occurs at altitudes near the reflection height of the HF pump wave where electrons accelerated by HF-driven electrostatic waves to high energies propagate out of the interaction region up and down the magnetic field lines (Bernhardt et al., 1988). The accelerated electrons' energy is lost by inelastic collisions with the neutral atmosphere to excite neutrals such as the 1D and 1S states of atomic oxygen. The red-line emission at 630.0 nm and green-line emission at 557.7 nm are the two brightest stimulated optical emissions during ionospheric heating experiments which

result from inelastic collisions of accelerated electrons with energies higher than 1.96 eV and 4.17 eV, respectively. There have been several attempts in the past to estimate the height of the artificial optical emission (Brändström et al., 1999; Gustavsson et al., 2001). This is important in understanding the electron acceleration excitation mechanisms and accelerated electron energy spectrum resulting in the artificial aurora. In this paper we present observations of the ionospheric modification experiment on 12 November 2001 at the EISCAT Heating facility in northern Scandinavia and describe a triangulation technique using images from two cameras separated by ~ 50 km in order to estimate the height of the optical emission throughout the heating experiment.

2 Experimental observations

On 12th November 2001, the EISCAT Heater was transmitting O-mode waves at 5.423 MHz operating at 550 MW ERP with a 2 min. on, 2 min. off cycle with the pump beam pointed 9° south of vertical in the first half of the experiment (15:05 - 16:55 UT). During the second half (16:57 - 20:00 UT), the Heater beam was scanning between 3° and 15° south of vertical in 3° steps. The pump beam width is $\sim 7^\circ$ throughout and magnetic zenith is 12.8° south of vertical. Optical observations were made simultaneously from two stations ~ 50 km apart. The DASI (Digital All-Sky Imager) camera (Kosch et al., 1998) with a 50° field of view was located at Skibotn, Norway (69.35° N and 20.36° E), pointing vertically using narrow-band interference filters at 557.7 or 630.0 nm. The other camera situated at Ramfjordmoen (69.59° N and 19.23° E) was looking along the magnetic field line direction with a 50° field of view, recording in white light. DASI used an integration time of 5 s for 557.7 nm and 10 s for 630.0 nm whereas the Ramfjordmoen camera used a 13 seconds cycle. The optical signature produced by the pump waves was a ring shaped structure at the start of the Heater on period which collapsed into a blob after ~ 60 s

of heating. Intensities up to ~ 100 and ~ 300 Rayleighs in 630.0 nm were observed for the ring and blob structure artificial aurora, respectively. For details of the observation refer to Kosch et al. (2004).

3 Height triangulation method

Multi-station observations of auroral emissions and the application of height triangulation in estimating the location of the emission is a well known, long standing technique (Störmer, London, 1955). However, by knowing the special distribution of the emission region as additional information, computer tomography is another method used to estimate the height of the emissions (Solomon et al., 1984; Semeter et al., 1999; Gustavsson et al., 2001). Tomographic reconstruction generally requires more than two points of view, which were not available during our experiment. In our case, we have used the images from two optical stations at Skibotn and Ramfjordmoen to estimate the height of the artificial auroral emissions produced by the EISCAT high gain Heater. The green line data from the DASI camera together with the white light recordings of the Ramfjordmoen camera have been used to estimate the height of the emissions. We assume that the vertical extent of the artificial aurora is limited, or equivalently the height triangulation is focusing on the region of greatest intensity, i.e. near the bottom of the forms. The O(1 S) 557.7 nm emission is suitable for studying temporal variations, due to its short radiative lifetime (~ 0.7 s) compared to the brighter O(1 D) 630.0 nm emission with ~ 30 s effective lifetime in the F-layer (Gustavsson et al., 2001). In addition, the white light data from the Ramfjordmoen camera is dominated by the 557.7 nm emission because of the spectral response of the camera, therefore it is reasonable to compare the white light images with the DASI green line data.

Star field images, computed from a star catalogue and mapped down onto the data images, have been used to cor-

rect the lens distortion for both cameras (Duffet-Smith, Cambridge, 1990) and calculate each camera's exact position and pointing direction. An additional transformation has been applied to the Ramfjordmoen camera as it is pointing toward magnetic zenith over EISCAT (Azimuth 183° , Elevation 77.2°) and so it is not co-aligned with the line to the centre of the Earth, i.e. the spherical coordinate system origin. Second order corrections have been made in the image x and y directions in order to compensate for the discrepancies between the recorded images and the star map, i.e. lens distortion, which is typical for wide-aperture night-vision imaging systems. However, a better accuracy is achieved for more central image pixels rather than those close to the edge of the image. Since the optical structures are located mostly away from the edge of the field of view, there is no significant error introduced into the height triangulation. The same corrections have to be made to all the images from each camera.

In order to eliminate the effect of the unwanted background signal, which also includes the stars in case of the Ramfjordmoen camera recording in white light, background subtraction and filtering is required. Figure 1 shows the DASI and Ramfjordmoen camera images before (1-a) and after (1-b) filtering and background subtraction. By subtracting the average of five successive images before each Heater on cycle from any image during the same cycle, a clear picture of the artificial emissions is obtained (Fig. 1-b). In addition, a 5×5 median filter has been applied to the images to eliminate the background noise and residual stars due to their motion. The integration and cycle times of the cameras are different, therefore synchronization is required. The Ramfjordmoen camera images have been subjected to linear time interpolation in order to synchronize them with the DASI data. The difference in time between the real camera image and the required synchronized image is only a few seconds, therefore linear interpolation is a good approximation in order to produce the desired image. In addition, to perform the height triangulation, it is essential to have the synchronized

images in a common coordinate system. Geographic coordinates are well suited to this purpose. In order to perform this transformation, first the image is converted into altitude and azimuth angles or horizon coordinates. Then, by choosing a certain height, the image can be transformed to geographic coordinates. Figure 1-c shows the converted images in geographic coordinates for both cameras at 220 km altitude.

Finally, the linear 2-dimensional cross-correlation coefficient between the corresponding images in geographic coordinates from the different platforms has been calculated within a common geographic area between 17.3° and 20.2° in Longitude and 68.6° and 69.6° in Latitude. Figure 2 shows the superimposed images from the two cameras assuming three different heights. Panel (2-a) is for 320 km altitude, giving a cross-correlation of ~ 0.05 . Panel (2-b) is for the highest correlation of ~ 0.7 at 220 km. The ring-shaped structures of the artificial aurora from both cameras are perfectly overlapped. Panel (2-c) is for 170 km altitude with a correlation coefficient of ~ 0.1 . The best correlation is achieved for the height which is most likely to be the real height of the brightest part of the optical emission. At this height, the apparent horizontal overlap of the ring structure of the artificial aurora, observed from the two different platforms, is optimized. The cross-correlation coefficient has been calculated for a range of heights in the vicinity of the pump wave reflection altitude. Using EISCAT UHF radar electron density profiles, the reflection height of the Heater pump wave has been estimated, which is ~ 220 - 235 km for 15-17 UT (Kosch et al., 2004). The small circles in Figure 2 represent the projection of the magnetic field line at Ramfjordmoen in geographic coordinates. The corresponding height for each point has been marked in kilometers.

Figure 3 represents the height vs. cross-correlation coefficient for different intervals over one of the Heater on cycles starting at 16:57:00 UT which lasts for 2 minutes. The correlation coefficient vs. height is shown for 40, 60, 80 and 100 seconds after the Heater on from top to bottom, respec-

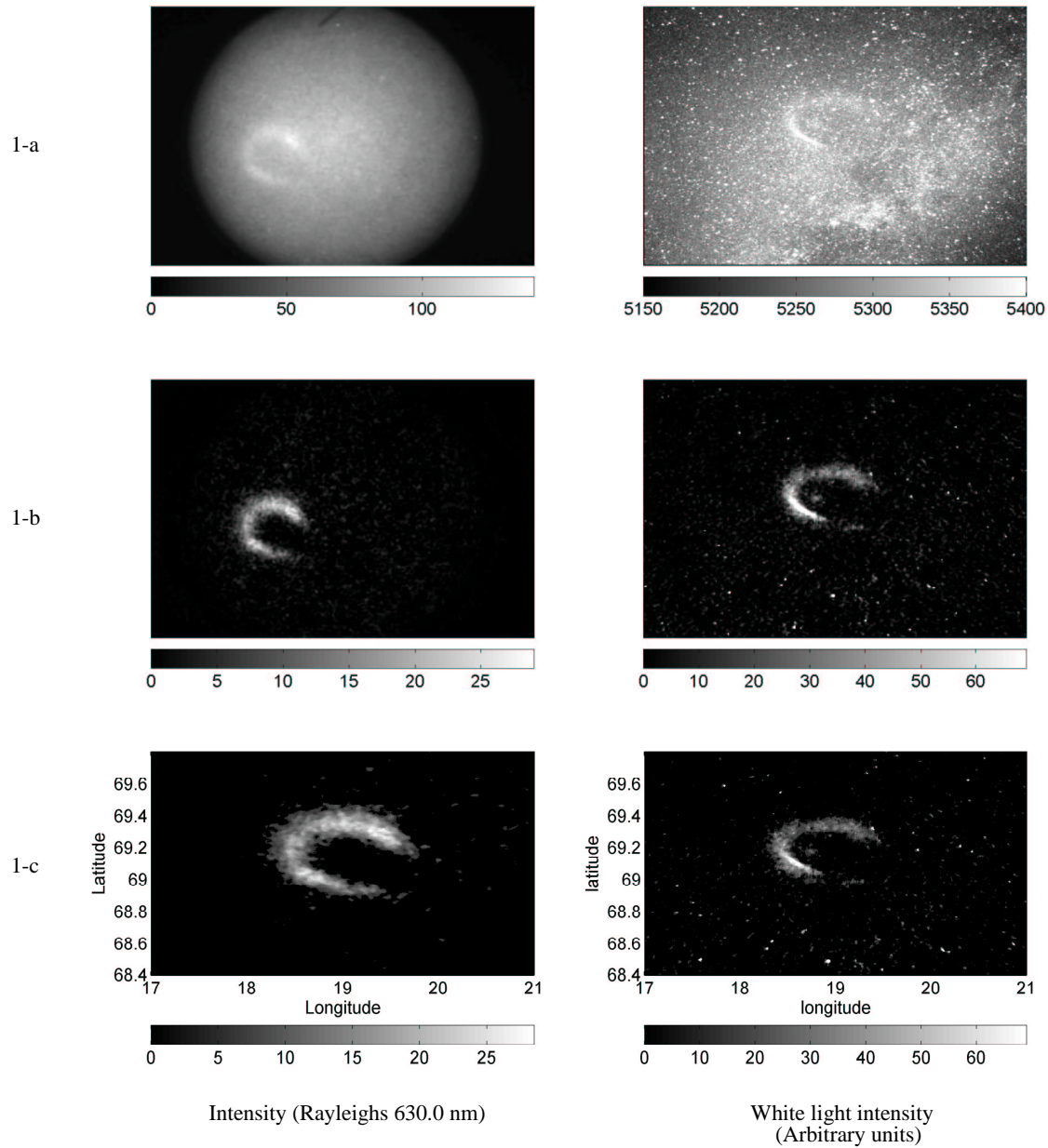


Fig. 1. The left column shows DASI images. From top to bottom is the raw, background subtracted and filtered image, and image projection into geographic coordinates for 220 km altitude. The images are calibrated in Rayleighs for 630.0 nm. The column on the right is the same sequence of images from the Ramfjordmoen camera in white light. In this case the red line emission data at 630.0 nm is used for demonstration purposes only and the height triangulation analysis has been applied to green line data at 577.7 nm..

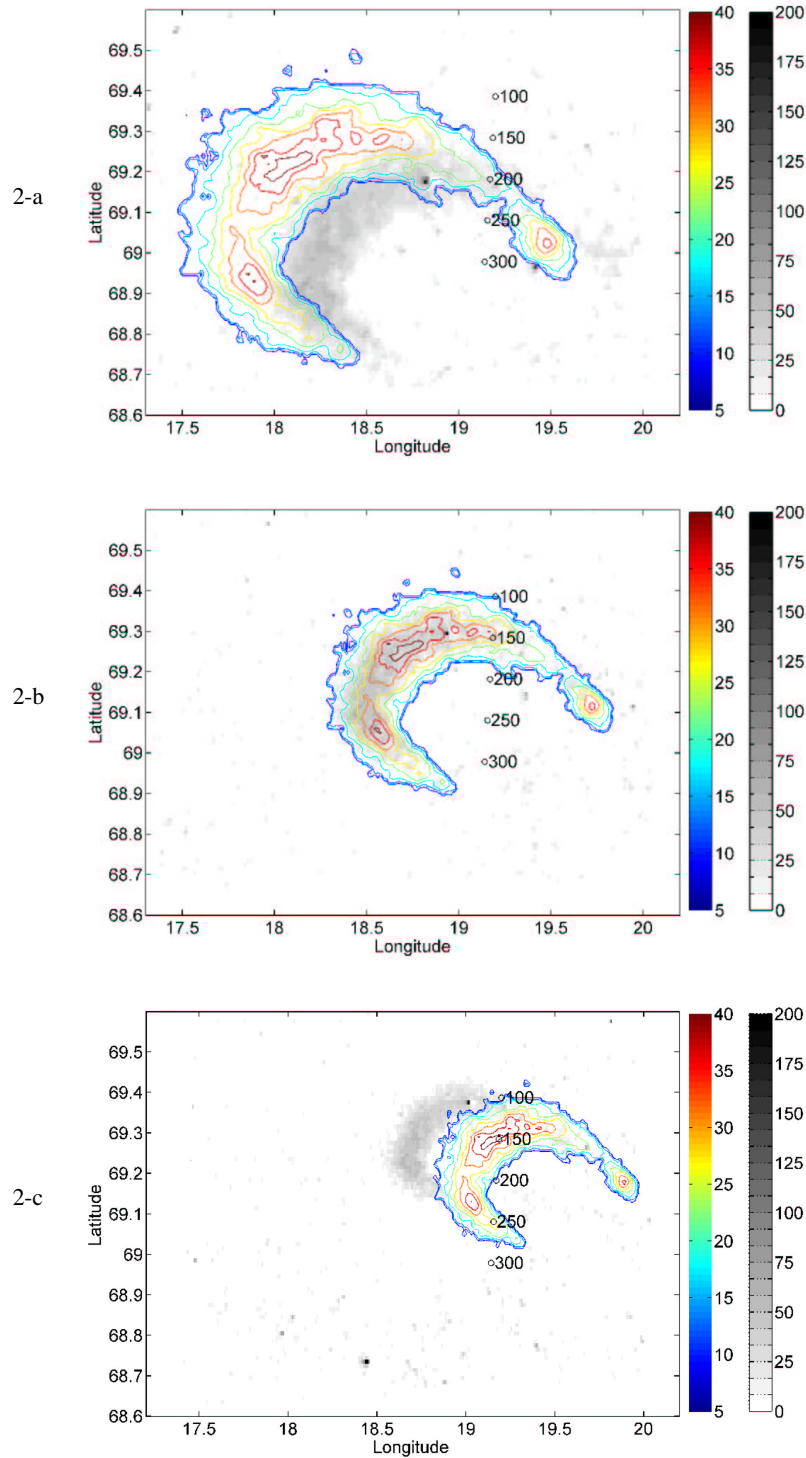


Fig. 2. Superimposed optical aurora from the DASI and Ramfjordmoen cameras at 16:25:10 UT projected in geographic coordinates assuming three different projection altitudes. The color contour plots are the optical annuli recorded by the DASI camera in green line emission (557.7 nm) overlaid on the gray scale images from the Ramfjordmoen camera in white light. Intensity is in arbitrary units. Panels a, b and c are for 320, 220 and 170 km altitudes, respectively. The small circles represent the projection of the magnetic field line through Ramfjordmoen for different altitudes.

tively. The points shown by asterixes are the corresponding cross-correlation coefficient for each two kilometer altitude step. The red curve is a second order polynomial fit to the points, the maximum of which is taken to be the maximum cross-correlation achieved for any given time. Therefore, the height of maximum correlation is considered to be the true equivalent height where the optical emissions come from assuming zero vertical extent. In the ideal case the cross-correlation for this altitude should be close to unity but considering the measurement uncertainty, lens distortion corrections, noise and other factors involved (e.g. vertical extent) this is not generally achievable.

The error associated with the height estimation is generated by uncertainties in the cross correlation, which is a result of height ambiguity or vertical extension, lens distortion, image noise, etc. and is expressed as the standard deviation of the correlation coefficient for each selected altitude. The uncertainty in height triangulation of the optical emission is obtained by simulation, i.e. the curve fit shown in Figure 3 is performed many times, varying the cross-correlation values for each selected altitude randomly within each value's standard deviation. The altitude error on average is ~ 4 -5 km.

4 Results and conclusion

The change in height of the brightest part of the optical emission has been calculated for Heater on cycles from 16:25 - 17:00 UT. Figure 4 shows the height triangulation results (asterixes) plotted on top of the EISCAT UHF radar backscatter power for 9 sequential Heater cycles. The intervals indicated by black lines show the Heater on cycles and the labels are radar zenith angles south of vertical. The general descent in height of the optical signature is consistent with the height variations of the EISCAT backscatter enhancements. These persistent ion line enhancements in the vicinity of the O-mode HF reflection altitude are the result of parametric decay of the pump electromagnetic wave in

vicinity of the O-mode reflection altitude into Langmuir and ion acoustic waves (Bernhardt et al., 1989; Stubbe et al., 1992; Djuth et al., 1994) and is commonly observed when pumping the ionosphere near an electron gyro-harmonic frequency (Kosch et al., 2004), e.g. 5.423 MHz corresponds to the 4th gyro-harmonic at 215 km altitude. The enhancements are only visible at angles close to the direction of the magnetic field line (Kosch et al., 2004). Therefore, in some of heater cycles there are no persistent ion line enhancements due to the radar look angle. The descent in altitude of the ion line data is a result of the descent of the pump wave's resonance region where the plasma frequency equals the pump frequency. Heating the lower F-layer plasma causes an increase in electron temperature (Rietveld et al., 2003) and decrease in electron recombination rate, thereby increasing the plasma density (Ashrafi et al., 2006). Electron density increases near the reflection point of the radio waves results in the descent of the reflection level of the pump wave.

The enhanced Langmuir waves accelerate electrons to supra-thermal velocities which then collide with the oxygen neutrals to produce 630.0 and 557.7 nm emissions. This is consistent with our height triangulation of the artificial optical emissions. The variation in height of the green line emission at 557.7 nm is similar to the temporal evolution in altitude of the ion line enhancements. The optical emission is being produced a few kilometers below the acceleration region, which is expected as the gas density increases at lower altitudes, making electron-neutral collisions more likely. The height difference between the ion-line enhancements and optical emissions on average is ~ 10 km, which is consistent with the night time mean free path between electron-atomic oxygen collisions of ~ 14 km at 210-220 km altitude (Gurevich, 1978).

The Ramfjordmoen camera was looking along the magnetic field line direction, therefore the recorded optical signature is the integration of all emissions distributed along the magnetic field line. This is because the optical aurora forms

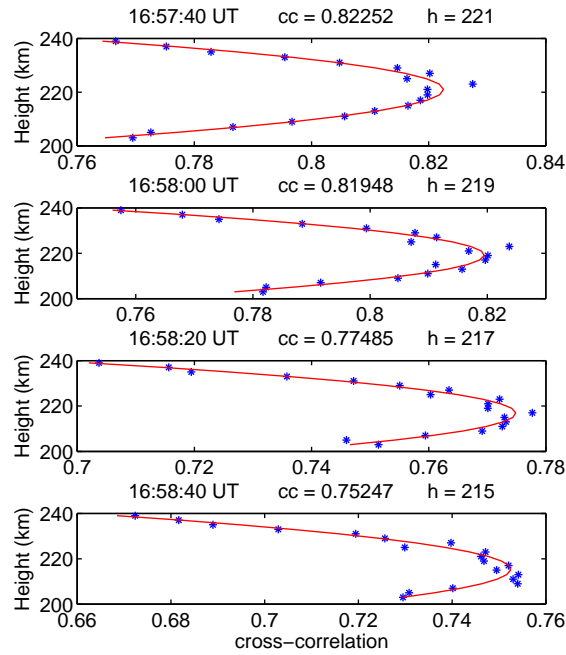


Fig. 3. The height vs. cross-correlation for the sequence of images with 20 seconds separation after the start of the Heater on cycle at 16:57:00 UT. The cross-correlation maximizes at a certain height for each time integration. The red curve indicates the 2nd order polynomial fit to the points, used to estimate the height of maximum cross-correlation. Time, maximum cross-correlation and the corresponding altitude are shown for each panel.

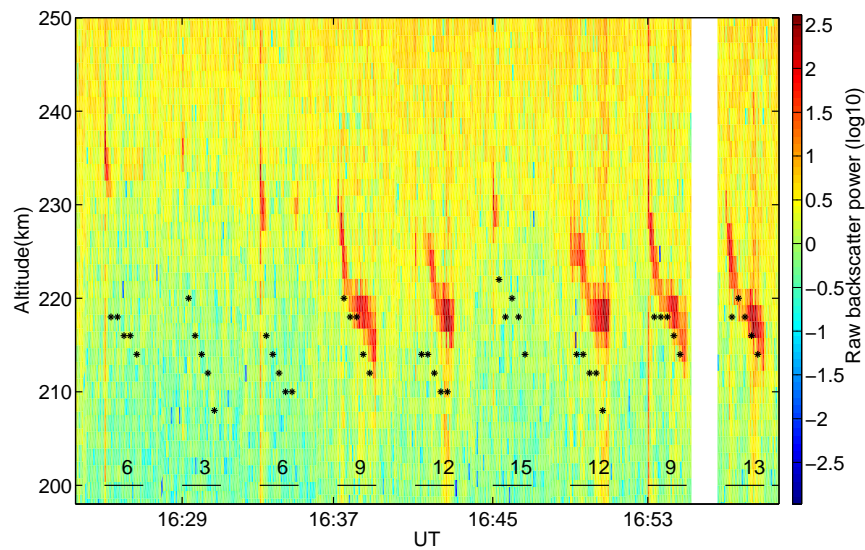


Fig. 4. Raw backscattered power from the EISCAT UHF radar shown in false color. The asterixes show the height triangulation of the optical artificial aurora at 557.7 nm. The intervals indicated by the lines are Heater on cycles and the labels are radar zenith angle south of vertical.

a cylinder above the pump wave reflection altitude parallel to the magnetic field line direction (Kosch et al., 2004). The apparent thickness of the partial ring in the Ramfjordmoen image is the real horizontal width of the structure. The DASI camera pointing towards local zenith ~ 50 km away recorded the column of artificial aurora at an oblique angle. This difference in the look directions leads to vertical extent ambiguity between the images from the two cameras and reduces the cross-correlation coefficient as a result. To properly estimate the vertical extent and altitude of the artificial aurora, a third camera would be needed, but this was not available at the time. The effect is visible in the DASI images where the optical ring recorded by DASI appears horizontally thicker compared to the Ramfjordmoen camera ring structure (Fig. 2). Using the apparent increased horizontal extension of optical signature in the DASI images compared to the Ramfjordmoen images, it is possible to estimate the vertical extent of the emission column by mapping the magnetic field line onto the images in geographic coordinates. For the example shown in Figure 2, the field aligned extension of the artificial aurora to first order is ~ 70 km which is consistent with Kosch et al. (2004).

References

- Ashrafi, M., Kosch, M. J., and Honary, F.: Heater-induced altitude descent of the EISCAT UHF ion line enhancements: observations and modelling, *Adv. Space Res.*, In press, 2006.
- Bernhardt, P. A., Duncan, L. M., and Tepley, C. A.: Artificial airglow excited by high-power radio waves, *Science*, 242, 1022–1027, 1988.
- Bernhardt, P. A., Tepley, C. A., and Duncan, L. M.: Airglow enhancements associated with plasma cavities formed during ionospheric heating experiments, *J. Geophys. Res.*, 94, 9071–9092, 1989.
- Bernhardt et al., P. A.: Excitation of artificial airglow by high power radio waves from the "SURA" ionospheric heating facility, *Geophys. Res. Lett.*, 18, 1477–1480, 1991.
- Brändström, B. U. E., Leyser, T. B., Steen, A., Rietveld, M. T., Gustavsson, B., Aso, T., and Ejiri, M.: Unambiguous evidence of HF pump-induced airglow at auroral latitudes, *Geophys. Res. Lett.*, 26, 3561, 1999.
- Djuth, F. T., Stubbe, P., Sulzer, M. P., Kohl, H., Rietveld, M. T., and Elder, J. H.: Altitude characteristics of plasma turbulence excited with the Tromsø superheater, *J. Geophys. Res.*, 99, 333–339, 1994.
- Duffet-Smith, P.: *Practical astronomy with your calculator*, Cambridge University Press, Cambridge, 1990.
- Gurevich, A. V.: *Nonlinear phenomena in the ionosphere*, Elsevier, North-Holland, 1978.
- Gustavsson, B., Sergienko, T., Rietveld, M. T., Honary, F., Steen, A., Brändström, B. U. E., Leyser, T. B., Aruliah, A. L., Aso, T., Ejiri, M., and Marple, S.: First tomographic estimate of volume distribution of HF-pump enhanced airglow emission, *J. Geophys. Res.*, 106, 29 105–29 124, 2001.
- Haslett, J. C. and McGill, L. R.: A model of enhanced airglow excited RF-radiation, *Radio Science*, 9, 1005–1019, 1974.
- Kosch, M. J., Rietveld, M. T., Hagfors, T., and Leyser, T. B.: High-latitude HF-induced airglow displaced equatorwards of the pump beam, *Geophys. Res. Lett.*, 27, 2817–2820, 2000.
- Kosch, M. J., Rietveld, M. T., Senior, A., McCrea, I., Kavanagh, A. J., Isham, B., and Honary, F.: Novel artificial optical annular structures in the high latitude ionosphere over EISCAT, *Geophys. Res. Lett.*, 31, L12 805, doi:10.1029/2004GL019713, 2004.
- Leyser, T. B., Gustavsson, B., Brändström, B. U. E., Honary, F., Å. Steen, Aso, T., Rietveld, M. T., and Ejiri, M.: Simultaneous measurements of high-frequency pump-enhanced airglow and ionospheric temperatures at auroral latitudes, *Adv. Polar Upper Atmos. Res.*, 14, 1–11, 2000.
- Pedersen, T. R. and Carlson, H. C.: First observations of HF heater produced airglow at the high frequency active aurora research program facility: Thermal excitation and spatial structuring, *Radio Sci.*, 36, 1013–1026, 2001.
- Rietveld, M. T., Kosch, M. J., Blagoveshchenskaya, N. F., Kornienko, V. A., Leyser, T. B., and Yeoman, T. K.: Ionospheric Electron Heating, Optical Emissions, and Striations Induced by Powerful HF Radio Waves at High Latitudes: Aspect Angle Dependence, *J. Geophys. Res.*, 108, 2/1–2/16,

doi:10.1029/2002JA009543, 2003.

Sipler, D. P., Enemark, E., and Biondi, M. A.: 6300-

A intensity variations produced by the Arecibo ionospheric modification experiment, *J. Geophys. Res.*, *77*, 4276–4280, 2001.

Störmer, C.: *The Polar Aurora*, Oxford University Press, London, 1955.

Stubbe, P., Kohl, H., and Rietveld, M. T.: Langmuir turbulence and ionospheric modification, *J. Geophys. Res.*, *97*, 6285–6297, 1992.

The Novel Programmable Riometer for in-depth Ionospheric And Magnetospheric ObservationS (PRIAMOS) Using Direct Sampling DSP Techniques

G. Dekoulis, F. Honary

Space Plasma Environment and Radio Science Group, Department of Communication Systems, Lancaster University, UK.

Abstract

This paper describes the feasibility study and simulation results for the unique multi-frequency, multi-bandwidth, Programmable Riometer for in-depth Ionospheric And Magnetospheric ObservationS (PRIAMOS) based on direct sampling digital signal processing (DSP) techniques. This novel architecture is based on sampling the cosmic noise wavefront at the antenna. It eliminates the usage of any intermediate frequency (IF) mixer stages (-6 dB) and the noise balancing technique (-3 dB), providing a minimum of 9 dB increase in performance. The DSP implements high-speed filtering and selects the appropriate centre frequencies and signal bandwidths. For the first time a riometer would automatically generate both the experimental and theoretical Quiet Day Curves (QDCs) and Absorption values. For the first time the full extent of Solar Radio Emissions (SREs Type III & IV) would be measured by a riometer, due to the receiver's programmable sliding gain range. The programmable auto-correlator integration time allows in-depth observation of the different magnetospheric and ionospheric events. Noise analysis was a crucial factor in selecting the appropriate components, since the received power signals are very low.

1. Introduction

A Riometer (Relative Ionospheric Opacity Meter for Extra-Terrestrial Electromagnetic Radiation) is a passive radio wave experiment inspired by radio astronomy techniques [1]. Such experiments require a low noise, high dynamic range, a low as possible minimum detectable signal (MDS) value and auto-calibrated receiver to measure the background cosmic noise received by Earth or another planet [2]. A vertical antenna with the main lobe in the direction of local zenith can detect these cosmic radio signals. Cosmic noise varies according to the Earth rotation, but remains constant for a repeated Local Sidereal Time.

There are two categories of riometers based on the number and phasing of the deployed antennas, namely widebeam and imaging riometers. Widebeam riometers have a single antenna above a ground plane. Typical operating frequencies are 27.6, 29.7, 29.9, 30, 32, 32.4, 35, 38.2 and 51.4 MHz and bandwidth of 15 to 250 KHz. The antenna is usually a broad-beam design of a vertical three element Yagi, two parallel horizontal dipoles or cross-dipole with a beamwidth in the region of 60°. Due to the benefits of the double polarisation the preferred antenna for this design is the cross-dipole. Riometer networks have been used in the past for co-ordinated experiments, e.g. auroral substorm measurements [3]. Single wide-beam riometers at different sites have been used to measure the moving absorption [4].

Several research centres have focused on studying absorption events in a smaller-scale by implementing antenna phased-array imaging riometers [5]-[7]. The University of Maryland, USA installed the first imaging system at the South Pole in 1988. The system uses 64 cross-dipoles tuned to 38.2 MHz. Butler matrices form 49 beams. The signals are distributed to seven receivers, and digitised using 8bits resolution. Imaging systems are divided into the square additive phased filled array and cross-correlated categories. The Lancaster University's Imaging Riometer for Ionospheric Studies (IRIS) [5] at Kilpisjarvi and Advanced Rio Imaging Experiment in Scandinavia (ARIES) [8] are an example of each category, respectively. Imaging systems, so far, use an analogue phase-steering network to produce narrow-beams scanning the ionosphere's D-region. Both the widebeam [9] and imaging systems [1] are built on the noise balancing technique of Fig. 1.

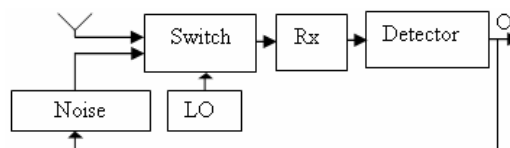


Fig. 1. Analogue Widebeam System using the Noise Balancing Technique.

The receiver switches between the antenna and the internal noise source. The switching frequency is derived from a low frequency local oscillator (LO). The

output voltage is at the switching frequency and proportional to the received power. The voltage difference between the noise source and signal determines the output's amplitude. The synchronous detector minimises the error by adjusting the noise source output. The balancing of the two signals causes the detector output to be proportional to the received signal. Based on the existing and planned systems list [6], the basic design has changed little over a long period. The systems reviewed have two main disadvantages; they are hardwired and rely on analogue electronics. Hardwired to perform specific functions restricts flexibility in terms of signal processing. Many boards are required with low reliability factors, high induced noise, temperature drift and regular calibrations. The existing systems spend from 0.125–0.5s every second calibrating the system using the noise balancing technique [5] and [2], respectively. This technique contributes to 3dB power loss.

Digital technology is rapidly replacing existing analogue systems [10]. DSP devices are unconditionally accurate, as accuracy is only determined by the size of the internal busses. The performance from device to device is identical since the tolerance of the components is the same. There is no temperature drift, thus, the noise balancing technique can be removed. The circuits are more reliable, consume less power and operate at higher speeds. DSP systems are reprogrammable and perform functions not possible with analogue circuits.

2. Receiver Design Study

There are 3 main receiver architectures depending on the position of the analogue-to-digital converter (ADC) in the system. These are the baseband (BB), IF and radio frequency (RF). From the feasibility study results the optimum solution was chosen. In 1994, the Watkins-Johnson company published its receivers' frequency plans [11]. The superheterodyne receiver [12] contains a filter and amplifier bank and two conversion stages. Each conversion stage has one LO, filtering and amplification. The conversion stage introduces thermal noise, unwanted frequency

components and leakage of the reference signal into the wanted IF signal. Similarly, using one conversion stage only, the 10.7MHz IF signal is obtained, which is then bandpass filtered (BPF) to 250KHz and sampled at 500KHz, as shown in Fig. 2. This architecture has been used in passive wave radio experiments before, but it suffers from high noise figure (NF), low dynamic range (DR), low output intercept point (OIP), there is minimum, if any, control over the analogue stages, low reliability factor, temperature drift and the calibration frequency is determined empirically. The system still relies on the usage of the noise balancing technique.

The ideal solution is the RF architecture of Fig. 3. The cosmic noise is sampled after the amplification and BPF stages. The incoming signal is centred at 38.2MHz and the ADC samples 2.5x the centre frequency. The system has a NF of 2.07dB, OIP > 25dBm, MDS = -118dBm and two-tone DR > 86dB. However, due to the high centre frequency, the digital finite impulse response (FIR) filtering was impossible in hardware and the signal processing results were poor.

By mutually excluding the other two techniques, the high-speed [13] direct conversion is the optimum solution [14]. The RF signal is translated to DC in one step, as in Fig. 4. It could also translate to a nonzero BB centre frequency and demodulate the signal into BB bitstreams within the same circuit.

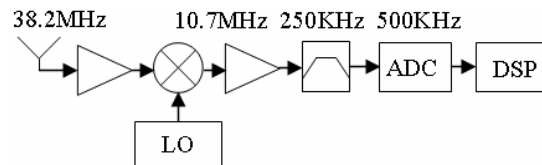


Fig. 2. IF Receiver Architecture Solution.

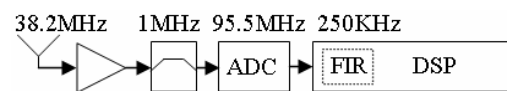


Fig. 3. RF Receiver Architecture Solution.

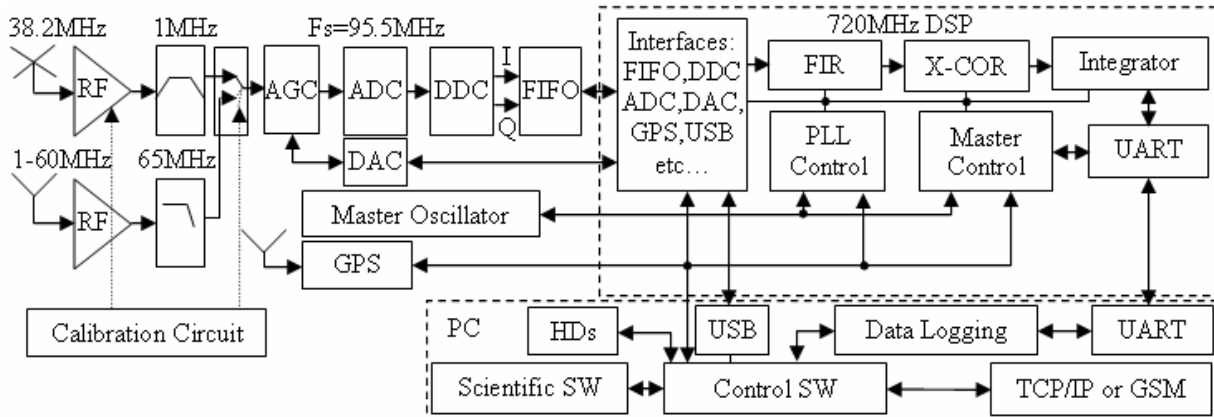


Fig. 4. The PRIAMOS Direct Conversion Solution.

3. The Novel PRIAMOS System

The following sections describe the peripheral hardware design, DSP design and scientific data processing of the proposed system.

3.1 Specifications

PRIAMOS features the following:

- Multi-Frequency (1-60MHz).
- Noise figure of 2.07dB.
- 14-bit ADC resolution.
- 87dB DR expandable to 175dB. Receiver saturation is avoided during Type III & IV SREs.
- Variable integration time for in-depth observation of events. Default is 1s.
- Multi-bandwidth (3KHz-4MHz). For this setup the analogue BPF sets it to a maximum value of 1 MHz.
- 0dB antenna transmission line losses.
- Reprogrammable on-board GPS chipset.
- The receiver can be reconfigured within seconds.
- Lengthy data logging or immediate host transfers.
- Automatic calculation of quiet day curves (QDCs) and Absorption Values.
- Fast prototyping for other Space Centre projects.
- Small, low cost, lightweight unit assembly.

3.2 System Description

The system is independent of the antenna and analogue front-end. For prototyping purposes, a circularly polarised crossed-dipole antenna is used, tuned to 38.2 MHz. It can electronically switch to a 1-60MHz input as well, although signals between 27-52MHz are used for space physics applications at HF and L-VHF. The noise balancing technique is removed. The digital receiver is continuously processing the input signal and exhibits improvement of 3dB, in terms of power levels.

The signal is pre-amplified by 23dB and wideband filtered to 5MHz. The signal is further bandpass filtered to 1MHz. The automatic gain controller (AGC) adjusts the voltage to a level suitable for the ADC to detect. The ADC samples at 95.5MHz, which is 2.5 times the input signal. Investigation was made whether the signal can be processed at RF by the DSP. The high center frequency, the sharp cut-off characteristics and the low stopband attenuation requirements impose the usage of a symmetrical FIR filter with roughly 5000 coefficients. Its implementation requires about 400 clock cycles to produce the first result, excessive amount of hardware resources and raises the system cost significantly.

A digital-down-converter (DDC) converts the signal to baseband, reduces the data rate by a factor of 256 and extracts the in-phase (I) and quadrature (Q) components of the signal. The signal is low-pass filtered to the

desired B. The data are buffered and matched FIR filtered in the DSP. The calculated power is integrated for 1s. The integrated values are logged for scientific analysis. The GPS receiver provides the pulse-per-second (PPS) signal, universal time (UT) for timestamping and location for the calculation of the theoretical QDC. The system automatically computes absorption by comparing the measured with the theoretical QDC.

3.3 Antenna Design

The radiation pattern of the crossed-dipole is formulated in [15]:

$$F(\mathbf{q}, \mathbf{j}) = \frac{\cos[\frac{1}{2}\mathbf{p}|\sin(\mathbf{q})|\sin(\mathbf{j})]\sin[\frac{1}{2}\mathbf{p}\cos(\mathbf{j})]}{\sqrt{1 - \sin^2(\mathbf{q})\sin^2(\mathbf{j})}}$$

Where, \mathbf{q} is the zenith angle and \mathbf{j} is azimuth angle using spherical coordinates. The antenna of Fig. 5 consists of 2 dipoles perpendicular to each other. The Im impedance components are nullified and the two Re impedances are matched, delayed by 90° with each other for an omni-directional pattern and routed through a power combiner. The output is fed to the main 50 Ohm feed-line that leads to the pre-amplifier.

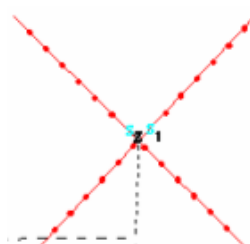


Fig. 5. Crossed-Dipole Antenna Modelling.

The antenna is positioned $l/4$ above ground, supported by non-resonant guy wires. The ground is modelled with a dielectric constant of 15 and ground conductivity of 0.0278 S/m to simulate the Tromso, Norway conditions. Its 3-D model and radiation pattern are in Fig. 5 and 6, respectively.

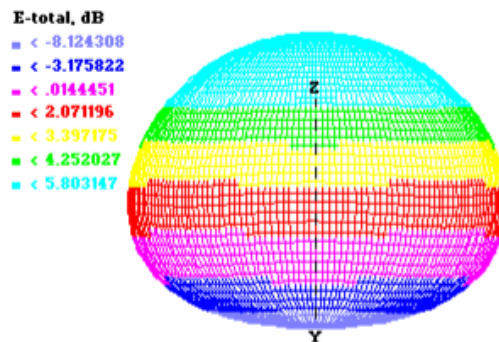


Fig. 6. 3-D Radiation Pattern. G=5.8dBi @90° elevation angle, HPBW=83.36°.

3.4 PRIAMOS Design

The 50 Ohm pre-amplifier circuit is tuned to 38.2MHz and exhibits a B of 5MHz, as shown in Fig. 7. Op-amp, double-tuned cascode and RF amplifiers has been tested and based on their performance and noise response a very low noise fixed gain RF amplifier was chosen.

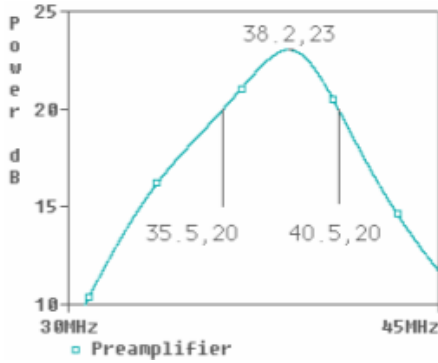


Fig. 7. 38.2MHz Pre-Amplifier Frequency Response.

The frequency response of the 50 Ohm high quality factor BPF is shown in Fig. 8.

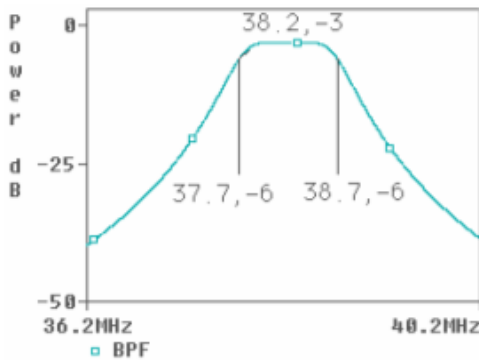


Fig. 8. Bandpass Filter Frequency Response
B=1MHz @ -3dB, Passband Ripple <0.2dB

The AGC amplifier [16] has a flat frequency response up to 150MHz and 90dBs gain range (-20-70dB). The AGC is activated by the DSP when the power exceeds the threshold value. SREs can be fully measured avoiding saturation. The ADC is driven differentially and samples at 95.5MHz. The differential input produces a high level AC performance and a B of 150MHz. The ADC is fully controlled by the DSP. A digital phase-locked loop (DLL) is inside the ADC and when activated, operates in the range 60-125MSPS. With DLL Off, operates in the range 10-80MSPS. The cosmic noise signal exits the ADC in the 2^s complement 14-bit parallel output format.

The master oscillator feeds the DSP with a programmable reference clock signal of 25MHz. The DSP after initialisation synchronises with the GPS,

sends the appropriate control signals back to the master oscillator and the required low jitter, 50% duty cycle sampling frequency is generated. The master oscillator is capable of producing a clock signal up to 250MHz. The output exhibits low jitter and duty cycle of 48-52%, up to 200MHz. It guarantees a duty cycle of 50% at 95.5MHz.

The GPS receiver instrumentation of Fig. 9 generates the reference integration time signal of 1s and provides synchronisation of the timestamped data with the Coordinated Universal Time (UTC). UT timestamping is important when performing joint experiments with other instruments and especially when their fields of view overlap. The DSP frequency controller accurately derives the wanted integration time. The GPS location information determines the theoretical QDCs.

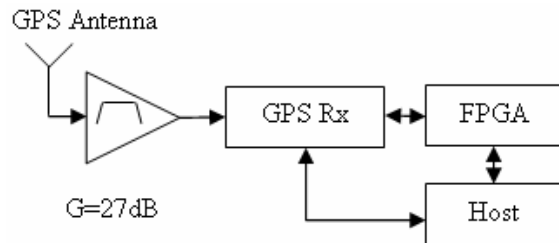


Fig. 9. GPS Receiver Block diagram.

The output of the ADC is connected to the DDC circuit of Fig. 10.

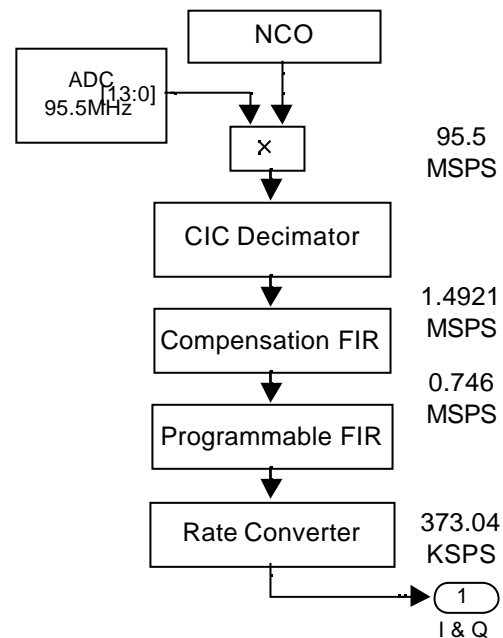


Fig. 10. Block Diagram of the baseband translator.

The DDC provides independent decimation and resampling, independent tuning, phase and gain control. The decimation factor is set to 64. The spurious free dynamic range (SFDR) is 115dB. The tuning resolution

is 0.02Hz. The cascaded integrator comb (CIC) filter [17] provides a variable B within the range of 3KHz – 4MHz. The resampler provides extra filtering and arbitrary selection of I/O rates. Overall, any data rate and any B are achievable, resulting in a flexible and reprogrammable solution. The frequency response of the baseband translator is in Fig. 11, where the programmable B is set to 250KHz.

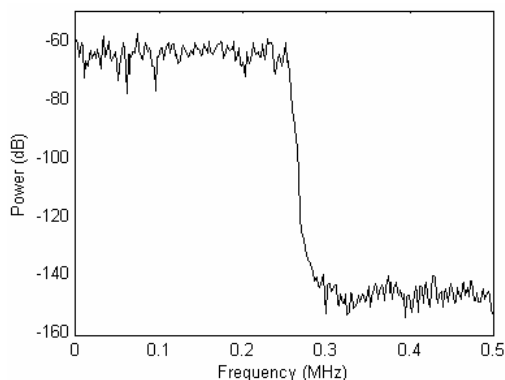


Fig. 11. Baseband Translator Frequency Response.

The complex low data rate output represents volts. The power is calculated in Watts using the cross-correlation function. The cross-correlator is suitable for direct hardware implementation inside the DSP. Linearity, sensitivity and dynamic range are determined by the receiver’s calibration curves. The dynamic range is 85 dBs. The power values are integrated for 1s. The integrator reset signal is driven from the 1 pulse-per-second (PPS) output of the GPS receiver. The integration time is reduced in cases where better resolution of a geomagnetic event is required.

3.5 Software Design

The data are collected to the host PC using C software and saved into indexed files. Each file contains 86,164 data values data for a sidereal day. The integrated power values are converted to dBm and plotted over 1 hour in Fig. 12. The QDC algorithm used in IRIS has been used for compatibility purposes. Other QDC methods are using the inflection point method [18]. Theoretical QDCs are derived knowing the galactic noise, antenna radiation pattern and GPS location. The sky map at 38.2MHz is in Fig. 13, while sky maps for 22, 30, 38 and 45MHz are in [19]-[22], respectively. The cross-dipole antenna’s field-of-view is projected on the ionosphere at 90 km altitude, as shown in Fig. 14. Similar results can be produced for any antenna type, knowing the current GPS location. The comparison of the experimental and theoretical QDCs for a quiet sidereal day is in Fig. 15.

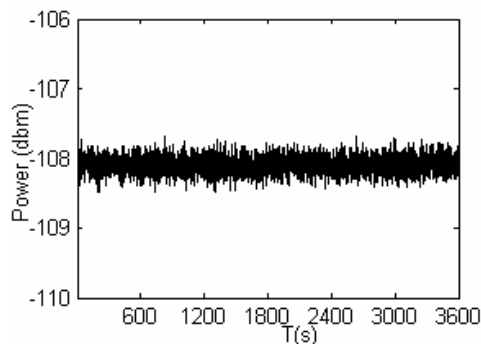


Fig. 12. 1s Integrated Data for 1h of Operation.

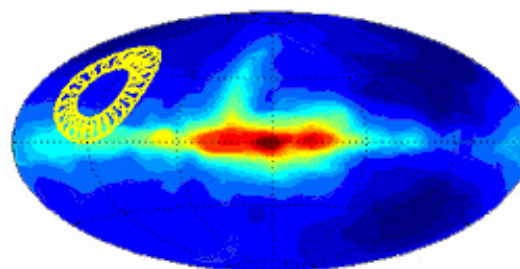


Fig. 13. Sky Map at 38.2 MHz and Right Ascension Scanning of the Galactic Plane within a Sidereal Day. Declination is constant.

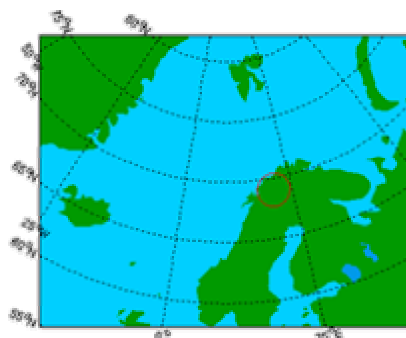


Fig. 14. Cross-Dipole’s Field-of-View, Projected on the Ionosphere at 90km Altitude.

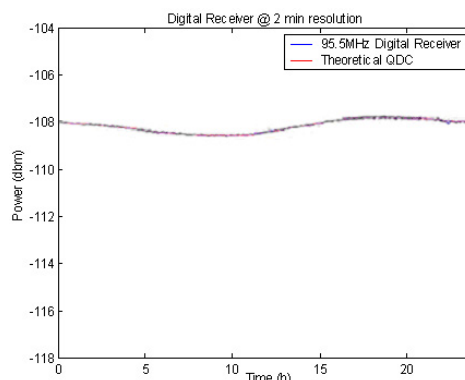


Fig. 15. Experimental and Theoretical QDCs Comparison for 1 Sidereal Day’s of Operation.

Summary

For the first time, a widebeam riometer experiment has so much flexibility in terms of possible system configurations, DSP power and software control. The system has excellent noise response and characteristics reprogrammable within seconds. The completion of the project means that any antenna and RF front-end system tuned to HF and L-VHF can be connected. Depending on the magnetospheric effect in progress, the system would have the capability of increasing the resolution of results, adjusting the gain to known values to avoid receiver's saturation and selecting the appropriate bandwidth. Matlab simulations assisted in modelling the riometer and experimenting with alternative architectures. Special attention was given to the design of the DDC and FIR filtering.

References

- [1] C. G. Little and H. Leinbach, "The Riometer- A Device for the Continuous Measurement of Ionospheric Absorption", Proc. IRE, V47, pp. 315 - 320, 1959.
- [2] L. Detrick et al., "Analysis of the Martian Atmosphere for Riometry", Planet. Space Science, V45, No. 3, pp. 289-294, 1997.
- [3] F. T. Berkey et al., "A synoptic Investigation of Particle Precipitation Dynamics for 60 Substorms in IQSY (1964-1965) and IASY (1969)", Planet. Space Sci, V22, pp. 255-307, 1974.
- [4] W. L. Ecklund and J. K. Hargreaves, "Some Measurements of Auroral Absorption Structure over Distances of about 300km and of Absorption Correlation between Conjugate Regions", J. Atmos. Terr. Phys., V30, pp. 265-283, 1968.
- [5] D.L. Detrick and T.J Rosenberg, "A Phased-Array Radiowave Imager for Studies of Cosmic Noise Absorption", Radio Sci, V25, No. 4, pp. 325-338, 1990.
- [6] P. Stauning, "Investigations of Ionospheric Radio Wave Absorption Processes using Imaging Riometer Techniques", Journ. Atmos. Terr. Phys., V58, pp. 753-764, 1996.
- [7] S. Browne, J. K. Hargreaves and B. Honary, "An Imaging Riometer for Ionospheric Studies", Journ. Electr. Comm., V5, pp. 209-217, 1995.
- [8] M. Grill, F. Honary, E. Nielsen, T. Hagfors, G. Dekoulis, P. Chapman and H. Yamagishi, "A New Imaging Riometer based on Mills Cross Technique", Proceedings of 7th International Symposium on Communication Theory and Application (ISCTA'03), Ambleside, The Lake District, UK, July 2003.
- [9] R. Panwar, J. Caruana and P. Wilkinson, "Application of Riometers in Space Weather", IPS Radio and Space Services, Sydney NSW 2000, Australia.
- [10] R. D. Strum and D. E. Kirk, "First Principles of Discrete Systems and Digital Signal Processing", V5, pp. 81-85.
- [11] ---, "Digital VXI VHF/UHF Receiver WJ-8629", Watkins-Johnson, 1994.
- [12] Orsak, "Optimum Receivers", The Mobile Communications Handbook, Boca Raton, FL: CRC Press, 1996.
- [13] J. Mitola, "The Software Radio Architecture", IEEE Comm. Mag., V33, No. 5, pp. 26-38, 1995.
- [14] U. Rhode et al., "Communications Receivers", New York, McGraw-Hill, 1997.
- [15] R. Carter, "Electromagnetic Waves: Microwave Components and Devices", Chapman & Hall, 1990.
- [16] I. Kipnis et al., "Silicon Bipolar Fixed and Variable Gain Amplifier MMICs for Microwave and Lightwave Applications up to 6GHz", IEE MTT-S Digest, pp. 109-112, 1989.
- [17] A. Kwentus et al., "Application of Filter Sharpening to Cascaded Integrator Comb Decimation Filters", IEEE Trans. Sig. Proc., V45, No.2, pp. 457-467, 1997.
- [18] S. Krishnaswamy, S. Detrick and T. J. Rosenberg, "The Inflection Point Method of Determining Riometer QDCs", Radio Sci., V20, No. 1, pp. 123-136, 1985.
- [19] R. Roger, C. Costain, T. Landecker and C. Swordlyk, "The Radio Emission from the Galaxy at 22 MHz", Astron. Astro-Phys. Supp., V137, pp. 7-19, 1999.
- [20] T. Milogradov, F. Smith, "A Survey of the Radio Back-Ground at 38 MHz", Mon. Not. R. Astr. Soc, V161, pp. 269-279, 1973.
- [21] B. Campistron et al., "A Partial 45 MHz Sky Temperature Map Obtained from the Observations of Five ST Radars", Ann. Geo., V19, pp. 863-871, 2001.
- [22] H. Cane, "A 30 MHz Map of the Whole Sky", Aust. J. Phys, V31, pp 561-565, 1978.

Two New Approaches to Spatial Interpolation with Inherent Sidelobe Suppression for Imaging Riometers

Martin Grill, Andrew Senior, Farideh Honary

All at Department of Communication Systems, Lancaster University, UK

Abstract

Absorption images as obtained by imaging riometers such as IRIS are usually created by interpolating between absorption values for individual beams. For IRIS, the locations of the beam centres serve as grid points for subsequent linear interpolation. Although generally producing good results, the fact that the actual shape of the imaging beams is not considered, potentially introduces errors and can lead to misinterpretations.

In this paper, two alternative interpolation methods are introduced. Method A is based on measuring the similarity between simulated reception of individual point sources and actually received data. Method B uses a mathematical model of the sky brightness distribution parametrised by the received data.

All interpolation methods are applied to power data, as opposed to absorption data, in order to avoid any errors that might be introduced by intermediate processing steps, especially QDC (quiet-day curve) generation.

We apply all methods to synthetically generated test data as well as to three exemplary real datasets which are also compared to a calculated sky brightness distribution obtained from a skymap.

1 Introduction

Riometers (Relative Ionospheric Opacity Meters) have been around for decades [9]. They measure absorption of cosmic background noise, caused by energetic particles ionising layers of the Earth's ionosphere. The first riometers were widebeam riometers with a large field of view in the order of 60° around zenith. The search for smaller scale structures led to the development of imaging riometers which divide a similar field of view into smaller areas by forming multiple beams, usually employing phased array antennas. Current imaging riometers have between 49 beams [2] and 256 beams [13], an even higher resolution imaging riometer based on a Mills Cross beamforming technique [12] currently being under development [14].

Along with the imaging capabilities of such riometers came the necessity to spatially interpolate between the measurements in order to form a real image of the observed area. Time series of these images can then be used for further studies like analysing the motion of absorption patches [10] and serve as a source for more advanced diagrams such as keograms, movies and virtual beams. These images can also be directly compared to images from other imaging instruments, for example optical cameras [5].

Currently, riometer images are usually created by interpolating between absorption values for individual beams. For IRIS, the Imaging Riometer for Ionospheric Studies [2], the locations of the beam centres serve as grid points for subsequent linear interpolation. This technique generally produces good results. However, the fact that the actual shape of the imaging beams is not considered, potentially introduces errors and can lead to misinterpretations. In particular, any given imaging beam receives signals not from one direction but from a range of directions around the beam centre, depending on the beamwidth, which itself is inversely proportional to the aperture of the receiving antenna. Also, a not always negligible fraction of signal is received from sidelobes that point in a significantly different direction from the main beam.

This paper suggests different interpolation methods that take the shape of the receiving beams into account. In doing so, they have the potential to compensate for the effects of sidelobes, to overcome the spatial constraints of linear interpolation (thus extending the field of view) and to uncover features that may not show up in traditionally interpolated images.

2 Prerequisites

In this section we introduce some general facts that are used for the observations in the following sections. We introduce the dataset that we will be using throughout this paper, highlight the role that obliquity factors play for the observations and introduce the coordinate system and the FLATM projection method that we use in this paper.

2.1 Power data, role of obliquity factors

The interpolation algorithms as discussed in this paper all deal with interpolation of power data on the positive hemisphere seen by the receiving instrument. The data is not interpreted in any way prior to processing. In particular, no assumptions are implied as to the media that the incoming signals traversed prior to reception, i.e. no correction factors (in this case known as obliquity factors) for the varying observed thickness of the absorbing layer etc. are applied to the data. In order to compare actual signals to theoretical signals based on convolution of beampatterns and skymap (see section 6), obliquity factors need to be taken into account as soon as there is an absorbing layer of electrons present. This layer appears thicker with decreasing elevation angles. See figure 1: The apparent thickness d' of the absorption layer decreases with

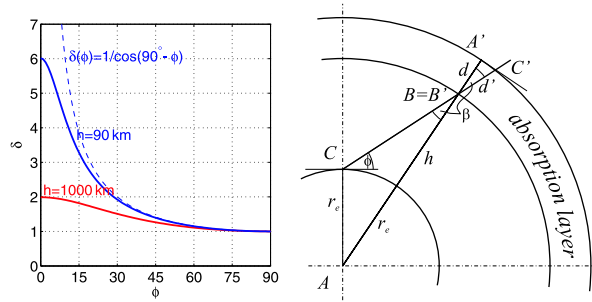


Figure 1: Obliquity factor δ correcting for apparent thickness of absorption layer (drawing not to scale)

observation elevation angle ϕ . The law of sines for $\triangle ABC$ allows us to derive angle β :

$$\sin\beta(\phi) = \frac{\sin(\phi + 90^\circ)}{r_e + h} \cdot r_e \quad (1)$$

from which we can derive the obliquity factor $\delta(\phi)$ simply by looking at $\triangle B'C'A'$ (as long as $d \ll (r_e + h)$):

$$\delta(\phi) = \frac{d'(\phi)}{d} = \frac{1}{\cos\beta(\phi)} \quad (2)$$

The left panel in figure 1 shows a plot of $\delta(\phi)$ for elevation angles $0^\circ \leq \phi \leq 90^\circ$ and $h = 90$ km (blue line). For comparison reasons, $\delta(\phi)$ is also shown for an (unrealistic) height $h = 1000$ km (red line). This is essentially a 'lower amplitude' version of $\delta(\phi)$ for $h = 90$ km. The dashed line is $\delta(\phi) = 1/\cos(90^\circ - \phi)$ as used in [7]. This is an approximation to equation 2 that works well for elevation angles $\phi > 30^\circ$.

Obliquity factors will also have to be taken into account when it comes to deriving absorption from the input data, but in this paper we are solely dealing with (spatial) interpolation of the underlying raw received data. Existing algorithms can then be used to derive quiet-day curves (QDCs) and absorption data for arbitrary directions ('virtual beams') within the usable working area of the given interpolation algorithm. Note, however, that equation 2 only works well if there is actually a well-defined absorption layer present. For quiet-day absorption, equation 2 generally exaggerates the expected results. This is because quiet-day absorption happens over a large range of heights, not within one narrow layer. In this paper, we only ever use obliquity factors for qualitatively comparing data derived from a skymap to actual measurements. To qualitatively compensate for quiet-day absorption we use the red curve in figure 1 when

we plot the sky brightness distribution as derived from a skymap (see section 6). This curve was empirically found to produce good results.

Note that this use of obliquity factors is different from the traditional use where obliquity factors are applied to received power values from each beam, either ignoring the beam shape or including the effects of the beam pattern in the ‘effective’ obliquity factor [7]. The obliquity factor in equation 2 does not relate to beams but simply to a certain viewing direction.

2.2 Time period

The time period chosen for the observations in this paper is 23rd September 1999. This day (as observed by the imaging riometer IRIS [2]) has quiet times, absorption events and ‘negative absorption events’ i.e. peaks in power due to interference (solar radio emissions). See figure 2 (obtained from the Multi

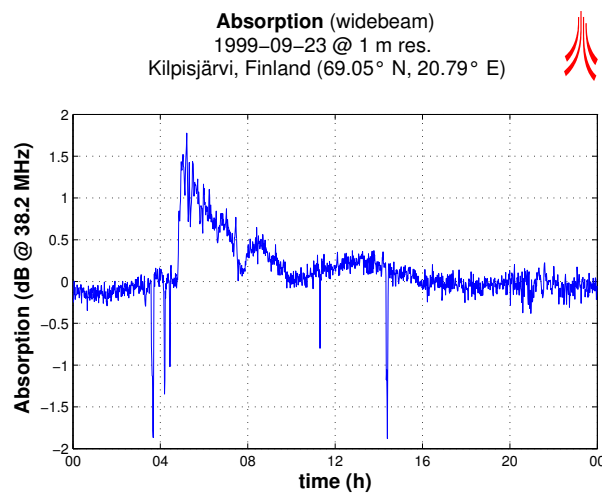


Figure 2: IRIS widebeam absorption during 1999-09-23

Instrument Analysis Toolkit MIA [11]). It is therefore an excellent dataset for comparing the performance of interpolation algorithms in various circumstances.

2.3 FLATM projection

Antenna radiation patterns and sky brightness distributions are most easily described in some sort of spherical coordinate system. In this paper we shall use a spherical coordinate system made up from azimuth angle θ (in the XY plane, counterclockwise, starting from the positive x-axis) and elevation angle ϕ (between XY plane and direction of interest, positive ϕ denotes positive z). For visualisation purposes and further studies, this spherical dataset often needs to be mapped onto a flat two-dimensional surface. For IRIS absorption images, we commonly use a projection that we will henceforth call the ‘FLATM’ (for ‘flat metres’) projection. This is a two-stage projection that first calculates the intersection between a ray in the given direction and the ionosphere (at a given height, 90km by default) and then maps the result onto a flat surface. The whole process is shown in figure 3. This projection offers relatively little distortion around the zenith, with distortion increasing with lower elevation angles. As the surface area of the ionosphere is much greater than the area usually covered by any given instrument, the FLATM projection gives a good (i.e. relatively undistorted) representation of the signal distribution at the height of the ionosphere (or any other sphere centred on the Earth’s centre for that respect).

Note that from the interpolation algorithms presented in this paper, only the original IRIS interpolation algorithm inherently uses the FLATM projection. The other algorithms interpolate in spherical coordinates, only the results shown in this paper are mapped back to FLATM projections for presentation and comparison purposes.

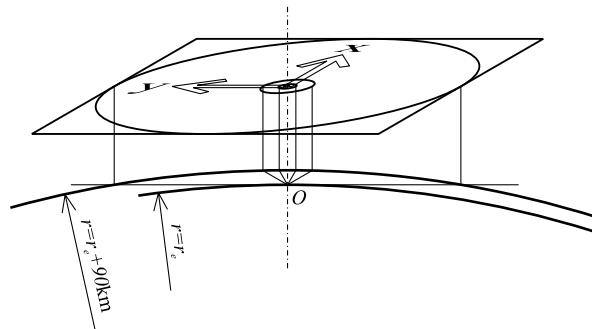


Figure 3: FLATM projection as used for IRIS image data. Drawn to scale. Instrument is situated at O.

3 Original IRIS interpolation algorithm

IRIS power/absorption images as created by the Multi-Instrument Analysis Toolkit (MIA) [11] use the FLATM projection to map the location of the 49 beam centres onto a flat two-dimensional grid¹. MIA assumes that the recorded power values originate from the respective beam centre (the direction of maximum gain, also referred to as beam axis or boresight) and then uses linear interpolation to fill the space between the beam centres. An example of this can be seen in figure 4 (left panel), together with the triangles that

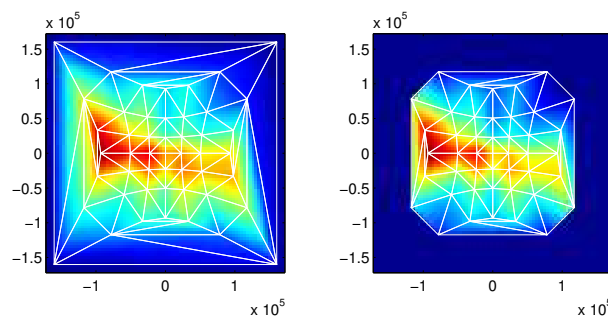


Figure 4: ‘Traditional’ IRIS Image Interpolation, distances are in m. Left panel shows Delaunay triangulation for all 49 beams, right panel shows Delaunay triangulation for only the ‘good’ beams.

are used internally by the two-dimensional linear interpolation algorithm. The vertices of the triangles represent the 49 beam centres. As the four corner beams (1, 7, 43, 49) have significant sidelobes [1] and the assumption of all power being concentrated at the beam centre does not even approximately hold, these beams are usually ignored leading to an interpolated image as depicted in figure 4 (right panel). Therefore the useable working area for this algorithm is defined by the convex hull of the beam centres projected onto a flat grid by the FLATM projection, and we will overlay a white bounding box in subsequent images generated by other algorithms (which are not inherently limited to this working area) to simplify visual comparison of the results.

¹Recent versions of MIA now use a default grid based on geographic latitude and longitude for interpolation, as geographic coordinates are more universally useful and accepted. This does not change the basic interpolation algorithm, however. We will stick with the FLATM projection in this paper, because it does not introduce any asymmetric distortion effects and is independent of instrument location.

4 Method A: Correlation method

Given the radiation patterns of all beams, we can (per definition) calculate the response of each beam to a noise source in any given direction. When calculating theoretical QDCs, this is done for all directions simultaneously, yielding the total response of each beam to the given sky brightness distribution as defined by a sky map. In the correlation method, a different approach is suggested:

First, we agree on a grid of ‘directions of interest.’ This can be any arbitrary list of I direction vectors $\vec{d}_i = [\theta_i, \phi_i]$, they do not have to form a regularly spaced grid.

We then treat each direction separately: For each direction \vec{d}_i we calculate the response of all N beams to a power source of a fixed intensity in that direction. This gives us N received power values p_n , one for each beam.

We then collectively compare this theoretical response of all beams $\{p_1 \dots p_N\}$ to the actual recording from these beams $\{b_1 \dots b_N\}$. The correlation as represented by the normalised cross correlation coefficient

$$c_i = \frac{1}{\sum_{n=1}^N p_n} \sum_{n=1}^N p_n b_n \quad (3)$$

between the two sets of values turns out to be a good estimate of how much the recording was influenced by a noise source in the particular direction in question (\vec{d}_i).

We repeat these steps for each direction \vec{d}_i and in doing so build up an image of the sky, represented by the values c_i .

It is interesting to note that equation 3 resembles the equation used for finite impulse response (FIR) filters, suggesting that this algorithm can be looked upon as some sort of matched directional filtering, the p_n being the expected responses.

4.1 Implementation note

Provided we know all potential directions of interest \vec{d}_i from the outset, the theoretical beam responses p_n can be calculated in advance. For any given set of input values b_n we then only need to calculate the cross-correlation coefficients c_i according to equation 3.

5 Method B: Parametrised model

We will first describe the general approach, this is not specific to using spherical harmonics, but is indeed valid for any kind of model that can be parametrised with a set number of parameters less than or equaling the number of concurrently available datapoints. We will then proceed to describe two approaches based on spherical harmonics.

5.1 (General) Curve Fitting Method

Rather than starting with an unknown power distribution (which is of course what we will be doing later on), let us assume for a moment that we know the spatial power distribution P across the visible hemisphere, i.e.

$$P(\theta, \phi) = \text{known} \quad (4)$$

We also know the radiation pattern for each of the given instrument’s N beams for all possible directions (θ, ϕ) :

$$B_{1 \dots N}(\theta, \phi) = \text{known} \quad (5)$$

Given the power distribution and the radiation patterns, we can now calculate the power response (the power received) $p_{n, \text{simul}}$ for each beam n . This is the same method that can also be used to derive theoretical quiet-day curves (see for example [16]):

$$p_{n,simul} = k \cdot \int_{\theta,\phi} P(\theta, \phi) B_n(\theta, \phi) \cos\phi d\theta d\phi \quad (6)$$

k is a constant that can be used for calibration purposes. The N values $p_{n,simul}$ directly correspond to the received power as measured by the receivers.

If we now find a way of representing the power distribution P in equation 4 by means of $M \leq N$ parameters instead of an infinite number of discrete values, we can work our way backwards from the actual received power values and derive (an approximation of) the original power distribution P , denoted P_{model} .

Let us assume that P_{model} is a linear combination of M functions of (θ, ϕ) , weighted by γ_m , i.e. a function of the direction as specified by (θ, ϕ) and of M parameters $\gamma_1 \dots \gamma_M$ as follows:

$$P_{model}(\theta, \phi, \gamma_1 \dots \gamma_M) = \gamma_1 \cdot f_1(\theta, \phi) + \gamma_2 \cdot f_2(\theta, \phi) + \dots + \gamma_M \cdot f_M(\theta, \phi) \quad (7)$$

In order to determine the parameters $\gamma_1 \dots \gamma_M$, we make use of equation 6, replacing the simulated results $p_{n,simul}$ with the actual measurement results p_n ($n = 1 \dots N$) from the N beams and the 'known' sky brightness distribution P (equation 4) with the modelled brightness distribution P_{model} (equation 7):

$$p_n = k \cdot \int_{\theta,\phi} B_n(\theta, \phi) P_{model}(\theta, \phi, \gamma_1 \dots \gamma_M) \cos\phi d\theta d\phi \quad (8)$$

We expand equation 8 using the definition of our model in equation 7:

$$p_n = k \cdot \int_{\theta,\phi} B_n(\theta, \phi) \cdot [\gamma_1 \cdot f_1(\theta, \phi) + \gamma_2 \cdot f_2(\theta, \phi) + \dots + \gamma_M \cdot f_M(\theta, \phi)] \cos\phi d\theta d\phi \quad (9)$$

Rearranging:

$$\begin{aligned} p_n &= \gamma_1 \cdot k \cdot \int_{\theta,\phi} B_n(\theta, \phi) f_1(\theta, \phi) \cos\phi d\theta d\phi \\ &+ \gamma_2 \cdot k \cdot \int_{\theta,\phi} B_n(\theta, \phi) f_2(\theta, \phi) \cos\phi d\theta d\phi \\ &+ \dots \\ &+ \gamma_M \cdot k \cdot \int_{\theta,\phi} B_n(\theta, \phi) f_M(\theta, \phi) \cos\phi d\theta d\phi \end{aligned} \quad (10)$$

Combining all constant terms into constants c :

$$p_n = c_{n,1} \gamma_1 + c_{n,2} \gamma_2 + \dots + c_{n,M} \gamma_M \quad (11)$$

which can be written as one matrix equation for all N beams:

$$P = C \times \Gamma. \quad (12)$$

In other words, we get one linear equation with M unknowns $\{\gamma_1 \dots \gamma_M\}$ for each of the N beam patterns. This set of equations can be solved (possibly in a least-squares sense for $N \neq M$) and therefore the unknown model parameters $\{\gamma_1 \dots \gamma_M\}$ can be determined. Once these parameters are known, the (model) sky brightness can be calculated in any arbitrary direction (θ, ϕ) by using equation 7.

5.2 Implementation employing Spherical Harmonics (B1)

Spherical harmonics [8] can be used to describe intensity distributions around a sphere. See, for example, [17] for a geophysical application. Spherical harmonics are useful because they form an orthogonal basis for functions on the sphere in a manner analogous to sines and cosines on the interval $[0, 2\pi]$. We are, of course, only using a finite number of spherical harmonics to approximate these functions, as is often done for Fourier sine/cosine series.

Spherical harmonics are solutions to Laplace's equation in spherical coordinates [19]. Without going into any further mathematical details, we stick to the practical description of the properties of spherical harmonics as found in [15]:

"The spherical harmonic $Y_{lm}(\theta, \phi)$, $-l \leq m \leq l$, is a function of the two coordinates θ, ϕ on the surface of a sphere. The spherical harmonics are orthogonal for different l and m , and they are normalised so that their integrated square over the sphere is unity."

The degree of the spherical harmonic in question is depicted by l , the order by m . The spherical harmonics are related to *associated Legendre polynomials* P_l^m by the following equation ([15]):

$$Y_{lm}(\theta, \phi) = K_l^m P_l^m(\cos\theta) e^{im\phi} \quad (13)$$

Since we are only dealing with a real numbers, we will use real spherical harmonics defined as follows:²

$$Y_{lm}(\theta, \phi) = \begin{cases} \sqrt{2} K_l^m \cos(m\phi) P_l^m(\cos\theta), & m > 0 \\ \sqrt{2} K_l^m \sin(-m\phi) P_l^{-m}(\cos\theta), & m < 0 \\ K_l^0 P_l^0(\cos\theta), & m = 0 \end{cases} \quad (14)$$

In both equations 13 and 14, the scaling factor K is defined as:

$$K_l^m = \sqrt{\frac{(2l+1)(l-|m|)!}{4\pi(l+|m|)!}} \quad (15)$$

Note that this scaling factor (equation 15) is constant for any given l, m . For our purposes we can therefore ignore this part, the weighting coefficients will automatically adjust themselves to accommodate for this missing factor.

For modelling the sky brightness distribution according to equation 7, we need a linear combination of a number of spherical harmonics equalling the number of available beam power readings N (49 in case of the IRIS observations used in this paper). We establish a unique order between the spherical harmonics starting with $f_1 = Y_{l=0;m=0}$ and then moving on to higher degrees, cycling through all possible orders $m = -l, \dots, m = l$ for each degree, until we arrive at $f_{49} = Y_{l=6;m=6}$.

5.3 Implementation using adjusted spherical harmonics (B2)

Ordinary spherical harmonics as used in 5.2 have the disadvantage of modelling the brightness distribution over the surface of a complete sphere, resulting in relatively low-resolution at any given region of interest. Especially, in our case, a riometer will only ever 'see' at most a hemispherical subsection of the whole sky. It would be sensible to choose a basis which represents the power distribution over the hemisphere alone. One possibility is capped spherical harmonics [6]. However, capped spherical harmonics can be complex to implement and can result in a range of computational problems [18]. Therefore, in this paper, we use a simple approximation to spherical capped harmonics called 'adjusted spherical harmonics' as proposed by DeSantis [17]. It is based on a coordinate transformation that 'adjusts' (compresses) the elevation angles ϕ in the original definition of the spherical harmonic to those of interest (in our case the visible hemisphere). By employing these adjusted spherical harmonics, we effectively double the resolution in the hemisphere of interest. We still use the same logical order of spherical harmonics as described in section 5.2 above.

5.4 Implementation notes

As for interpolation method A (section 4), some of the values needed for evaluating equation 7 can be pre-calculated. In case of method B we do not need to know about the required directions \vec{d}_i from the outset, we only need to define a grid for numerically doing the integration in equation 10, this grid does not directly relate to the possible output directions, it is only used for the integration (summation) process, therefore limiting the accuracy of the results if chosen too wide-meshed. Once we have defined this 'internal' grid, the N -by- N matrix C (made up of the values $c_{1\dots N, 1\dots N}$ in equation 11 can be computed. For any given set

²Robin Green, "Spherical Harmonic Lighting: The Gritty Details", <http://www.research.scea.com/gdc2003/spherical-harmonic-lighting.html>

of input values b_n we then only need to solve the system of linear equations (equation 11 for all $n = 1 \dots N$) and use equation 7 to calculate the interpolated power values for arbitrary directions (θ, ϕ) . Note that this method has ‘self-interpolating’ properties, meaning that once we have calculated the coefficients c , we are not limited to certain predefined directions. Instead, equation 7 will directly give results for all desired directions (θ, ϕ) .

6 Results

In this section, we will present the results from the two interpolation methods for three different times during 23rd September 1999 as well as for two test-cases using synthetically generated data. We will compare these results to the result obtained by the original MIA interpolation method. The results for the synthetically generated brightness distributions are compared to these very distributions. For the ‘real’ datasets, this is of course impossible since we do not know the actual sky brightness distribution in these cases. We will compare the ‘real’ datasets to the expected sky brightness distribution as derived from a skymap [4], noting that the real distribution at the time might vary greatly from this theoretical distribution, especially during active times.

In the following figures, each panel is the FLATM projection (see section 2.3) of the respective results, covering a square area of 340×340 km. For figures containing ‘real’ data, we also show in each panel the locations of the two major radio stars [3] in this area of the sky, Cassiopeia A (white circle) and Cygnus A (white X).

6.1 Synthetic test brightness distribution 1

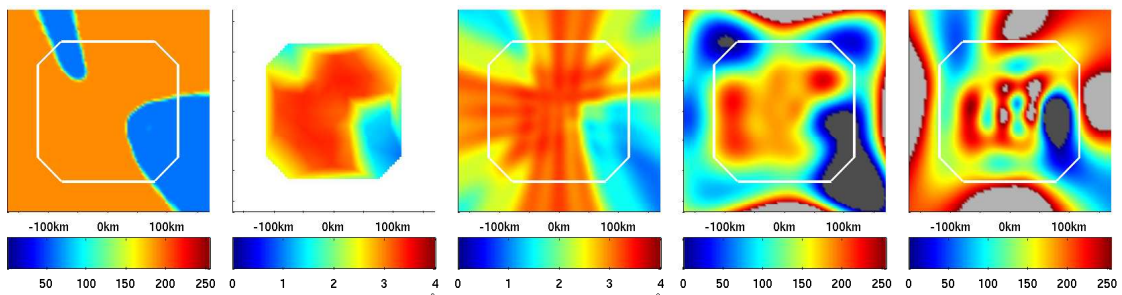


Figure 5: Simple testimage used as input to the interpolation algorithms. From left to right: Synthetic skymap used to synthesise power readings for all 49 IRIS beams; original MIA interpolation algorithm applied to the synthetic power readings of all IRIS beams except the four corner beams (‘good beams’); interpolation method A applied to simulated data from all 49 beams; interpolation method B1 applied to simulated data from all 49 beams; interpolation method B2 applied to simulated data from all 49 beams.

In a first step, the algorithms were compared using a synthetically generated dataset. The leftmost panel in figure 5 shows the image that was used as a skymap. Convolution of the 49 IRIS beampatterns with this skymap according to equation 6 results in 49 synthetically created ‘power readings’. The four remaining panels show the results of applying these synthetically created power readings to the different interpolation algorithms.

The original MIA interpolation algorithm produces a good representation of the input distribution. The intensity values diminish towards the outside of the interpolated area. There are low-power artefacts due to the interpolation between distant beams, especially visible at the top and bottom of the image.

Algorithm A also produces a good representation of the input distribution. However, some effect of the beam patterns is visible, and the power values trail off towards the to right and bottom left of the image.

Algorithm B1 shows the general shape of the input distribution within the primary field of view. The distribution is not nearly uniform, however, and there are strong overshoots in both negative and positive

directions. Algorithm B2 clearly shows the doubled spatial resolution compared to B1, but also seems to emphasise the problems observed with B1. There are strong overshoots in positive and negative directions and a high level of variability even inside the primary field of view.

6.2 Synthetic test brightness distribution 2

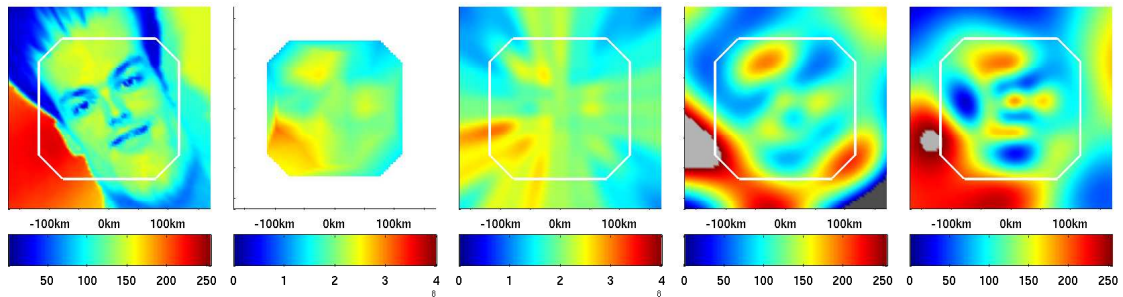


Figure 6: More detailed test image used as input to the interpolation algorithms. From left to right: Synthetic skymap used to synthesise power readings for all 49 IRIS beams; original MIA interpolation algorithm applied to the synthetic power readings of all IRIS beams except the four corner beams (‘good beams’); interpolation method A applied to simulated data from all 49 beams; interpolation method B1 applied to simulated data from all 49 beams; interpolation method B2 applied to simulated data from all 49 beams.

A more detailed input image was now used to investigate the reaction of the different algorithms to input data with higher spatial structure. See figure 6.

All algorithms seem to be able to resolve the main features (eyes, mouth). The influence of the beam-patterns is again clearly visible in the image created by algorithm A, while in the original MIA interpolated image the structure of the triangles used for the interpolation seems to show through. Both algorithms B1 and B2 seem to be doing rather well in this test case. They both emphasise the main structures rather better than the other algorithms. However, we can again observe a tendency to overshoot. Notice that both B1 and B2 tend to oscillate, especially visible for B2 as one moves from top to bottom.

6.3 Quiet Dataset

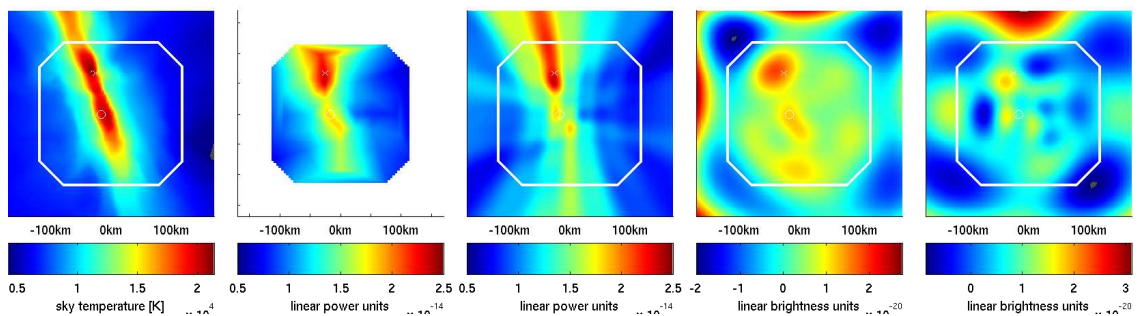


Figure 7: Quiet Dataset (1999-09-23 21:47UT). From left to right: Skymap for this part of the sky at this particular moment in time; original MIA interpolation algorithm applied to actual data as received by IRIS at the time in question (only ‘good beams’ i.e. all beams except the four corner beams); interpolation method A applied to real data from all 49 beams; interpolation method B1 applied to real data from all 49 beams; interpolation method B2 applied to real data from all 49 beams.

Figure 7 shows 1-minute integrated data for a quiet part of the day around 21:47UT. The skymap panel shows that we would expect to see a band of high power across the field of view. Both the traditional MIA interpolation algorithm and method A tend to break the band up into sections of varying intensity, the effects of individual imaging beams showing through. Note, however, that method A at least seems to show the continuity of this high power section to the top and to the bottom above and beyond the working area of the MIA algorithm. Opposed to this, the traditional MIA method shows areas of low power to the top and the bottom of the high power section, resulting from the linear interpolation between the outermost beam centres. This is clearly not an accurate representation of the real sky brightness. This can, of course, be eliminated by further limiting the working area of the algorithm, further reducing the field of view of the instrument.

Both methods B, whilst still showing the approximate direction of the high power band, produce several local maxima and minima within the visible area, that clearly do not resemble the actual expected brightness distribution. Notice that the two largest local maxima seem to coincide with the location of the two radio stars.

6.4 Absorption Event

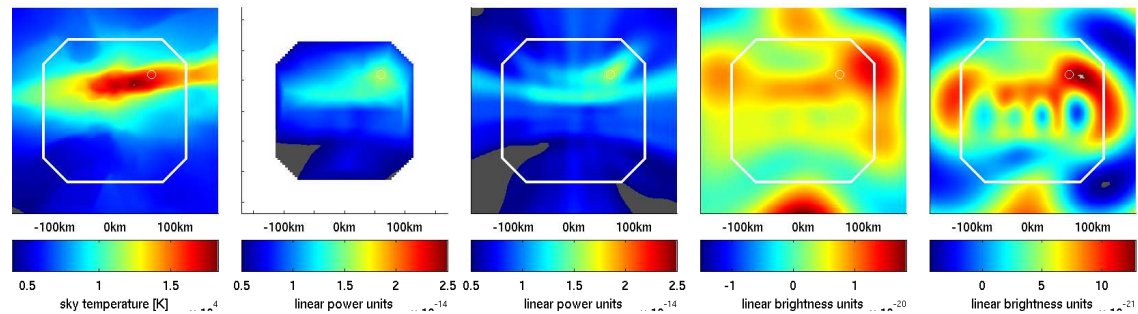


Figure 8: Absorption Dataset (1999-09-23 05:23UT). From left to right: Skymap for this part of the sky at this particular moment in time; original MIA interpolation algorithm applied to actual data as received by IRIS at the time in question (only ‘good beams’ i.e. all beams except the four corner beams); interpolation method A applied to real data from all 49 beams; interpolation method B1 applied to real data from all 49 beams; interpolation method B2 applied to real data from all 49 beams.

Figure 8 is a 1-minute integrated dataset for a period of strong absorption around 05:23UT. Note the generally reduced power in all three images that are derived from real data. The image obtained by method A quite clearly shows individual beam shapes, even though those should in theory be completely removed by the algorithm. The image produced by the traditional MIA algorithm looks much smoother. It does, however, again show the sharp cutoffs, this time at the left and right, where we would expect the bright band to continue North and South. Also note the isolated brighter spot at the bottom. Looking at the skymap, we’d expect this spot to continue towards the bottom, as it indeed does for method A.

Method B, while clearly showing less overall power and the general direction of the high-power band, again seems to be the worst of the interpolation methods. It still manages to approximately show the location of the radio star. Especially method B2 shows strong oscillations in the horizontal direction.

6.5 Interference Event

Finally, figure 9 is an example of strong solar radio emissions as captured by the IRIS riometer at 03:39UT. The original MIA interpolation method clearly shows the high power received from the eastern side of the array. Similar to the previous figures, the image seems to contain errors in the extreme outer parts, especially visible at the right, where the interpolation algorithm produces a red band all along the right-hand side. In comparison, method A clearly separates the two power sources (galactic centre and solar

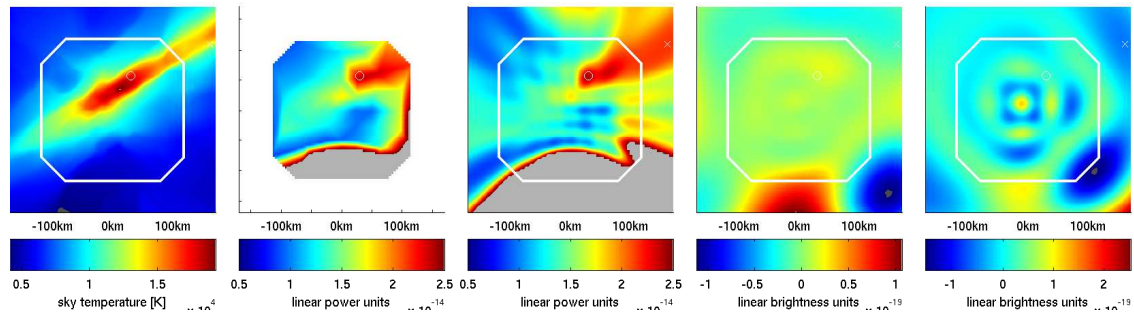


Figure 9: Interference Dataset (2004-09-23 03:39UT). From left to right: Skymap for this part of the sky at this particular moment in time; original MIA interpolation algorithm applied to actual data as received by IRIS at the time in question (only 'good beams' i.e. all beams except the four corner beams); interpolation method A applied to real data from all 49 beams; interpolation method B1 applied to real data from all 49 beams; interpolation method B2 applied to real data from all 49 beams.

radio emission). Overall, however, the image created by method A shows strong beam artifacts, whereas the MIA image looks smooth.

Method B1 seems to show the location of the radio star, and both methods B show high intensity in the direction of the solar radio emission. As before, they fail to accurately map the overall brightness distribution, however.

7 Conclusion

We compared the traditional MIA riometer power image interpolation method to two other methods that try to take the actual antenna radiation patterns of the riometer into account. While method A seems to give good results for the 49 beam riometer IRIS, methods B1 and B2 fail to accurately reconstruct the sky brightness distribution in the general case. Some results seem to suggest that methods B1 and B2 may be useful for identifying strong but spatially small features (figure 6).

At this stage, method A seems to perform equally to the traditional MIA method, both methods leading to slightly different results due to the different underlying principles. Given that the shapes of the beam patterns still show through in the resulting images, there seems to be no clear advantage of this method over the original MIA method. Which method is more suitable for the given task at hand will need to be decided on a case-by-case basis.

In its current form, method B fails to accurately model the brightness distribution to a high enough level of accuracy. It also suffers from oscillations and overshoots.

Although failing to deliver the increase in quality that was originally envisaged, it is hoped that this paper will trigger an increased interest in the area of interpolation algorithms for improving images generated by riometers, eventually leading to higher quality absorption images as a basis for high quality riometry work. The following sections give a few ideas as to possible improvements and ongoing work.

8 Suggestions for Improvements / Future work

In interpolation method A, the influence of the beam patterns seems to be visible, whereas ideally this method should completely eliminate any beam-related patterns from the resulting image. One option might be to weight different beams differently in equation 3, aiming to put less emphasis on beams whose beam patterns are less certain. With regard to both methods A and B, the theoretically derived beam patterns could be replaced by actual beam measurements (provided these are available), or the theoretical beam patterns could be replaced by simulated beam patterns that take imperfect ground conditions into account.

Research is ongoing with the aim of improving method B's results. Currently, the matrix problem is ill-conditioned due to the inability of the IRIS beam pattern to discriminate between a large number of configurations of the model power distribution, effectively resulting in fewer equations than unknowns. In section 5.1, it has already been hinted at the fact that the number of equations used to model the brightness distribution (M) does not have to equal the number available data points (N). In fact, having $M < N$ allows for least-square fits and also for error ranges to be included in the approximation. This has the potential to significantly increase the quality of method B's output, along with a built-in quality indicator. Along the same lines, it is possible to add additional spatial constraints to increase the number of available equations. This will lead to a better conditioning of the matrix problem.

It may also be possible to improve method B's results by choosing different interpolation functions for the curve fitting process.

Finally, it has to be noted that interpolation of power images is only the first step to deriving absorption data in arbitrary (virtual beam) directions. Based on the interpolation algorithms presented in this paper, quiet day curves (QDCs) can potentially be calculated for arbitrary directions, enabling the derivation of absorption in these directions and therefore the creation of absorption images on arbitrary grids and with arbitrary resolutions.

Appendix A: Image interpolation with Spherical Harmonics

To confirm the spatial resolution that image approximation using spherical harmonics is able to produce, three test images have been approximated by calculating the first 49 and 256 coefficients for both the standard spherical harmonics approach (section 5.2) and the adjusted spherical harmonics approach (see section 5.3), see the figures 10, 11 and 12. Clearly, spherical harmonics are able to reproduce the source image with sufficient details, but deriving the coefficients from real-world data is non-trivial.

References

- [1] Noach Amitay, Victor Galindo, and Chen Pang Wu. *Theory and analysis of phased array antennas*. Wiley-Interscience, New York, 1972.
- [2] S. Browne, J. K. Hargreaves, and B. Honary. An imaging riometer for ionospheric studies. *Electronics and Communication Engineering Journal*, 7(5):209–217, October 1995.
- [3] Bernhard F. Burke and Francis Graham-Smith. *An Introduction to Radio Astronomy*. Cambridge University Press, 1st edition, 1997.
- [4] H. V. Cane. A 30 MHz map of the whole sky. *Australian Journal of Physics*, 31:561–565, 1978.
- [5] C. F. del Pozo, M. J. Kosch, and F. Honary. Estimation of the characteristic energy of electron precipitation. *Annales Geophysicae — Atmospheres, Hydrospheres and Space Sciences*, 20(9):1349–1359, 2002.
- [6] G. V. Haines. Spherical cap harmonic analysis. *Journal of Geophysical Research*, 90:2583–2591, 1985.
- [7] J. K. Hargreaves and D. L. Detrick. Application of polar cap absorption events to the calibration of riometer systems. *Radio Science*, 37(3):7/1–7/11, 2002.
- [8] Ernest William Hobson. *The theory of spherical and ellipsoidal harmonics*. 1955.
- [9] C. G. Little and H. Leinbach. The riometer - a device for continuous measurement of ionospheric absorption. *Proceedings of the Institution of Radio Engineers*, 47:315–320, 1959.
- [10] R. A. Makarevitch, F. Honary, I. W. McCrea, and V. S. C. Howells. Imaging riometer observations of drifting absorption patches in the morning sector. *Annales Geophysicae — Atmospheres, Hydrospheres and Space Sciences*, 22(10):3461–3478, 3rd November 2004.

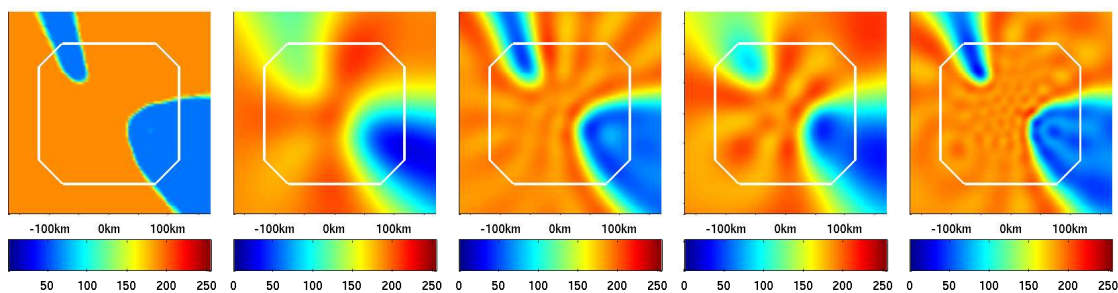


Figure 10: Interpolating an image using spherical harmonics. From left to right: original image; interpolated image using 49 coefficients and standard spherical harmonics; interpolated image using 256 coefficients and standard spherical harmonics; interpolated image using 49 coefficients and adjusted spherical harmonics; interpolated image using 256 coefficients and adjusted spherical harmonics.

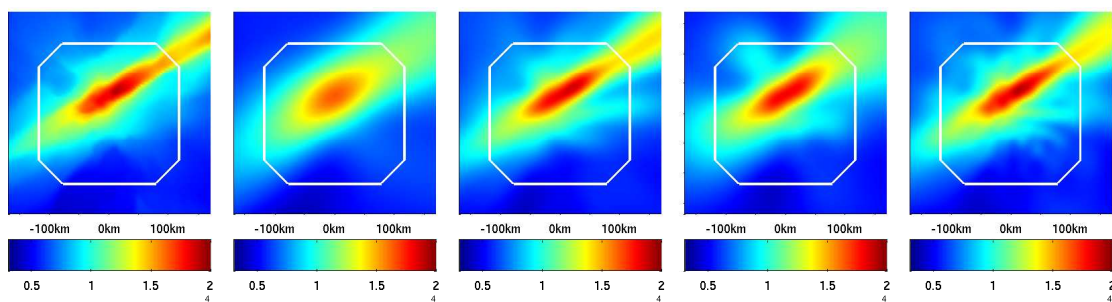


Figure 11: Interpolating an image using spherical harmonics. Panels as in figure 10.

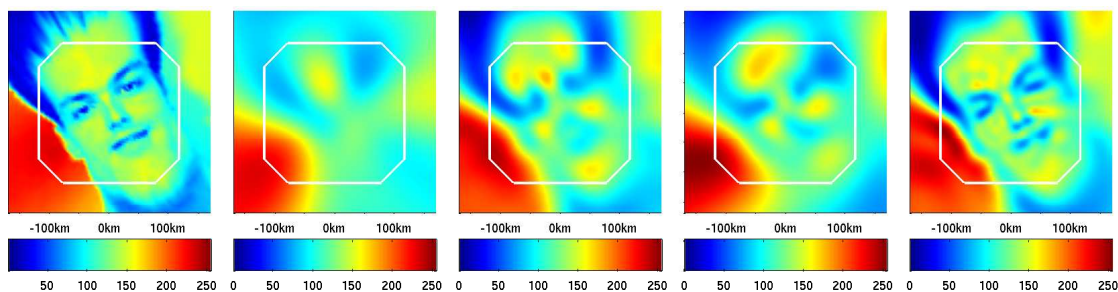


Figure 12: Interpolating an image using spherical harmonics. Panels as in figure 10.

- [11] S. R. Marple and F. Honary. A multi-instrument data analysis toolbox. *Advances in Polar Upper Atmosphere Research*, 18:120–130, September 2004.
- [12] B. Y. Mills and A. G. Little. A high-resolution aerial system of a new type. *Australian Journal of Physics*, 6:272–278, 1953.
- [13] Yasuhiro Murayama, Hirotaka Mori, Shoji Kainuma, Mamoru Ishi, Ichizo Nishimuta, Kiyoshi Igarashi, Hisao Yamagishi, and Masanori Nishino. Development of a high-resolution imaging riometer for the middle and upper atmosphere observation program at Poker Flat, Alaska. *Journal of Atmospheric and Solar-Terrestrial Physics*, 59(8):925–937, 1997.
- [14] E. Nielsen and T. Hagfors. Plans for a new rio-imager experiment in Northern Scandinavia. *Journal of Atmospheric and Solar-Terrestrial Physics*, 59(8):939–949, 1997.
- [15] William H. Press, Brian P. Flannery, Saul A. Teukolsky, and William T. Vetterling. *Numerical Recipes in C*. Cambridge University Press, 1st edition, 1988.
- [16] T. J. Rosenberg, D. L. Detrick, D. Venkatesan, and G. van Bavel. A comparative study of imaging and broad-beam riometer measurements: The effect of spatial structure on the frequency dependence of auroral absorption. *Journal of Geophysical Research — Space Physics*, 96(A10):17793–17803, October 1991.
- [17] A. De Santis. Conventional spherical harmonic analysis for regional modelling of the geomagnetic field. *Geophysical Research Letters*, 19:1065–1067, 1992.
- [18] A. De Santis and J.M. Torta. Spherical cap harmonic analysis: a comment on its proper use for local gravity field representation. *Journal of Geodesy*, 71:526–532, 1997.
- [19] Eric W. Weisstein. *CRC Concise Encyclopedia of Mathematics*. Chapman & Hall/CRC, 2nd edition, December 2002.

Calibration of TV all-sky data by simultaneous observations of scanning photometer

Boris V. Kozelov

Polar Geophysical Institute, Apatity, Murmansk region, 184209, Russia

Abstract. Calibration of image intensity is a common problem that hampers the use of TV data in quantitative auroral studies. The availability of simultaneous photometry observations allowed us to carry out relative calibration. An example of such calibration is described in this report. The data of two instruments located at Barentsburg, Svalbard (78.1°N, 14.24°E, 75.17MLAT, 112.1MLON) are used: a TV all-sky camera and a meridian scanning photometer. The scan trajectory in the TV field of view was traced by stars crossings. The calibration procedure was based on comparison of the surrogate keogram constructed from TV data and the keograms really observed by the scanning photometer in 557.7 and 427.8 nm emission spectral bands. The calibration curve (intensity of the auroral emission as a function of TV gray level) was interpolated in each 5-degrees interval of zenith angle to obtain the angle dependence. In both cases of aurora emission used, it was found that the calibrated surrogate keogram constructed from TV data reproduced reasonably well the fine small-scale structure of bright aurora observed by the scanning photometer.

1 Introduction

Ground-based observations of the polar aurora have very long traditions in geophysics. Now it is known that the aurora variety is a result of numerous processes occurring in the different regions of the magnetosphere-ionosphere system: energization due to parallel electric fields, Kelvin-Helmholtz instability, wave-particle interactions, current sheet pitch-angle scattering, field-line resonances, etc. (see, for example, reviews in Lyons et al., 1999). Investigation of these processes usually requires a separation of temporal and spatial variations. Ground-based television (TV) observations give the data which contain two-dimensional spatial and very good

temporal information. However, now the images themselves are mainly used only as illustrations. One of the common problems that hampers the use of TV data in quantitative auroral studies is an absence of calibration of TV image intensity.

This paper describes a possible procedure of calibration of image intensity in TV data by data of simultaneous photometry observations.

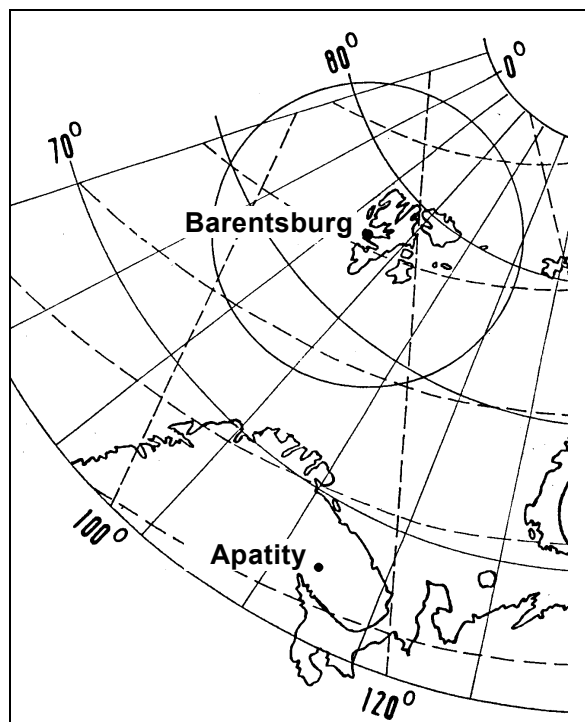


Fig.1. Kola Peninsula and Barentsburg Observatory of Polar Geophysical Institute

2 PGI optical observations at Barentsburg

Barentsburg Observatory (78.1°N, 14.12°E, 75.3 MLAT, 112.1 MLON) of Polar Geophysical Institute is equipped by two optical instruments: a TV all-sky camera (TVASC) and a meridian scanning photometer (MSP). The TV all-sky camera observes the auroral emission in the range of visible light with a broad maximum at

blue-green wavelengths. Field of view of TVASC is shown in Fig.1. The TV data were saved by VHS recorder at the long-play type speed encoded in PAL video system, 25 images per second. We digitized the data by Acorn TV-Capture plate with the output resolution of 5 images per second, 320×288 pixels, 8 bits per pixel.

The MSP is a 4-channel photometer monitoring the auroral emission at the wavelengths 427.8 nm (N_2^+ 1NG), 557.7 nm (OI), 630.0 nm (OI), and 489.1 nm ($H\beta$). The photometer data were recorded with the angular

resolution of about 0.5 degree, and the scanning time along the geographic meridian of about 12 seconds. Typically, the photometer scans the sky every 60 seconds, with even (odd) scans corresponding to south-north (north-south) scanning directions. The MSP was calibrated by calibration lamp TRS-28-50, with an estimated discrepancy of emission intensity in the 557.7 nm channel of 25%.

Here we use data obtained during night of 19-20 January 2001 that was reliably documented by both instruments. The MSP data of this event in 557.7 nm emission line is shown in Fig.2.

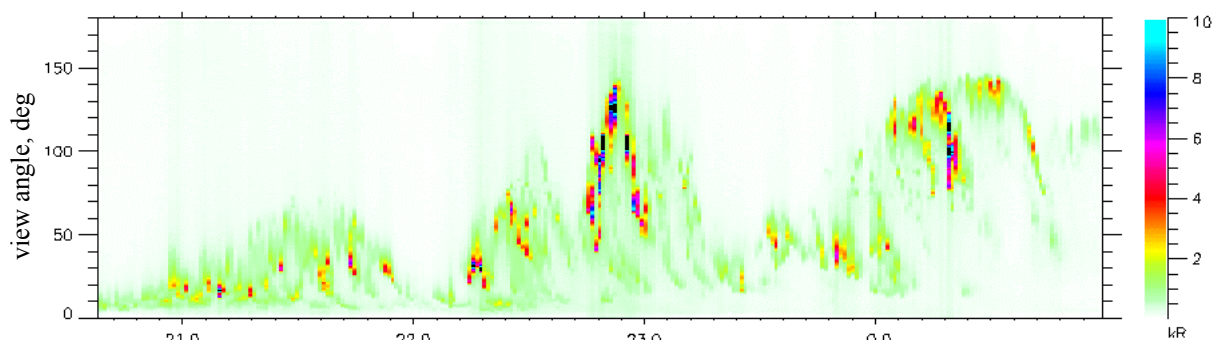


Fig.2. Meridian scanning photometer observations in 557.7 nm emission band during 19-20 January 2001 at Barentsburg Observatory. View angle is counted from south horizon

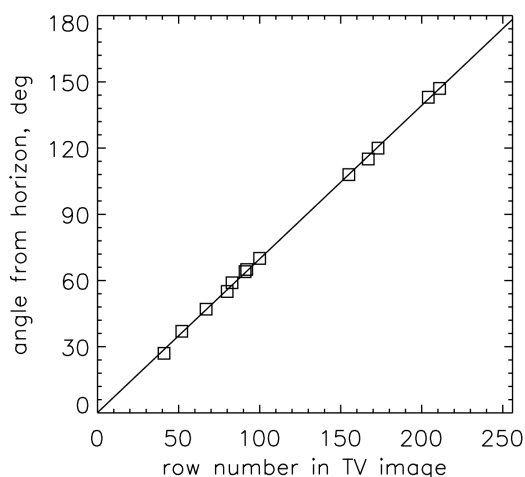


Fig.3. Relation between row number in TV image along the trajectory of scanning photometer and angle from south horizon: symbols are position of stars, line is the least square linear fit.

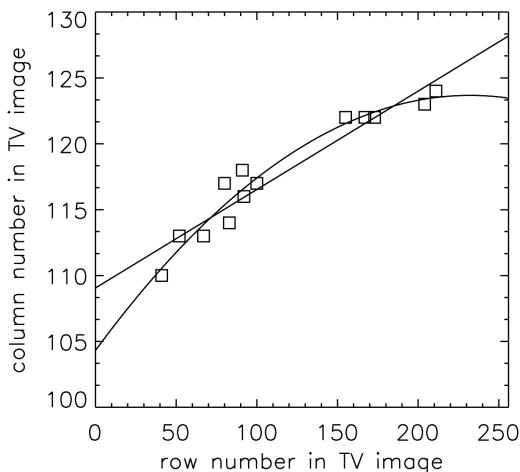


Fig.4. Relation between row and column numbers in TV image along the trajectory of scanning photometer: symbols are position of stars, lines are the least square fitted first and second order curves.

3 Calibration procedure

The offered calibration procedure consisted of the following basic steps:

I. The trajectory of the scanning photometer in the TV-camera field of view was traced precisely by star crossings.

Star crossing by the scanning photometer was fixed. Then, relation between row number in TV image for the star positions and the scanning angle from south horizon was fitted by the crossing points, Fig.3. The stars positions in TV image at the crossing moments gives the trace of the scanning photometer in the TV-camera field

of view, Fig.4. Fig.5 shows the least square fitted curves of MSP trace plotted in TV image. A difference between the first and second order curves is minor, so here we will use the linear fitted trace.

II. Taking the operational mode of the scanning photometer into account, an analogue of the keogram was constructed from the TV frames. As the time between scans is well stabilized, the adjustment of 2 parameters is required: initial time of first scan for considered event and average scanning time.

III. Based on the comparison of the observed keogram intensity and the gray-color level in the analogue keogram, the dependence of the calibration factor as a function of the zenith angle is obtained. For this we construct a dependence of intensity of the auroral emission (from MSP data in 557.7 nm emission spectral band) as a function of TV gray level for each 5-degrees view angle interval, see Fig.6.

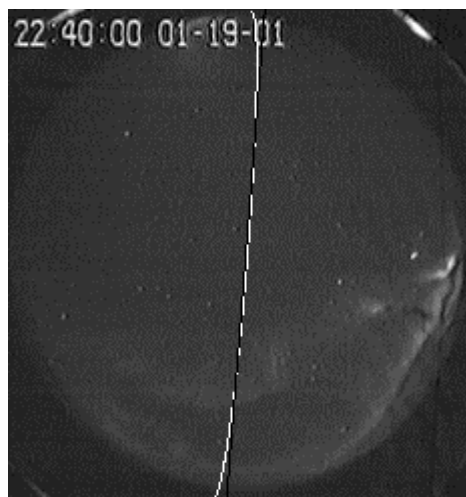


Fig.5. TV frame with MSP scanning trace. Black line - linear interpolated, white line - interpolated by second order curve

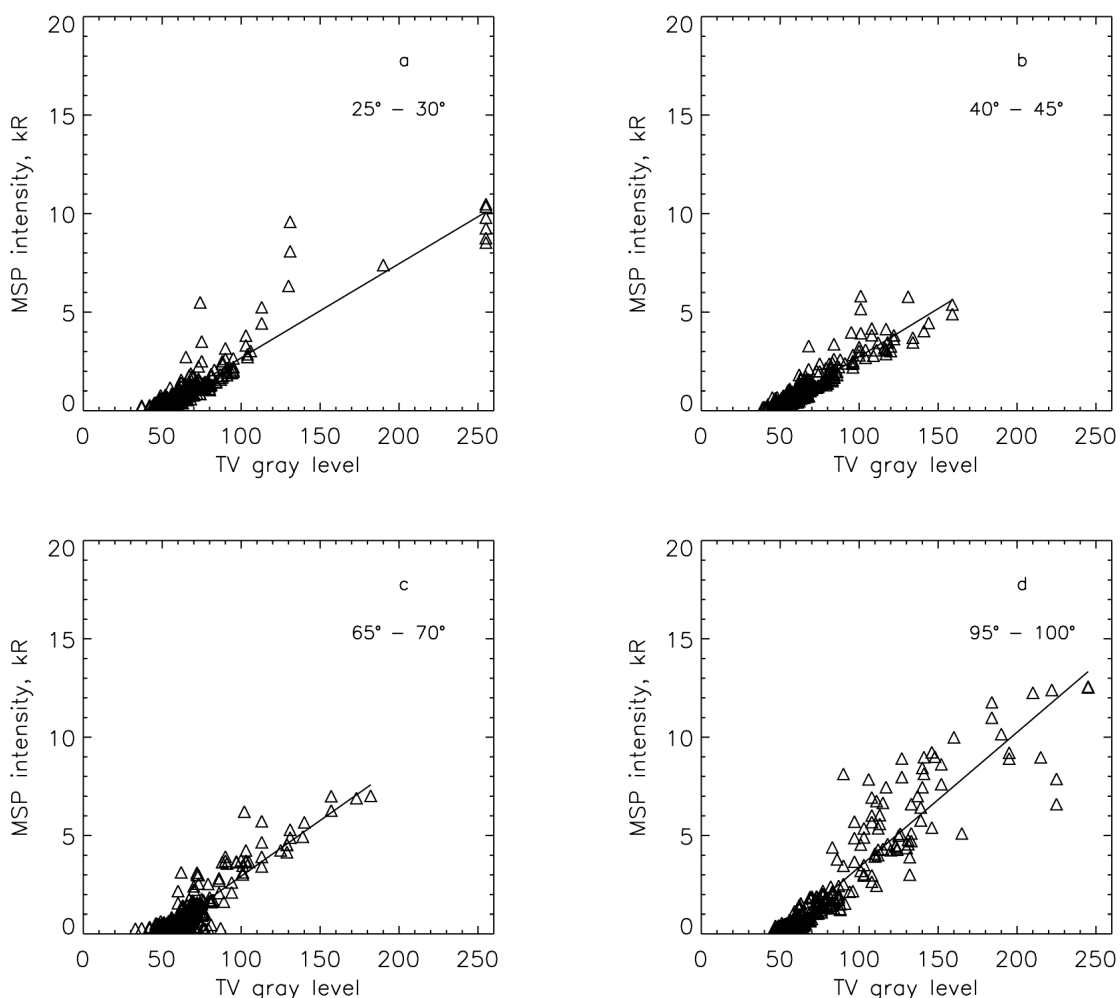


Fig.6. Examples of dependence of intensity of the 557.7 nm auroral emission (from MSP data) as a function of TV gray level for 5-degrees view angle interval. Lines are interpolations by (1).

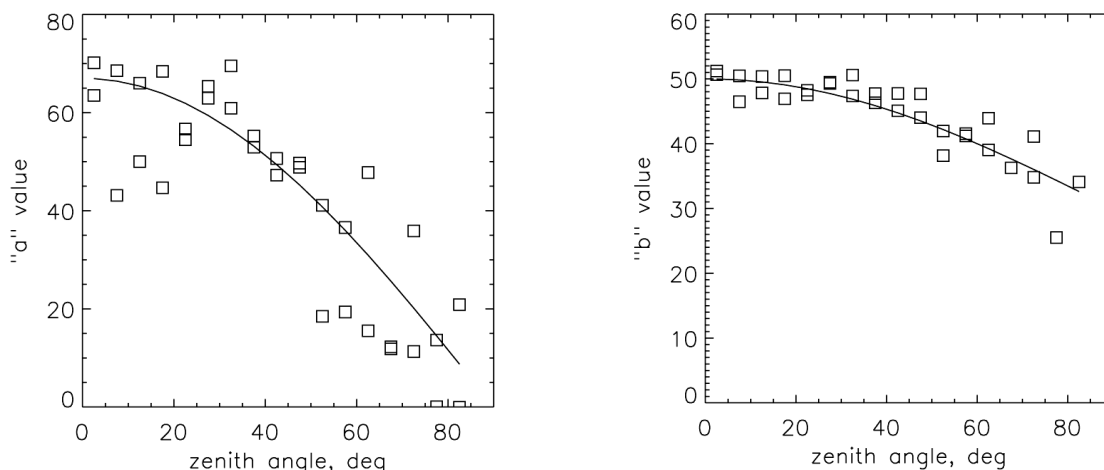


Fig.7. Interpolation of zenith angle dependency. Symbols -parameters of a and b in (1) as functions of zenith angle; lines – fitted functions by (2).

The dependencies is interpolated by linear function:

$$I = a(L - b), \quad (1)$$

where a and b are fitted parameters, L is TV gray level, I is auroral intensity by MSP data. Then, obtained values of a and b were fitted as functions of zenith angle (see Fig.7):

$$\begin{aligned} a &= 67 \cos \varphi \\ b &= 20 \cos \varphi + 30 \end{aligned} \quad (2)$$

From (1) and (2) we obtain final expression:

$$I = 67L \cos \varphi + 2010 \cos \varphi + 1340 \cos^2 \varphi \quad (3)$$

IV. The expression (3) has been extended to full TV frame to calibrate auroral intensity level.

4 Discussion

A comparison of MSP keogram and surrogate keogram constructed from calibrated TV data is presented in Fig.8 and Fig.9 to demonstrate a quality of the offered calibration procedure. One can see that the calibrated surrogate keogram constructed from TV data reproduced reasonably well the fine small-scale structure of bright (>2 keV) aurora observed by the scanning photometer. However, background noise in the surrogate keogram is much higher than in MSP data. Also there are additional linear structures from the stars that are not observed in 557.7 nm emission of MSP.

The same calibration procedure was carried out by 427.8 nm emission spectral band. It was found that in bright aurora the relation between calibrated intensity levels for case 557.7 nm and 427.8 nm is ~ 5 that corresponds well to theoretical value of these relation. So, we can

pass from the auroral intensity in specific emission (557.7 nm or 427.8. nm) to energy flux of precipitated electrons. However, an estimated discrepancy of the calibration procedure is not better than 50% for energy flux of precipitated electrons in range of 1-10 $\text{erg cm}^{-2} \text{s}^{-1}$.

The calibration procedure has been used in paper [Kozelov et al., 2004] to study statistical distributions of the characteristics of the auroral blobs during substorm intensifications.

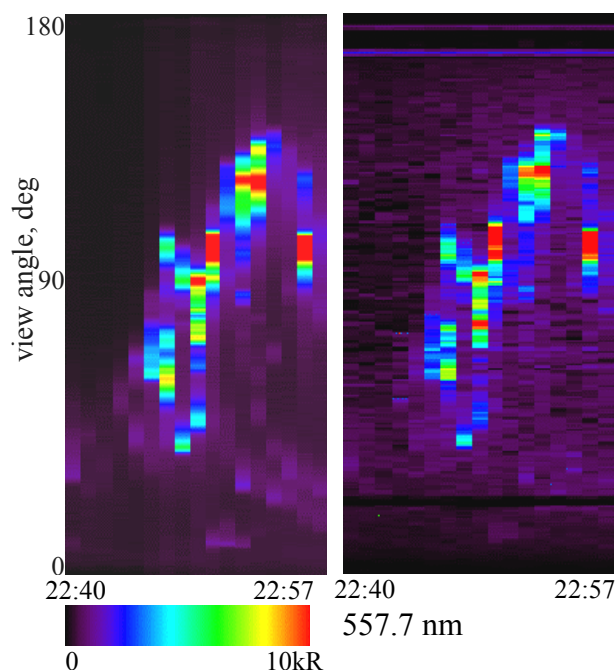


Fig.8. A comparison of MSP keogram (left panel) and surrogate keogram (right panel) constructed from calibrated TV data for 22:40-22:57 UT, 19 January 2001

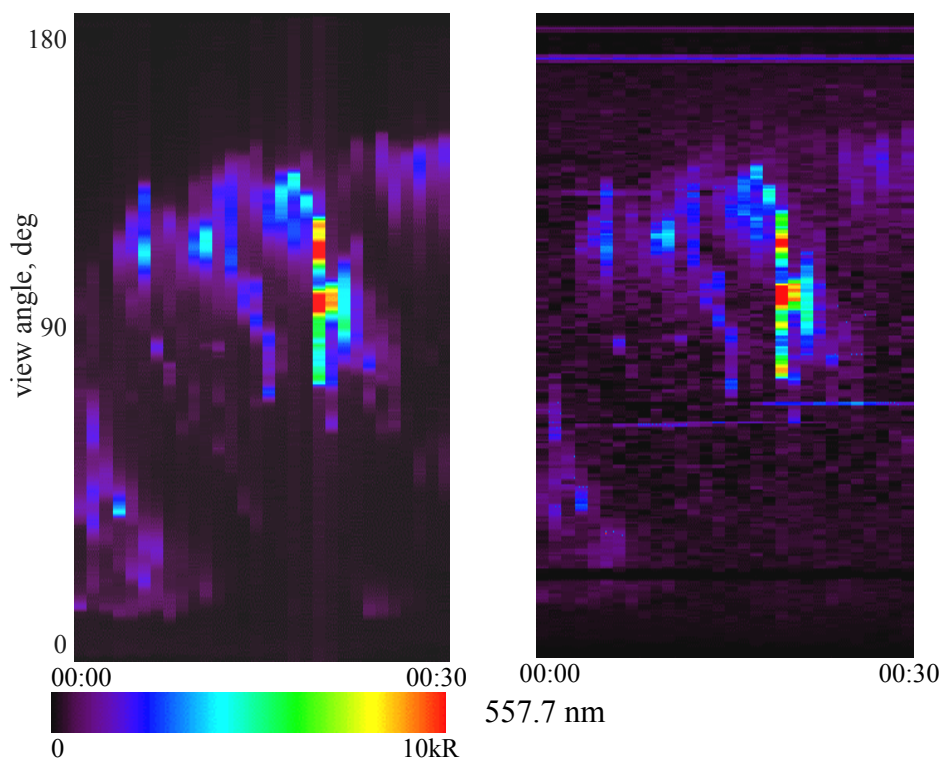


Fig.9. A comparison of MSP keogram (left panel) and surrogate keogram (right panel) constructed from calibrated TV data for 00:00-00:30 UT, 20 January 2001

5 Conclusions

1. A procedure of calibration of image intensity in TV data by data of simultaneous photometry observations is presented.
2. An example of such calibration by data of PGI instruments located at Barentsburg (Svalbard) is described.
3. It was found that the calibrated surrogate keograms constructed from TV data reproduced reasonably well the fine small-scale structure of bright aurora observed by the scanning photometer.

Acknowledgements. The work was partly supported by the basic research programs of the Division of Physical Sciences of RAS "Plasma processes in the solar system". Author thanks Polar Geophysical Institute for data of optical observations at Barentsburg Observatory and the organizing committee of the 31AM for support of his participation in the meeting.

References

- Lyons, L. R., Koskinen, H. E. J., Blake, J. B., Egeland, A., Hirahara, M., Oieroset, M., Sandholt, P. E., and Shiokawa, K.: Processes leading to plasma losses into the high-latitude atmosphere, in: Magnetospheric plasma sources and losses, Space Science Series of ISSI, vol.6, edited by Hultqvist, B., Oieroset, M., Paschmann, G., and Teumann, R., Kluwer, Dordrecht, 85–136, 1999.
- Kozelov, B. V., Uritsky, V. M. and Klimas, A. J., Power law probability distributions of multiscale auroral dynamics from ground-based TV observations, *Geophys. Res. Lett.*, V. 31, L20804, doi:10.1029/2004GL020962, 2004.

Irregular pulsations in simultaneous TV, IRIS and VLF observations

B.V. Kozelov¹, E.E. Titova¹, J. Manninen², F. Honary³, S. Marple³, T. Turunen²

¹ Polar Geophysical Institute, Apatity, Murmansk region, Russia

² Sodankylä Geophysical Observatory, Finland

³ Dept. Communication Systems, Lancaster University, United Kingdom

Abstract. The models of VLF emission generation are based on cyclotron wave-particle interaction mechanism. According to such models the generation of waves is accompanied by a modification of particles pitch-angle distribution, that can lead to their precipitation in a loss cone. The dissipation of energetic particles in the atmosphere is accompanied by excitation of auroral emissions at altitudes of 100-200 km, that is observed by optical instruments. If the precipitated particles are rather energetic to penetrate at altitudes below than 90 km, the ionization by them of atmospheric gases leads to an absorption of radiowaves, that is observed by riometers. However, to find direct correlation between VLF waves and particles precipitation is complicatedly. Only a few papers with examples of such correlation are known. In this report we consider simultaneous morning time observations of VLF antenna, IRIS riometer array, and TV all-sky camera located at Kilpisjärvi and Porojarvi, Finland. We used the continuous wavelet transformation of original data sets to find similarities in variations seen at time scales from 1 to 100 seconds.

Keywords: 2407 Auroral ionosphere, 2483 Wave-particle interactions, 2704 Auroral phenomena, 2716 Energetic particles, precipitating, 2431 Ionosphere-magnetosphere interactions

1. Introduction

Pulsing electron precipitations are usually considered connected with developing of the instability in the magnetosphere [Trakhtengerts, 1984, Davidson, 1990, Trefall et al., 1975]. Simultaneous registration of such events as pulsing auroral forms, riometric absorption and ELF/VLF choruses in morning sector is usual for recovery phase of substorm and supports this point of view. [Helliwell, 1965, Tagirov, 1986,]. However one-to-one correspondence for variations of precipitated electron flux and ELF/VLF waves is observed seldom [Tsuruda et al., 1981, Rosenberg et al., 1971, Helliwell et al., 1980, Tagirov et al. 1999]. It can be explained by features of low-frequency electromagnetic waves propagation in the

magnetosphere and ionosphere of the Earth. The ray trajectories of nonductedly propagating ELF/VLF waves oblique from a magnetic field line that can essential displace an exit point of the wave from L-shell of generation region [Huang, 1883]. Reflection and absorption of low-frequency waves in the lower ionosphere also hinder the ground-based observations of VLF waves.

However, search of connection between precipitated electrons and ELF/VLF emissions is very important for the analysis of wave-particle interaction and non-stationary magnetospheric processes. Observations of aurora by highly sensitive television (TV) cameras and riometric absorption by IRIS image riometer allows ones to research spatial-temporal dynamics of precipitated particles. Here we present some results of an analysis of simultaneous observations of ELF/VLF emissions, aurora and riometric absorption for two events of 8 and 12 January 1997.

2. Geometry of observations

In this report we consider simultaneous observations of VLF antenna, IRIS riometer array, and television all-sky camera located at Kilpisjärvi and Porojarvi in northern Finland.

The Imaging Riometer for Ionospheric Studies (IRIS) [Browne *et al.*, 1995] is located at Kilpisjärvi in northern Finland, (69.05° N, 20.79° E). IRIS samples the cosmic radio noise at 38.2 MHz and consists of an imaging array (7x7 imaging beams) and a single, wide beam riometer. The whole array is sampled every second.

The television all-sky camera (TVASC) was located at Porojarvi (69.17° N, 21.47° E) and observed the aurora in "white" light with a broad maximum at blue-green wavelengths. The TV data were recorded by a VHS recorder in a PAL video system, at 25 images per second. The TV data were digitized using an Acorn TV-Capture plate with an output resolution of 5 images per second, 160x144 pixels, 8 bits per pixel.

Stereo sound track of VHS video tape used to store ground-based observations of ELF/VLF electromagnetic waves up to 20 kHz. The signal was digitized with sampling rate 44.1 kHz, 16 bit per channel, simultaneously with TVASC data.

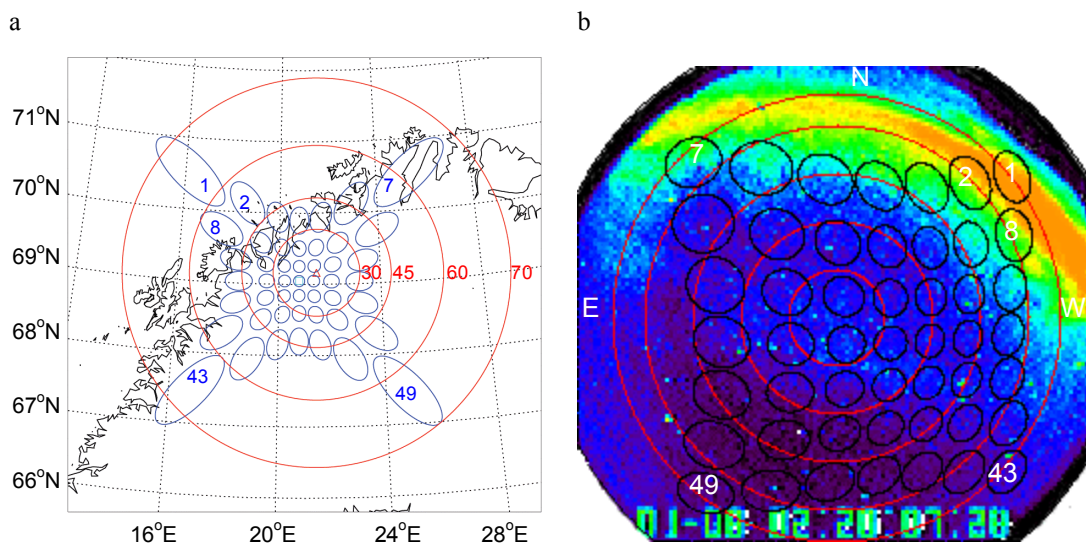


Figure 1. Geometry of observations for IRIS and Porojarvi TV all-sky camera: a – map of projections of IRIS beams to 110 km (blue ovals and numbers) and all-sky camera (red circles for zenith angles of 30°, 45°, 60° and 70°); b – projections of IRIS beams to 110 km in all-sky camera field of view (black ovals), red circles show zenith angles of 15°, 30°, 45°, 60° and 70°.

3. Selected events

For the analysis we chose two morning events, during which occurrence and the increase of discrete chorus activity was accompanied by gradual approximation of band of pulsing auroral forms. We hoped, that the gradual development of an observable phenomenon gives us possibility to clarify a connection between wave activity and particle precipitation.

The dynamic spectrum of waves during event of January 8 is shown in Fig.2 together with keograms, constructed by IRIS and TV data. Section of the field of view for keograms were taken approximately along the magnetic meridian (~30 degrees from north to west relative to geographic meridian).

The TV keogram demonstrates the southward movement of a boundary of the pulsing auroral patches that formed arc-like structures. Same movement is seen in IRIS keogram. The boundary of the pulsing patches corresponds to the equatorial boundary of the auroral oval, well seen from the DMSP F13 satellite, Fig.3.

The dynamic spectrum of the electromagnetic waves (Fig.2-a) shows that ELF/VLF chorus observed from 450 to 1500 Hz and the top frequency of the ELF/VLF chorus increases during this event. ELF/VLF waves observed permanently at frequencies < 400 Hz and > 1800 Hz relate with discrete atmospheric emissions (sferics).

Second event, January 12, 1997, has the same morphology, but some slower. We can note that both event were observed during mainly quiet conditions after small substorm-like intensification, Table 1.

Table 1. Geophysical conditions during considered events.

	January 8, 1997 02:20-02:35 UT	January 12, 1997 05:20-05:35 UT
Dst	<10	~10
Kp	3	2
AE	~200	<100

4. Spatial regions of correlation

Whether there is a connection between the particle precipitation causing riometric absorption and optical aurora? For the answer to this question there were selected the virtual photometers appropriate to projections of IRIS beams in TV ASC frames on an altitude 110 km. We compare variations of a spatial-integrated intensity of TV signal in each virtual photometer with variations of absorption in the appropriate beam of IRIS. The figure 4 by color code presents results of calculations of linear Pearson correlation coefficient between values of riometric absorption and auroral intensity in each IRIS beam. The numbers designate numbers of beams. One can see, that aurora and riometric absorption are well correlated in northern part of the field of view, for some beams the correlation coefficient reaches values of ~0.8.

Whether it is possible to localize a spatial area of particle precipitation connected with measured chorus emissions? The frequency band, in which the chorus were observed, was divided into 3 bands: 450-700 Hz, 700-1000 Hz and 1.0-1.5 kHz. The correlation coefficient between intensity of waves in each band and data of IRIS and TV ASC are shown in a Figure 5. From figure 5 we can conclude:

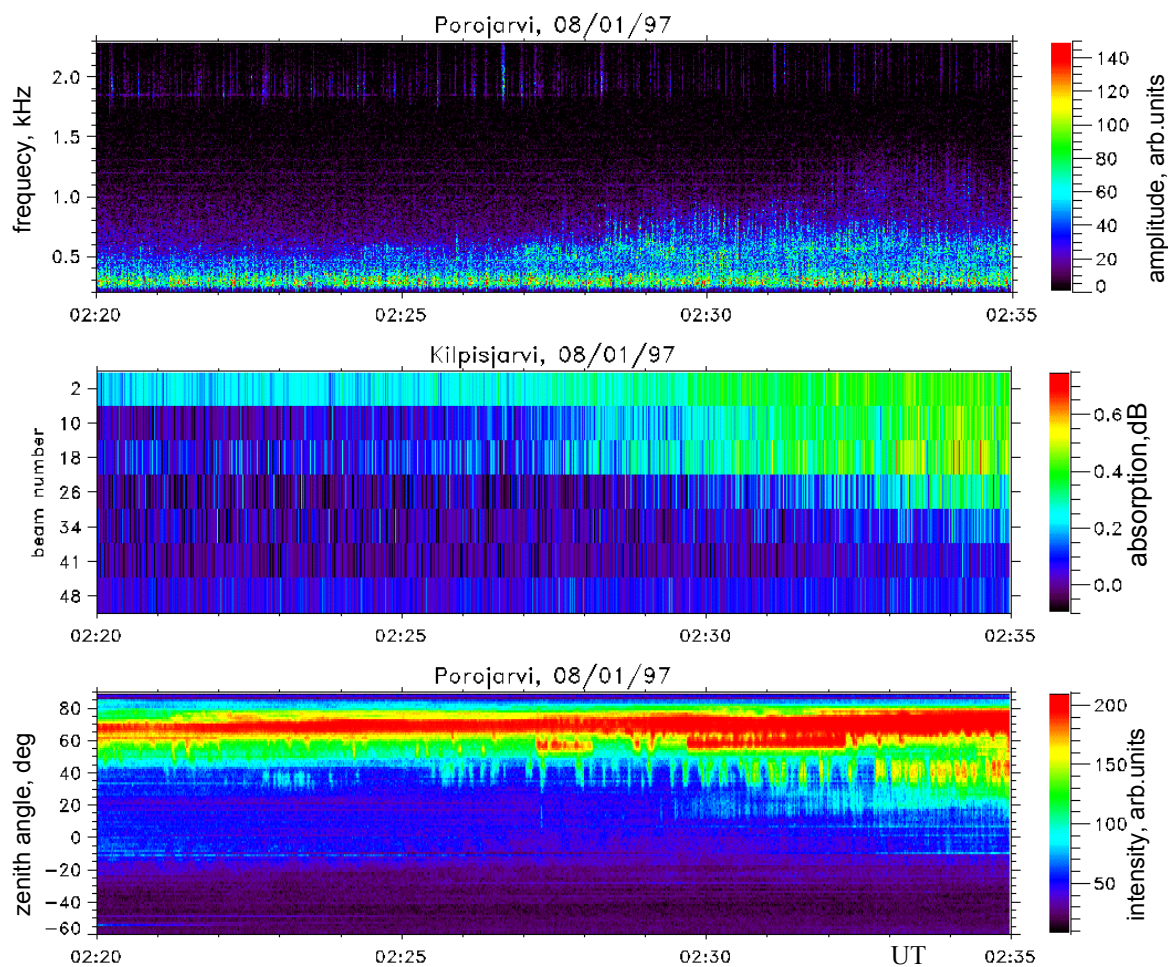


Figure 2. Dynamics of ELF/VLF activity and particle precipitations during event of January 8, 1997: a - dynamical spectra of ELF/VLF waves; b - keogram of riometric absorption from IRIS data; c - TV ASC keogram. The keograms were taken along the magnetic meridian.

1) The waves correlate better with the data of an IRIS (correlation coefficient reaches value of 0.7), than with TV (correlation coefficient is not more than 0.4).

2) Waves in the lower band of 450-700 Hz is better correlated with riometric absorption.

3) There is a region of anti-correlation (correlation coefficient ~ 0.4) of waves in band of 450-700 Hz and optical aurora. This is a region of oscillated boundary of sub-visual diffuse aurora, the boundary is well seen in figure 2-c at -20 zenith angle. This diffuse aurora decreases during the event, so we have anti-correlation with increasing wave activity.

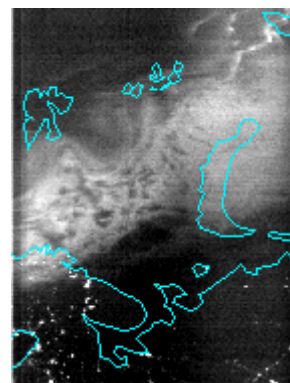


Figure 3. Auroral structure observed by DMSF F13, 08 January 1997, 02:45 UT.

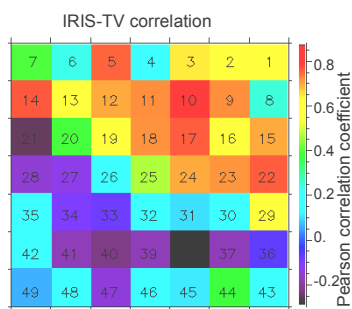


Figure 4. Correlation between absorption in IRIS beams and optical emissions in correspondent regions of the TV all-sky image during event of 08 January 1997, 02:20-02:35UT. Value of linear Pearson correlation coefficient presented by color coding in IRIS beams array. Note, that the scintillation due to Cassiopeia is located in beam 4, and due to Cygnus - in beams 6 and 7.

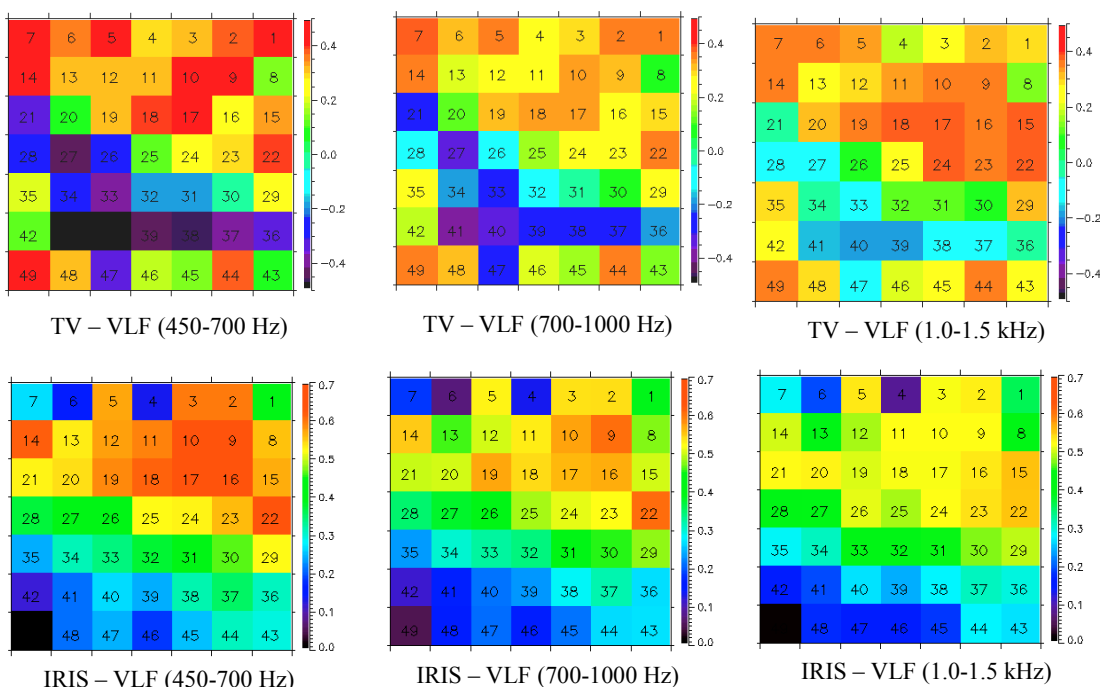


Figure 5. Spatial distribution of correlation between particle precipitation and ELF/VLF waves in three frequency bands during event of January 8, 1997, 02:20-02:35UT: top row- for TVASC data, bottom row - for IRIS data. Value of linear Pearson correlation coefficient presented by color coding in IRIS beams array. Note, that for bottom row the scintillation due to Cassiopeia is located in beam 4, and due to Cygnus - in beams 6 and 7.

5. Top frequency of chorus and position of generation region

The increase of top frequency of chorus band deserves special attention. Whether it is possible to connect the observed increase of top frequency of chorus emissions with a possible position of generation region? The characters in Figure 6 mark the top frequency of chorus depending on a latitude of equatorial boundary of pulsing patches (by IRIS and TVASC data). The solid lines show the latitude dependence of a half of electron gyrofrequency calculated by values of equatorial magnetic field according to the magnetospheric model of Tsyanenko-96 [Tsyanenko and Stern, 1996]. One can see, that for two considered events the experimental and theoretical dependencies of the frequencies are close.

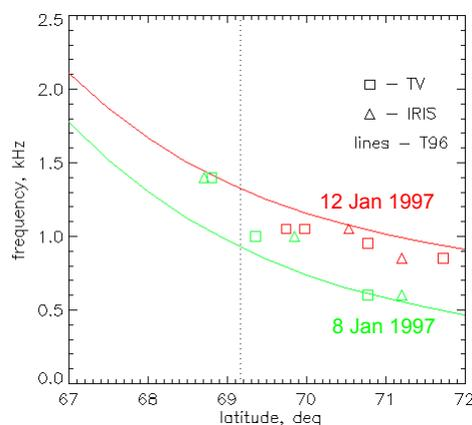


Figure 6. Comparison of observed top frequency of chorus band as a function of latitude of equatorial boundary of pulsing patches and $f_H/2$ calculated by Tsyanenko-96 magnetic field.

6. Pulsations at scales 1-100 s

Correlation coefficients discussed in section 4 were calculated for full interval (15 minutes) and characterize large-scale changes of considered signals. Whether it is possible to find time intervals of one-to-one conformity of small-scale variations of measured signals?

For this analysis we used the continuous wavelet transformation (CWT), because these variations can be irregular. The Morlet wavelets of 6 order were used for the transformation. Wavelet analysis has shown, that there is no periodic structure in VLF signal at time scales from 1 to 100 seconds. The examples of wavelet-spectra of considered signals for beam 17 are shown in a figure 7.

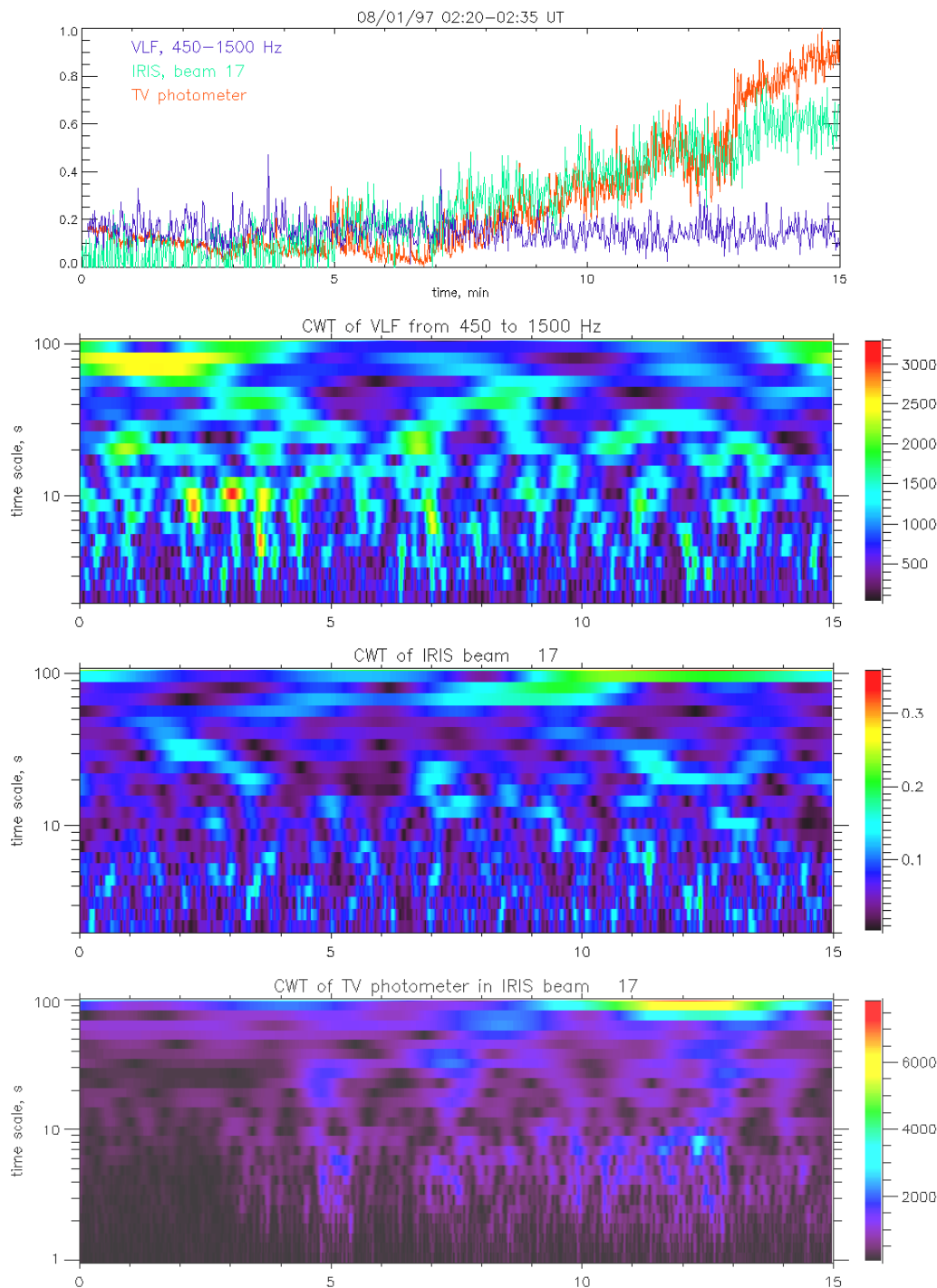


Figure 7. Analysis of small scale variations of three kind of signals: ELF/VLF waves integrated from 450 to 1500 Hz; beam 17 of IRIS; TV ASC virtual photometer in projection of beam 17. Considered signals is shown in top panel, other panels are continuous wavelet transformations of the signals.

The power spectra of the signals were obtained by integration of wavelet-spectra from figure 7 along the time axis. The power spectra are shown in figure 8. Obviously, that despite of large values of a coefficient of correlation (figures 4 and 5), the one-to-one correspondence between variations of signals on small scales is absent. Moreover, it is possible to say, that for considered events it is impossible to find a continuous conformity between small-scale variations of waves and particle precipitation in any fixed position in the sky. Detailed study of a beginning of January 12 event has shown, that the groups of chorus elements may be associated sometimes with pulses of aurora patches near aurora boundary. The Fig. 9 demonstrate this relationship, however location of aurora patches are different. The position of the three series patches is shown in figure 10.

However, at small scales it is possible to find anti-correlation between ELF/VLF chorus and particle precipitation also. Such example is presented in figure 11, where series of chorus elements is observed between pulses of aurora. This event may be explained by reflection or/and absorption of waves in the ionosphere. The reflection and absorption conditions is strongly depends on altitude profile of electron density which varies by precipitated particles [Bespalov, 2004].

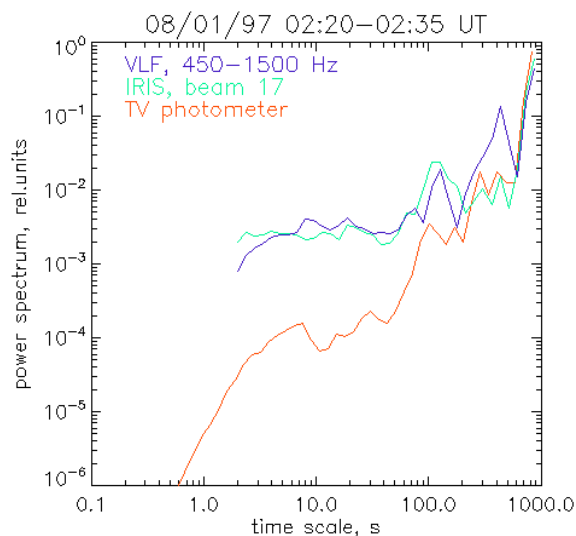


Figure 8. Power spectra for signals from fig.7

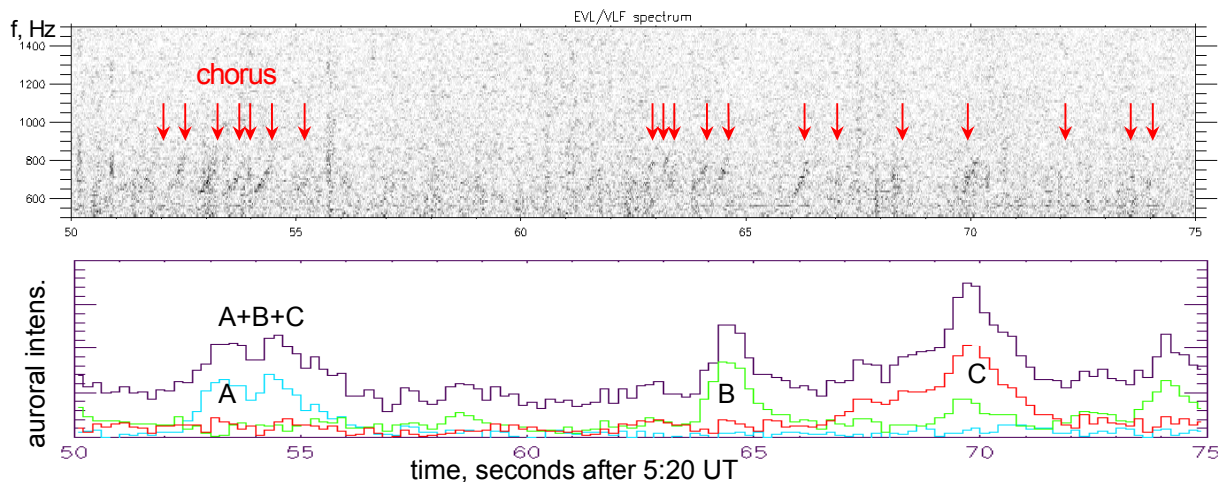


Figure 9. Example of small scale correspondence of the ELF/VLF chorus and pulses of aurora. Top panel is a dynamical spectra of ELF/VLF waves, chorus elements are marked by arrows. Bottom panel presents variation of auroral intensity in three virtual photometers (A,B, and C) on the TB ASC field of view. Positions of the virtual photometers are shown in figure 10.

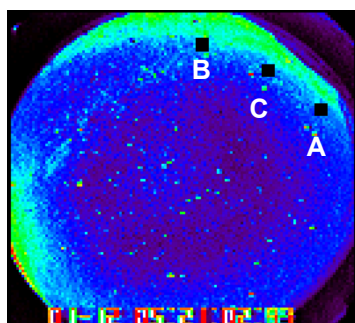


Figure 10. Positions of the virtual photometers used in figure 9.

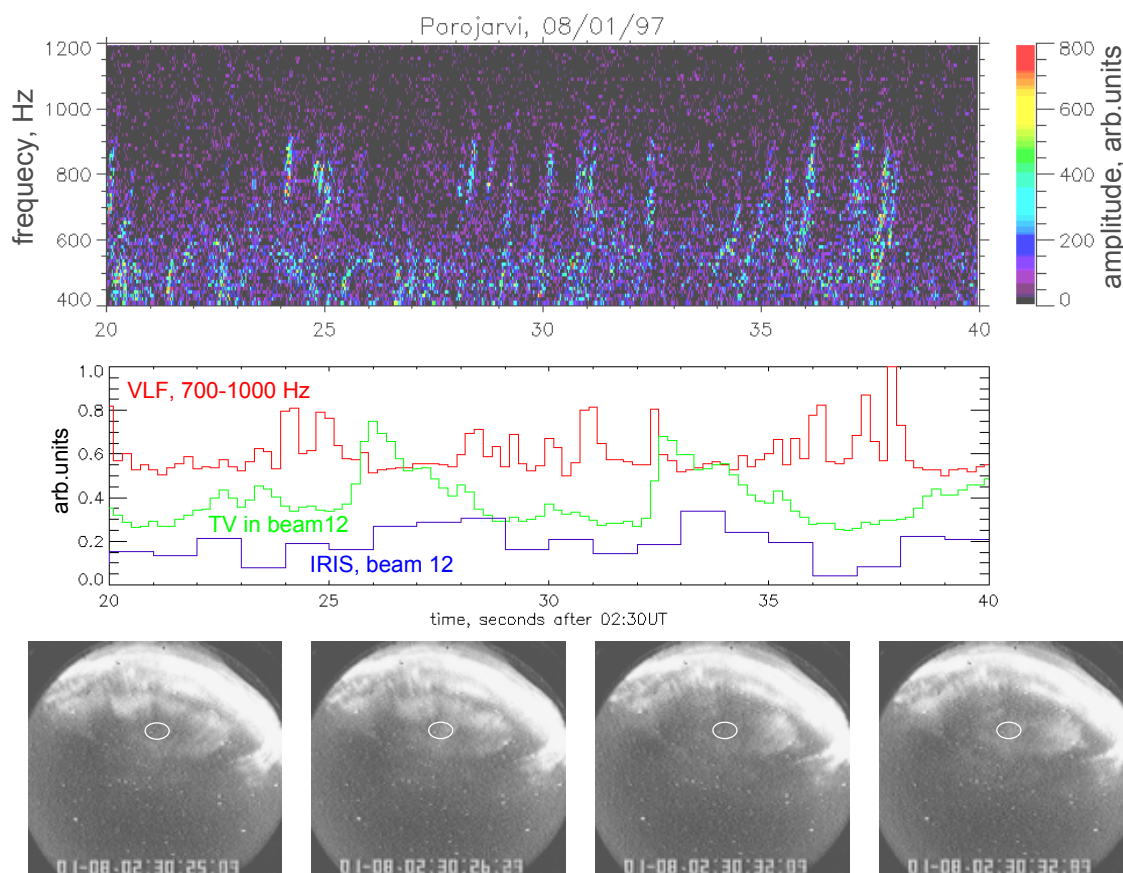


Figure 11. Example of anti-correlation between VLF and particle precipitation, time interval 02:30:20-02:30:40 of 08 January 1997: top panel – dynamic spectrum of ELF/VLF waves; middle panel – variations of ELF/VLF waves integrated from 70 to 1000 Hz, riometric absorption in beam 12 of IRIS, and auroral intensity in projection of beam 12 on TV ASC field of view; low panel – examples of TV ASC frames.

7. Conclusions

We consider two events of simultaneous morning time observations of VLF antenna, IRIS riometer array, and TV all-sky camera located at Kilpisjärvi and Porojarvi, Finland. During these events the band of pulsing aurora approached on area of observations from northwest. This motion was accompanied by appearance and increasing of ELF/VLF emissions.

Wavelet analysis has shown, that usually there is no periodic structure in VLF signal at time scales from 1 to 100 seconds.

The waves correlate better with the data of an IRIS (linear Pearson correlation coefficient for some beams reaches value ~ 0.7), than with TV (correlation coefficient is not more than 0.4).

There is no one-to-one prolonged correspondence between pulses in VLF, optical aurora and riometer absorption. However during some time intervals at a weak VLF signal with rare discrete elements it is possible to find such correspondence. The analysis of appearance of chorus

elements in the band 0.5-1.1 kHz and optical pulsation on auroral emission boundary has shown, that the optical pulses correspond to groups of choruses. Position of the pulses at the boundary is changing.

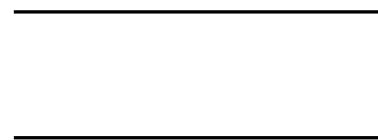
However, it is possible to find time intervals of not only correlation, but also anti-correlation between ELF/VLF chorus and particle precipitation.

It was found that the observed increase of top frequency of chorus emissions is possible connected with position of generation region in the magnetosphere.

Acknowledgements. The work was partly supported by the basic research program of the Division of Physical Sciences of Russian Academy of Sciences "Plasma processes in the solar system", by the grants INTAS 03-51-4132 and RFBR 04-05-64955. BVK thanks the Organizing Committee of 31 AM for support of his participation in the meeting. Authors thanks site at <http://sd-www.jhuapl.edu/Aurora> for auroral images from DMSP F13 satellite.

References

- Bespalov, P.A., and Mizonova, V.G., Reflection coefficient of whistler mode waves normally incident on the ionosphere, *Geomagnetizm i aeronomia*, 44, 55-59, 2004.
- Browne, S., Hargreaves, J. K., and Honary, F. An Imaging Riometer for Ionospheric Studies, *Elect. Comm. Eng. J.*, 7, 209–217, 1995.
- Davidson, G. T., Pitch-angle diffusion and the origin of temporal and spatial structures in pulsating aurorae, *Space Sci. Rev.*, 53, 45-82, 1990.
- Helliwell, R. A., Whistlers and related ionospheric phenomena, Stanford University Press, Palo Alto, Calif., 1965
- Helliwell, R. A.; Doolittle, J. H.; Armstrong, W. C.; Carpenter, D. L.; Mende, S. B. Correlation between lambda 4278 optical emissions and VLF wave events observed at L approximately 4 in the Antarctic. *Journal of Geophysical Research*, vol. 85, July 1, p. 3376-3386, 1980.
- Huang, C. Y.; Goertz, C. K., Ray-tracing studies and path-integrated gains of ELF unducted whistler mode waves in the earth's magnetosphere, *Journal of Geophysical Research*, 88, 6181-6187, 1983.
- Rosenberg, T. G., R. A. Helliwell, and J. P. Katsufakis, Electron precipitation associated with discrete very low frequency emissions, *J. Geophys. Res.*, 76, 8445-8456, 1971
- Tagirov, V. R., V. Y. Trakhtengerts, and S.A. Chernouss, The origin of pulsating auroral patches, *Geomagn. Aeron.*, 26, 501-505, 1986.
- Tagirov V. R., V. S. Ismagilov, E. E. Titova, V. A. Arinin, A. M. Perlikov, J. Manninen, T. Turunen, and K. Kaila, Auroral pulsations and accompanying VLF emissions, *Ann. Geophysicae* 17, 66-78, 1999.
- Trakhtengerts, V.Y., Relaxation of plasmas with anisotropic velocity distribution. In: Galeev, A.A., Sudan, R.N. (Eds.), *Handbook of Plasma Physics*, Vol. 2, Basic Plasma Physics II. Elsevier, New York, pp. 519-552, 1984.
- Tsyganenko, N.A. and D.P. Stern, A new-generation global magnetosphere field model, based on spacecraft magnetometer data, *ISTP Newsletter*, V.6, No.1, P.21, 1996.
- Trefall, H. , S Ullaland, J. Stadsnes, I. Singstad, T. Pytte, K. Bronstad, J. Bjordal, R. Karas, R. Brown, J. Muench, Morphology and fine time structure of an early-morning electron precipitation event, *J. Atmos. Terr. Phys.*, 37, 83-105, 1975.
- Tsuruda, K. S.; Machida, T. Oguti, S. Kokubun, K. Hayashi, T. Kitamura, O. Saka, T. Watanabe, Correlations between the very low frequency chorus and pulsating aurora observed by low-light-level television at L approximately 4.4. *Canadian Journal of Physics*, vol. 59, p. 1042- 1047, 1981.



Aurora, currents and particle dynamics in the inner magnetosphere: case study of multiple-onset substorm of March 12, 1991

Lazutin L.¹, T. Kozelova², M. A. Danielides³, N. Meredith⁴, B. Kozelov², J. Jussila³, and A. Korth⁵

¹Science Division, Scobeltsyn Institute for Nuclear Physics of Moscow State University, Russia,

²Polar Geophysical Institute, Apatity, Russia

³Space Physics Group, University of Oulu, Finland

⁴Mullard Space Science Laboratory, UK

⁵Max-Planck Institute for Aeronomie, Lindau, Germany

Abstract. We study substorm signatures in the ionosphere and in the magnetosphere during a selected event on 12 March 1991. This event, of a moderate complexity, was a sequence of optical pseudo-breakups and a double breakup followed by a large substorm expansion. The auroral dynamics were recorded by TV and four all-sky cameras over Scandinavia. The data from an array of ground-based magnetometers in the sector of geomagnetic longitudes from $\sim 80^\circ$ to 155° were used. Simultaneously we analyzed the observations from CRRES near the earthward edge of the plasma sheet westward of the substorm onset sector. One of the substorm intensifications occurred close to the CRRES location. We find it difficult to fit this substorm with the simple substorm model and propose a scheme involving a combination of global and local processes. The ion and electron substorm injections have different origins. The electron increase closely correlates with the magnetic field dipolarization, whereas the energetic proton increase starts about 2 minutes before the onset and 4-5 minutes before the magnetic field dipolarization. The ion energy density increases several minutes before the local activations and decreases immediately after onset. The low energy (<15 keV) and high energy (>50 keV) ions are the two species primarily involved in substorm activity, whereas the middle energy ions remain passive during late growth phase and expansion time. The importance of the quasitrapped ions with energy higher than 50 keV deserves special attention and we suggest that ion acceleration is of the resonant interaction with the auroral arc curl structures. The increase in the auroral electron flux during the substorm expansion is a composition of field-aligned, inductive and betatron acceleration and magnetic drift shell radial displacement. The latter prevails for the high energy electrons, the pure acceleration effects for the soft particles, and a combination of betatron acceleration and drift shell displacement for the middle-energy auroral electrons. We were able to trace transformation of the central plasmashet 0.1-10 keV electrons into 10 - 100 keV auroral electrons which

creates most of known precipitation effects and supplies the radiation belts with fresh particle flux. We investigated the fine structure of the local onset in the vicinity of the CRRES at 2046-2048UT. For the first time we show that keV field-aligned electrons (and upward current) arrived in front of energetic electron increase and dipolarization. The transformation of energy spectrum of the middle-energy electrons differs from the accelerated by betatron mechanism and suggest induced electric field or other types of acceleration. Ion and electron substorm injections are the result of local acceleration in the quasitrapping region without transport from the magnetotail region. Several steps of the acceleration can be assumed, with the ionosphere as an initial source of low energy inner plasmashet population later transformed into auroral and trapped radiation.

1 General substorm structure

The classic substorm model includes growth phase, onset, active phase with expansion phase as a part of it, and the recovery [Akasofu (1968)]. All these elements are usually seen in any real substorm but in a more mixed, complicated combination. Several important features were included into the substorm scheme by Rostoker et al. (1980) and found in numerous case studies. Our goal for the first part of this study is to examine the existing scenario of the substorm onset and, in particular the transition from the growth to the active phase. This question attracts considerable attention. There are no accepted descriptions on what is going on several minutes before the onset. For example, are there any precursors?, which observation (Pi2, aurora brightening, start of injection etc.) is the best indicator of the substorm onset? There are no accepted schemes of the substorm onset. However, there are suspicions that it is not a single action. Indeed, a two-step transition to the active phase or synthesis of different mechanisms were discussed (see for example Lui (1991); Elphinstone et al. (1996); Voronkov et al. (2002)).

Correspondence to: Lazutin L. (lazutin@srd.sinp.msu.ru)

Lazutin L. et al.: Case study of multiple-onset substorm of March 12, 1991

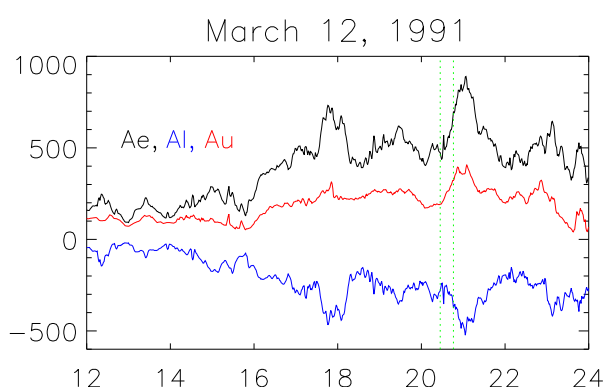


Fig. 1. Ae index during 12.03.91 substorm activity. Dotted lines show time of the substorm onset and local activation.

The substorm expansion phase usually develops in a restricted longitudinal sector, while in other sectors the growth phase may continue or some independent activity take place. As a result, several intensifications are usually observed during a substorm, each showing signatures of the onset and expansion types of activity. The transition from one intensification to the next is not smooth, but impulsive. It can be applied, for example, to the westward travelling surge, which is actually not traveling but jumping [Vorobiev and Rezhnev (1973)]. Even inside the currently active sector the observations depend on the relative position of the instrument (observer) to the center of the local activation. Therefore, at the beginning of the case study we compile a map of the intensifications and the position of the instruments.

The day of March 12, 1991 from 1400 UT was moderately disturbed with several substorms of increasing intensity as monitored by the AE index (Figure 1). We will discuss the substorm with onset registered at 2026–2028 UT that gradually reached AL of about - 500 nT at 2100 UT. The auroral magnetosphere was enhanced by previous activity and therefore the development of the activity was more complicated than an ideal isolated substorm. A map of the Arctic region where activity developed is shown in Figure 2 and a list of ground-based stations deployed presented in Table 1.

1.1 Magnetometer data

The H components of the magnetometer records from the Scandinavian sector show that the gradual development of the AE index includes sharp intensifications when the magnetic station was located close to the intensification onset region (Figure 3). The first intensification occurred in the Apatity-Tromsø sector at 2026–2028 UT, the second shifted westward as represented by NOR magnetogram (2032 UT) and the last one or two intensifications were registered by the FAR and Jan Majen magnetometers at 2045–2052 UT. Along with this step-like (or WTS-like) westward expansion, the magnetometer of Dixon observatory ($\sim 45^\circ$ eastward from Apatity) shows that a new bay occurred here at 2040 UT. The

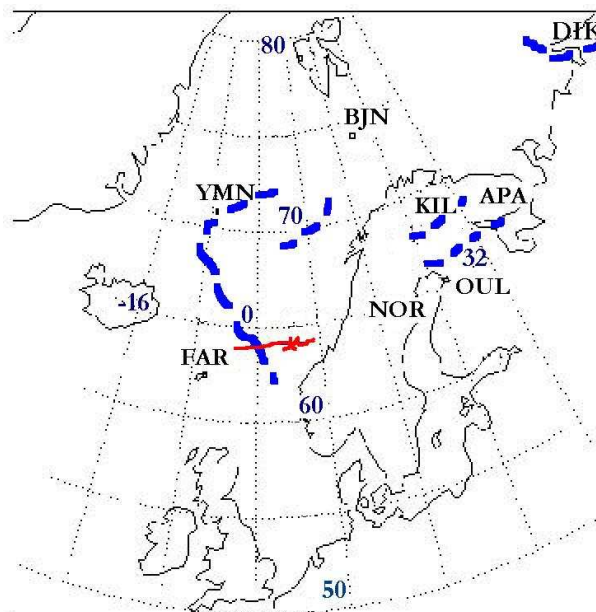


Fig. 2. The map with location of several ground-based stations. Red line: CRRES footprint, blue lines: auroral activity during substorm activity.

Table 1. Ground stations of this case study

abbrev.	name	geogr. lat ($^\circ$ N)	geogr. long ($^\circ$ E)	CGM lat ($^\circ$ N)	CGM long ($^\circ$ E)
APA	Apatity	67.58	33.31	63.86	112.9
BJN	Bear Island	74.50	19.20	71.45	108.07
BOR	Borok, CIS	58.03	38.33	54.06	113.41
DIK	Dixon	73.5	80.6	68.3	155.9
FAR	Faroes	62.05	352.98	60.72	77.44
KEV	Kevo	69.76	27.01	66.32	109.24
KIL	Kilpisjärvi	69.02	20.79	65.88	103.79
LOZ	Lovozero	67.97	35.08	64.23	114.49
MUO	Muonio	68.02	23.53	64.72	105.22
NOR	Nordli, Norway	64.37	13.36	61.50	94.92
NUR	Nurmjärvi	60.50	24.65	56.89	102.18
OUL	Oulujärvi	64.52	27.23	60.99	106.14
PEL	Pello	66.90	24.08	63.55	104.92
SOD	Sodankylä	67.37	26.63	63.92	107.26
TRO	Tromsø	69.66	18.94	66.64	102.90
YMN	Jan Mayen	70.90	351.30	70.29	82.93

Dixon and Apatity magnetic field H-components are compared in Figure 4. It is most probable that it was two independent substorms and that before 2040 UT the growth phase continued in the Dixon sector, as we will see from the satellite data.

The Pi2 burst of pulsations recorded at the Borok observatory are shown in Figure 5. Middle latitude Pi2 magnetic records summarize the substorm intensifications in a wide azimuthal sector of auroral region. Several onsets which will be discussed in our study coincide with peaks indicated in

Lazutin L. et al.: Case study of multiple-onset substorm of March 12, 1991

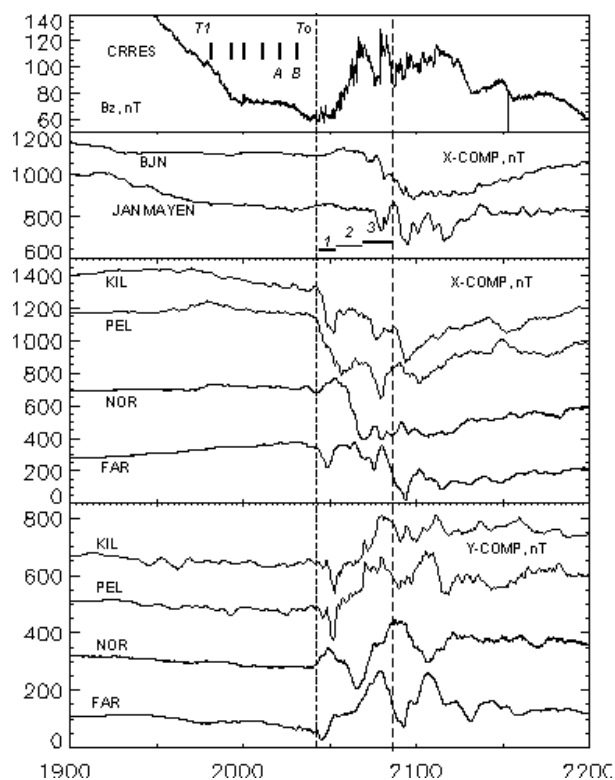


Fig. 3. Scandinavian ground-based magnetometers data, H-component.

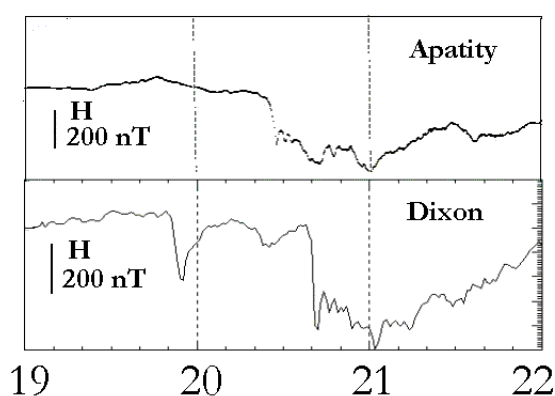


Fig. 4. Comparison of the magnetograms of Scandinavian (Apatity) and Dixon substorms.

this figure: A = 2022:15 UT, coincides with pseudobreakup in Scandinavian sector; B = 2026:25 UT, the first activation onset (T0); most intense peak C = 2028:40 UT coincides with the second activation onset (T1); D = 2040:44 UT, the Dixon substorm activation; E = 2048:50 UT, the local onset near the CRRES position. Several other peaks between C and D may be associated with substorm activations during impulsive substorm poleward expansion.

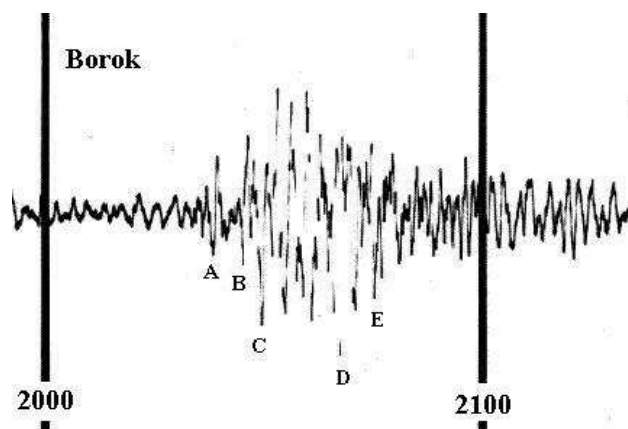


Fig. 5. Pi2-pulsations, Borok.

1.2 Current systems

The substorm onset took place on the geomagnetic meridian 120° near the geomagnetic latitude $\sim 62^\circ$ in the vicinity of the Harang discontinuity (HD). During the first intensification the westward substorm electrojet does not really push the HD further west on the FAR meridian, but rather suppresses the global current system locally. When this substorm intensification recovers, the global current system with eastward electrojet is reestablished (on the FAR). Only near the moment 2048 UT during third substorm intensification, the typical current picture associated with the leading edge of the substorm current wedge was observed over the meridian 80° and the region of westward electrojet established here. Just in this time CRRES observed fast local dipolarization and main dispersionless injection of energetic 21-150 keV electrons.

Figure 6 shows a sketch of the superimposed current systems around the HD and the substorm J_W similar to those presented by Opgenoorth et al. (1989). The westward expansion of the J_W can be identified with the CRRES transition from pre-HD to post-HD sector.

At 2041 UT magnetic activity began at BJN at $\varphi = 71^\circ$ and auroral brightening appeared northward of KIL. Two minutes after this time (in the interval 2043 - 2045:30 UT) the X decrease was observed simultaneously near FAR and KIL, near along $\Lambda \sim 65^\circ$. However, the upward FAC usually associated with the westward side of the SCW was located eastward or near KIL. At 2045:30 UT the clear onset of activity occurred at Jan Mayen at $\varphi = 73^\circ$, the weak N-S type auroral forms appeared above Scandinavia. In the equatorward part of the auroral oval ($\varphi \sim 63-65^\circ$), the upward FAC was located near or eastward of NOR. After 2048 UT pulsating auroras were observed near the poleward boundary of the diffuse auroral band near the latitude 63° . The typical current picture associated with the leading edge of the SCW appears suddenly over the meridian FAR and the region of substorm electrojet J_W established here. And CRRES positively was now eastward of the upward field-aligned current.

Lazutin L. et al.: Case study of multiple-onset substorm of March 12, 1991

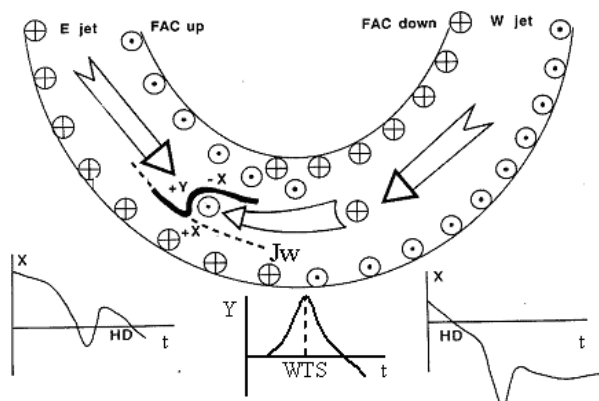


Fig. 6. Sketch of the 3-dim current system during substorm.

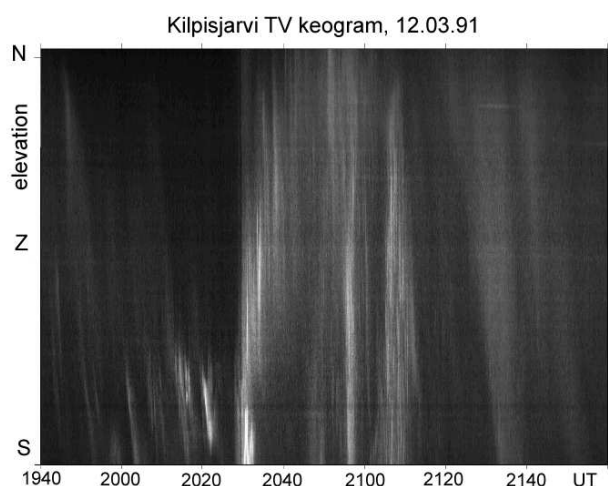


Fig. 7. Keogram, Kilpisjärvi TY records.

1.3 Aurora

For this event we have been able to obtain all-sky one minute snapshots from four stations (SOD, MUO, KIL and KEV) and TV film from Kilpisjärvi with a field of view restricted to approximately 15° above the horizon.

The growth phase is clearly seen on the TV records by the southward moving arcs. It was not movement from the horizon to horizon, rather most of the arcs became visible and brightened at the end of the trajectory. One brightening at 2021-2023 UT with active rotation can possibly be classified as a pseudobreakup. The keogram plotted from TV records provides a useful summary of the aurora dynamics (Figure 7).

Fast poleward expansion is seen on the keogram at 2031 UT. However, the first substorm activation onset was registered at 2026 UT to the South and the East off the field of view of the Kilpisjärvi TV, and southward of the SOD zenith.

1.4 CRRES and LANL

Geostationary satellite particle and magnetic field data have traditionally been used as an indication of the substorm development. Particle data from three LANL satellites and CRRES are available for our case study but all were not located exactly inside the onset and initial expansion region which has a typical azimuthal width of about 20° - 70° .

The CRRES and LANL-097 footprints were located 20° westward from Kilpisjärvi and westward expansion reached there with some delay. LANL-046 satellite, located in the morning side, detected drifting auroral ions and electrons with energy dispersion. LANL-095 was located in the Dixon azimuthal sector and the particle dynamics shown in Figure 8 are consistent with the development of the independent substorm at Dixon mentioned above. We observed a decrease of the particle flux (2015 UT) during the growth phase and fast recovery simultaneously with substorm onset. There is no reaction to the Scandinavian substorm onset (first dashed line). LANL-095 was entering in a dropout, away of the quasi-trapping region. Later there was no dynamic reaction to the CRRES local intensification at 2047 UT, only signature of the drifting auroral electrons. Therefore a substorm in Dixon region developed not as a continuation of the previous one but independently with the onset taking place when the Scandinavian substorm was still at the expansion phase.

1.5 Summary

On the background of previous disturbances the growth phase was observed over a wide nightside longitudinal sector (near 100°), (weak westward electrojet, southward moving arcs, dropout on LANL). Several local activation and the pseudobreakup were registered before the onset. Two seemingly independent substorms (with $\Delta t \sim 14$ min) were registered, partially overlapped in time in two azimuthally separated ($\Delta \lambda \sim 50$ - 60°) auroral sectors.

2 Late growth phase and onset structure

Auroral breakup is associated with the explosive substorm instability which is one of the most important substorm events. Investigation of the fine onset structure therefore attracts considerable attention. The commonly accepted description of auroral breakup denotes the sudden brightening of the most equatorward diffuse auroral arc as the main starting breakup point (Akasofu (1968); Isaev and Pudovkin (1972)). In a series of statistical studies based on POLAR auroral observations, Liou et al. (2003) found that auroral breakup starts earlier than other substorm onset signatures such as AKR, energetic particle injections, Pi2 and magnetic bays.

It is clear also that before the onset at the late growth phase there are some processes which may be important for the preparation of the onset instability, such as wave-like enhancements of activity with periods of 2-4 minutes, pre-onset auroral intensity decreases, so called fading effects when the auroral arc brightness decreases for a few minutes before To

Lazutin L. et al.: Case study of multiple-onset substorm of March 12, 1991

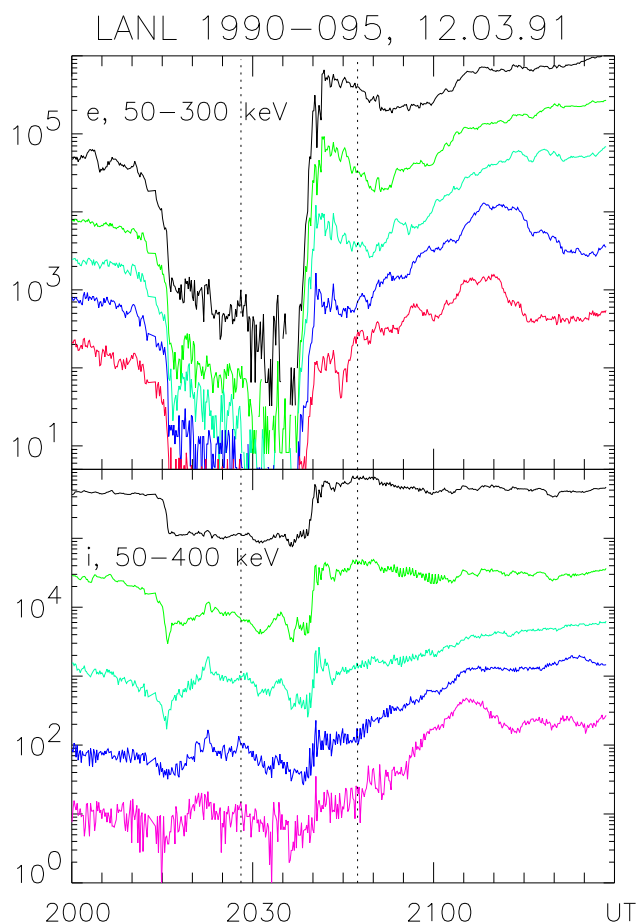


Fig. 8. LANL 095 energetic particle dropout and recovery. Several differential energy channels of electron (upper section) and ion (bottom section) detectors. Dotted lines show moments of the Scandinavian substorm onset and local activation.

[Pellinen and Heikkila (1978)], and pre-onset increases of the proton aurora [Fedorova et al. (1988)].

Recent studies with fine temporal resolution show that there are many details, both in particle dynamics and auroral development which are lost with one minute averaging and which might be extremely important for the understanding of the substorm development [Kornilova et al. (1990); Pudovkin et al. (1995)].

Along with ground-based signatures of the onset precursors, some signatures of E and B variations were measured at 6-8Re in the magnetosphere, in the equatorial plane. Maynard et al. (1996) presented the observation of brief electric field reversals from dawn-dusk to dusk-dawn before the substorm onset. Erickson et al. (2000) observed quasi-electrostatic oscillations with a period of 60-90 sec during the growth phase. Just before the local dipolarization onset CRRES observed one oscillation of E and B fields with quasi-period of 50 sec [Kozelova et al. (2004)].

Most substorm studies do not include detailed analyses of both ground-based and magnetospheric observations. Our case study allows us to make a detailed comparison of



Fig. 9. Frame of the Kilpisjärvi TV record of the vortex-type auroral activation at 2022 UT.

ground-based and space-based observations for the substorm of March 12, 1991.

2.1 Late growth phase

We study the detailed development of the late growth phase and onset structure using all-sky 1-minute images from SOD, MUO, KIL, KEV stations, TV records from Kilpisjärvi and data from the magnetometer network. Five moments may be regarded as important steps:

- a) the pseudobreakups A at 2013-2017 UT and B at 2019:30-2022:30 UT on southward moving auroral arcs,
- b) beginning of weak brightening to the south - 2024 UT,
- c) slow poleward expansion beginning at 2026 UT during substorm onset, T_0 , at 2026 UT, with ,
- d) the second activation onset, T_1 , at 2028 UT, and
- e) the start of the large poleward expansion at 2031 UT.

The first decrease in the X component along the KIL meridian began at 2023 UT at the station Pello (PEL) at latitude $\varphi = 63^\circ$. From the ΔX and ΔZ (not shown) components the differential westward current appeared equatorward of this station and moved poleward. The growth of a weak westward electrojet was observed at the Apatity also at 2023 UT and even at Dixon.

The TV record at Kilpisjärvi shows that at this time the southward moving auroral arc intensified creating a rotating vortex which is shown in Figure 9 at the maximum width moment. Small but definite Pi2 confirm that it was a pseudobreakup (Figure 5).

The electrojet was small until 2026 UT (T_0), when the rate of decrease of the X component abruptly increased. Comparison of the magnetic data shows small poleward activity

Lazutin L. et al.: Case study of multiple-onset substorm of March 12, 1991

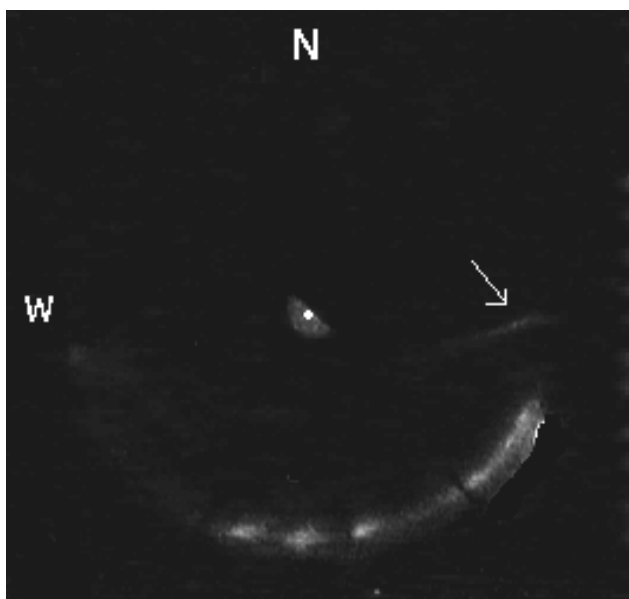


Fig. 10. Substorm onset (T0), Kilpisjärvi all-sky camera, 2026 UT.

expansion terminated between Muonio and Kilpisjärvi. Figure 10 shows that the breakup of the most equatorial auroral arc occurred near the south horizon of Kilpisjärvi at 2026 UT. This breakup was registered also by all-sky cameras at (MUO and SOD. Meanwhile, the KIL TV which was more sensitive, registered poleward of it growth-phase southward auroral arc motion until 2028UT.

The next decrease in the X component started at 2028-2029 UT (T1) again at the station PEL and expanded both poleward to stations MUO and KIL and equatorward to OUL (at $\varphi = 61^\circ$). The TV at KIL shows the second auroral activation (or second auroral breakup) of the KIL zenith arc and poleward expansion.

There are three possible approaches how to consider the 2026 -2028 UT (To-T1) pair of auroral activation onsets.

Onset at To. We may consider To as the onset, and T1 as the second activation. For example, it is well known, that substorm expansion consists of several activations which have many important features similar to the first activation. Moreover, To started at the most equatorial arc and coincided with Pi2 intensification, both signatures belonging to the major onset ones.

Onset at T1. Alternatively, we may assume that To still belongs to the growth phase with the onset at T1. For example, the poleward expansion after To was very small and the real expansion started after T1. Southward arc motion continued after To 2-5 degrees to the North as seen by Kilpisjärvi TV records. The slope of the magnetic bay was smaller after To than after T1. As will be shown below, CRRES started to register gradual increase of B_z only after T1. This may indicate that substorm onset begins in a localized region of the near earth plasmashet when growth phase is not finished.

Onsets at To and T1. Finally, we consider the possibility that we have a double-onset substorm. It is widely recog-

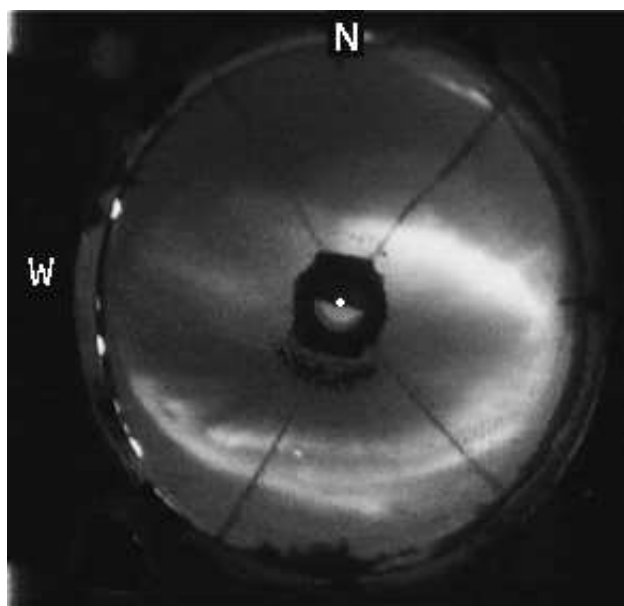


Fig. 11. Two auroral regions where substorm onsets To and T1 began are seen at all-sky camera Muonio, 2029 UT.

nized that the position of the equatorial arc is an important indication that local conditions (plasma pressure gradient, magnetospheric current intensity or sharp change of configuration, etc.) are favorable for the onset instability. But there are cases where two (or a several) auroral arcs were observed during substorm growth phase as in our case. The second arc may indicate that at the end of the growth phase there were two regions in the inner magnetosphere where conditions were close to the critical for the onset instability. (It is necessary to note, that the term "double breakup" was used by Kornilova et al. (1998, 2001) in different meaning, namely when two separated by latitude auroral activations are moving poleward nearly simultaneously, sometimes northward arc activated before the southward one.)

Is there a difference how to name T1 - second activation or breakup onset? Possibly, there is some important physics besides: both the first onset and T1 were prepared before To, while the following activations in a chain are prepared mostly by the previous one. It is clear we cannot choose for sure between these three approaches, even with very good data coverage. These results point to the weakness of the linear single onset substorm scheme.

2.2 T1 Fine structure

The T1 (2028:17 UT) substorm onset or activation which initiated the fast poleward expansion started on the second-from equator auroral arc seen on the Muonio all-sky camera frame in Figure 11. Temporal developments are seen in the keogram (Figure 7), and on several frames of the TV records for the important moments before and after T1 (Figure 12).

Three Figures 10, 11 and 12 illustrate how different might be onset and development of the auroral breakup, au-

Lazutin L. et al.: Case study of multiple-onset substorm of March 12, 1991

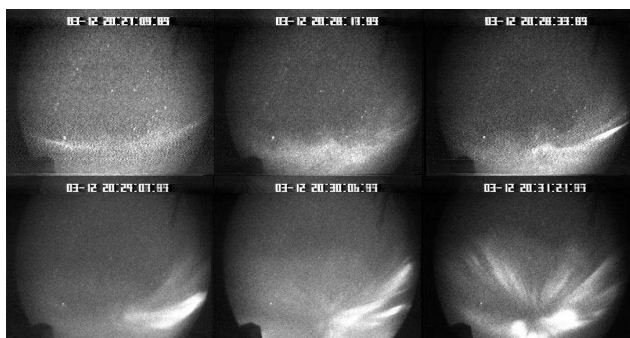


Fig. 12. TV frames of the aurora over Kilpisjärvi during T1 onset and expansion. From the left to the right, upper part: 2027:09 UT, 2028:17 UT, 2028:33 UT, bottom: 2029:07 UT, 2030:06 UT, 2031:21 UT.

roral arc fragmentation, new discrete arcs poleward of the previous and activity development out of some dispersed luminous area.

2.2.1 Auroral arc dispersion

We want to pay particular attention to the pre-T1 activation effect which was not mentioned before, namely the widening or spreading of the very weak and narrow diffuse arc both southward and northward at 2027:47 UT. As a result, the narrow arc became wide and diffuse 30s before T1, when two parallel arc fragments emerged out of the east part of the wide diffuse arc. The equatorial arc became a cradle of the explosive instability. This arc developed with following sequence: 00-15sec - increase of the brightness, 15-25sec - increase of the azimuthal extension toward the west, 33-70sec southward expansion and brightening, 70sec - rays fragmentation began, solid rayed arc across all the sky remains until 80sec.

The poleward expansion started as a fast restricted shift of the diffuse area about 100s after T1, at 2030UT. During the following 3 minutes we observed the corona - two active arcs with rays rotating by preference clockwise. At 2033 UT the equatorial arc faded and the polar one expanded further to the north. One can see from the keogram, that luminosity occupied nearly all of the TV area.

Along with the northward expansion westward expansion takes place. We cannot point out the exact moment when it started, but from magnetometer data we may conclude that WTS structures appeared. Pronounced NS front and at 2046-2048UT, shown on the map in Figure 2, emerged as a local activation near the CRRES footprint. We can assume that the auroral expansion terminated when the first pulsating spots appeared indicating that the aurora was being created by precipitating trapped electrons rather than the freshly accelerated ones. Intensifications of the pulsation brightness coincided with substorm intensifications at 2047UT and 2056UT westward of Kilpisjärvi and were most probably caused by arrival of the energetic electrons drifting from the active region.

2.3 Section Summary

As will be shown below, important signatures in auroral particles are seen at the late growth phase, therefore it is necessary to start summary with growth phase auroral dynamics. Our pseudobreakups (there are large variety of the pseudobreakups) occur on southward moving auroral arcs as vortex formations with counter-clockwise rotation (corresponding to field-aligned current from the ionosphere to magnetosphere) with interval $\Delta t \sim 6$ min in between. Continuation of the CRRES magnetic field stretching (Figure 3) confirms, that gross-scale growth phase continues.

One can see the precursors of the substorm onset: in the ionosphere - the clear onset of the growth of a weak substorm westward electrojet at least from FAR to Apatity ($\Lambda \sim 77^\circ - 113^\circ$) began at 2022 UT (4 min before the T_0) approximately along $\varphi = 63^\circ$. However, we do not find a distinct fading effect in aurora.

At the end of the growth phase at the same longitudinal sector we observe two diffuse arc regions where presumably stability conditions were critical and later two breakups began. The north one started later, activity therefore propagates poleward. The substorm onset was a complicated chain of the events:

- 1) ($T_0 - 2$ min) - increase of weak substorm westward electrojet and appearance of weak most equatorial arc,
- 2) T_0 - brightening of the most equatorial arc with restricted poleward expansion; simultaneously in same longitude sector, southward motion of auroral arc is observed on more high latitudes,
- 3) ($T_0 + 2$ min) - auroral activation in more poleward auroral region near,
- 4) ($T_0 + 4$ min) - final and wide poleward expansion of activity.

In total, after T_0 activations are followed with interval $\Delta t \sim 2$ min, much faster than during growth phase. Was then 2026 UT real beginning of the expansion phase or it stated later, 2028-30 UT, it is difficult to decide assuredly.

Anyway, 2026UT activation was undeveloped, without fast expansion to the North and West. It seems that convective electric field restricted the area of the activity continuing growth phase to the west, east and north of it. At the same time it has all features of the auroral breakup. We found also that two substorms (or large scale intensifications) were observed simultaneously in two different longitudinal sectors (Dixon and Scandinavia) with active phases overlapping in time.

An important feature was auroral arc dispersion accompanying expansion, diffusion forms vent before the associated jump of the active aurora. We found one reference to similar onset feature by Kornilova et al. (2000), but possibly it is more common and important element of the activity expansion, only it usually impossible to register without good resolution.

Lazutin L. et al.: Case study of multiple-onset substorm of March 12, 1991

Table 2. EPAS energy channels

Channel	Energy (keV)	Channel	Energy (keV)
E1	21.5–31.5	P1	37–54
E2	31.5–40	P2	54–69
E3	40–49.5	P3	69–85
E4	49.5–59	P4	85–113
E5	59–69	P5	113–147
E6	69–81	P6	147–193
E7	81–94.5	P7	193–254
E8	94.5–112	P8	254–335
E9	112–129.5	P9	335–447
E10	129.5–151	P10	447–602
E11	151–177.5	P11	602–805
E12	177.5–208	P12	805–3200
E13	208–242.5		
E14	242.5–285		

3 CRRES data

The CRRES spacecraft was launched on 25 July 1990, into a geosynchronous transfer orbit with a perigee of 305 km, an apogee of 35,768 km and an inclination of 18°. The low energy particle data were provided by the low energy plasma analyzer (LEPA) which measured the complete pitch angle distributions of electrons and ions from 0° to 180° every 30 sec with a resolution of 5.625° x 8° in 20 channels in the ranges 100 eV < E < 30 keV for electrons and 10 eV < E < 30 keV for ions [Hardy et al. (1993)]. The medium energy electrons used in this study were provided by the electron proton angular spectrometer (EPAS) which measured electrons in 14 channels in the range 21 keV < E < 285 keV and ions in 12 channels in the range 37 keV < E < 3.2 MeV respectively [Korth et al. (2001)]. The magnetic field data were provided by the AFGL fluxgate magnetometer [Singer et al. (1992)]. Best temporal resolution was used: for particle data down to 1 sec, for magnetic field 2 sec.

At 20–21 UT on March 12, 1991 CRRES was near the equatorial plane at 6.5 Re and 2111–2147 MLT with an estimated magnetic field lines projection between the Scandinavia and Great Britain (Figure 2). The local magnetic field and the EPAS energetic particle measurements for this event are presented in Figure 13. The two arrows in the top panel indicate the onset of the substorm expansion phase, which took place 20° eastward of the CRRES footprint, and the third arrow shows the beginning of the local substorm intensification near the CRRES meridian.

The decrease in the flux of the trapped particles before 2020 UT is a consequence of the CRRES radial motion toward the background boundary of the outer radiation belt and the boundary motion toward the Earth due to the growth phase transition to the tail-like magnetic field configuration.

The emergence and gradual increase in the energetic electrons began immediately after the substorm expansion. In contrast, the energetic ion injection began before the substorm onset during the late growth phase (dashed line) and

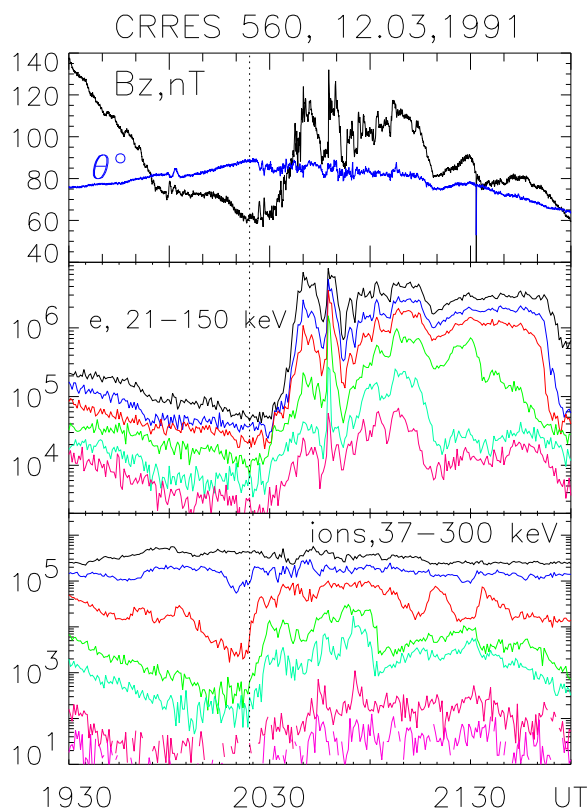


Fig. 13. Magnetic field, electrons and protons differential channels measured by CRRES, orbit 560. Red arrows indicate moments of To, T1 and local activation near CRRES footprint.

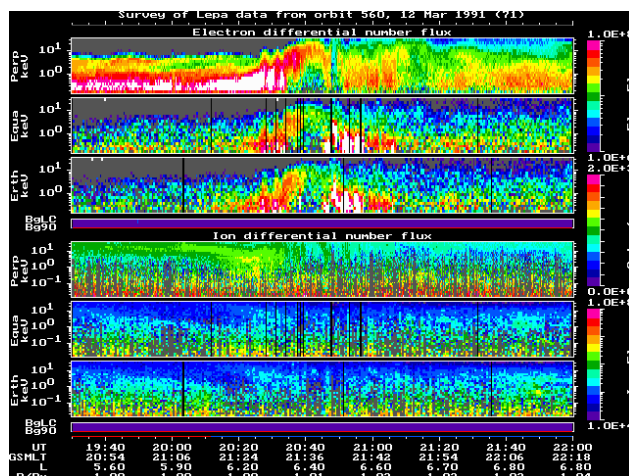


Fig. 14. LEPA particles diagrams during March 12 substorm, 1920–2000 UT. Three upper sectors trapped, field-aligned equatorward and earthward, bottom three sectors show the same for ions.

the intensity increase was completed before the beginning of the electron increase. Besides, the ion-electron injection separation observed also near the local activation at 2047 UT. Separate arrival of enhanced proton flux at the evening

Lazutin L. et al.: Case study of multiple-onset substorm of March 12, 1991

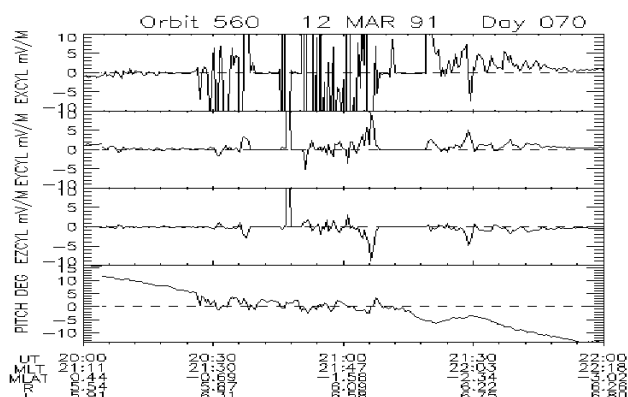


Fig. 15. CRRES electric field measurements, X, Y and Z components, 2000-2200 UT, March 12, 1991.

sector and electrons in the morning is normal for the injections with dispersion away from the acceleration region. In our case good temporal resolution suggest that injections was dispersionless and therefore that the ion and electron injections are separate and different events as was discussed earlier [Lazutin and Kozelova (2004)]. Because this conclusion is not known or recognized by the substorm community, we will pay special attention to this problem.

Summary plots of the low energy particles are presented in Figure 14. One can see considerable response in electron channels and relatively small variations in the ion channels. The electric field measurements are presented in Figure 15. Impulsive enhancements in the electric field were detected in X-component starting from the 2026 UT - substorm onset. Note that CRRES was westward of the onset region. When local intensification onset takes place near the CRRES at 2047UT, E-field increase with an amplitude more than $10 \frac{mV}{m}$ (sensor saturation) was registered in all components. As the electric field measurements are not fast compared with the development of the activation we can regard the E-field data only as an indication that large electric fields were present without details useful for the reconstruction of the E-field geometry and origin.

4 Ions

The region where CRRES was located during the events discussed here may be characterized as an inner edge of the plasmashet and as a nightside quasitrapping region. The importance of the ion population in this region can not be overestimated, because pre-substorm disturbed current configuration is created presumably by the ions, and the substorm onset instability is regarded as a consequence of the growth of ion intensity and anisotropy. Ion current increases and disruption belong to the acknowledged signatures of the substorm scenario.

Although ions (protons) in this region are often regarded as a single population (inner or central plasmashet ions) we prefer to consider separately the low energy (< 30 -40 keV)

and energetic ions, because their temporal behaviour differs notably. There might be possible other divisions. For example, Konradi et al. (1975) suggest division of the substorm injected ions into three parts, above 40 keV, between 2 and 40 keV and below 2 keV.

The energetic ions in turn may be divided onto "old" trapped particles and freshly accelerated substorm-associated ions. The trapped ion flux in the quasitrapping region is decreasing with radial distance while substorm injected ions are dynamic and spatially nonuniform. The existence of the large earthward directed plasma pressure gradient (see, for example, Samson et al. (1992)) led a number of authors to suggest substorm onset scenario in a quasitrapping region.

Observations of the energetic ion changes by the geostationary and the CRRES satellite detectors have been discussed in several case studies [Ohtani et al. (1992); Rasinkangas et al. (1994); Lazutin and Kozelova (2004)]. It was found that the particle (ion and electron) intensity decreased during the growth phase because of the reconfiguration of the magnetosphere and increased rapidly during expansion phase usually with appearance of the additional freshly accelerated (injected) energetic particles. It is accepted that both dropouts and injections are simultaneous for the energetic electrons and ions in the near midnight sector. Statistical investigation of dispersionless substorm injections on geosynchronous orbit by Birn et al. (1997) shows that ions injections are delayed at the morning sector and electrons at the evening one by several minutes. They used data with 72 sec time resolution and events with dispersion up to 2 minute were considered dispersionless. It is difficult to apply results of this and other low resolution studies for the description of the fast changes of the particle and fields during substorm expansion.

The accepted view that electron and ion injections are simultaneous was questioned when resolution better than 1 min was applied. Several case studies reported that ions may increase before the local dipolarization in the evening /pre-midnight sector [Kozelova et al. (1986); Rasinkangas et al. (1994); Lazutin et al. (1998b, 2002)]. The time delay between the ion injection and the dipolarization varied from several minutes to seconds. The energy spectrum of the ion increases suggests a resonant acceleration mechanism because of the essential difference in temporal structure of the different energy fluxes [Lazutin and Kozelova (2004)].

As the number of case studies based on direct measurements of the ion dynamics in this region are small, especially with good time resolution and with necessary coverage of the energy range we hope that our case study will supply some new information.

Figure 16 shows the ion flux from 2020 to 2030 UT, during late growth phase and first minutes of the active phase. Ions were very dynamic during this interval and there were essential difference in temporal features of the different energy channels. Vertical dashed lines indicate four moments of the ion distribution changes: (a) after 2022 UT change of flux in channel P5-P6, (b) at 2024 UT began rather sharp intensity increase in P3-P5, (c) at 2026 UT flux change in P4

Lazutin L. et al.: Case study of multiple-onset substorm of March 12, 1991

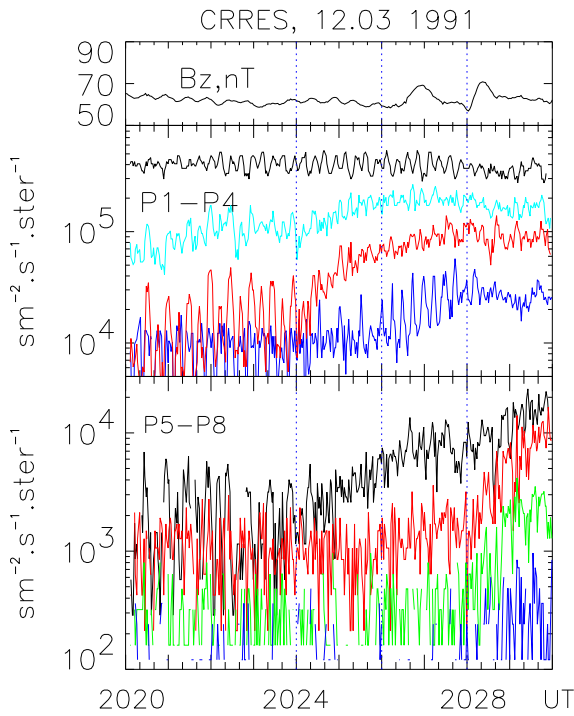


Fig. 16. Magnetic field Bz-component, two low-energy electron channels and eight energetic ion variations during 10 minutes of the late growth phase and substorm onset. Dotted lines show moments of the particle flux transformations described in a text. Regular modulation of the particle flux ($T = 30s$) by satellite rotation indicate to anisotropic PAD.

and new intensity increase in P6-P7, and finally (d) at 2028 UT new intensity increase, in P6-11. It is difficult to foresee such step-like changes of the ion flux with different dynamics in separate energies even in the center of the activation. But we know from the analysis of the ground-based data, that CRRES was outside the onset region and therefore we may suppose that such curious ion behaviour is taking place over the wide longitudinal sector.

4.1 Ion pitch angle distributions

Transformation of the pitch-angle distribution is illustrated in Figure 17 where the PADs of three energy channels are shown for the three time intervals: before 2024 UT (blue signs), after 2025 UT (red) and between these two moments when dramatic change of PAD occurs (green).

Before 2024 UT only the first two channels P1 and P2 have trapped PADs, while higher channels have a decrease near 90° , known as a butterfly distribution. It is typical for the decreasing intensity slope of the outer radiation belt and may be regarded as a temporal effect of the tailward magnetic field line stretching. Then in less than one minute the 90° PA gap

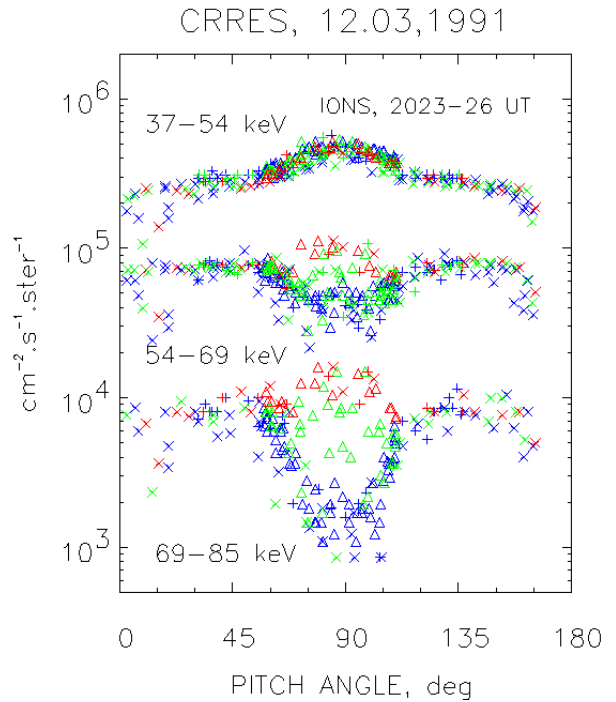


Fig. 17. Pitch-angle distribution of three energy channels of auroral ions for three intervals of the growth phase and substorm onset: before 2024UT (blue signs), after 2025 UT (red) and between these two moments when dramatic change of PAD occurs (green).

was filled and more channels receive pancake or rather head-and-shoulder PAD. The beginning of the "green" interval was chosen when increase of the 90° high energy ($>100keV$) ions started. One can see that particle flux with smaller PA and smaller energy started to increase with delay (some green signs remain on the lower curves). Let us note that no associated changes of the CRRES magnetic field was observed during transition interval therefore ion increase cannot be explained by the change of the trapping region configuration. Later, near to T_o , pancake distributions were observed (not shown) in all the channels except the high energy ones, where statistics doesnot allows to measure PAD. After T_o flat distributions with very small anisotropy (nearly isotropic) were registered for 1-2 minutes.

4.2 Ion spectral distributions

Figure 18 presents an energy spectra of the ions for three moments of the growth - active phase transition where both LEPA and EPAS data are combined. Only 90° particles are presented. Energy spectrum of the ions with PA less than 60° or higher than 120° was similar to the 2028 UT trapped ion spectrum and does not vary with time as one can see from the PAD figures.

Three energy intervals can be found on spectral distribution with different temporal behaviour and presumably different origin. The flux of the low-energy ions with energies below $\sim 2 - 5 keV$ was variable at 2020 - 2028 UT and later

Lazutin L. et al.: Case study of multiple-onset substorm of March 12, 1991

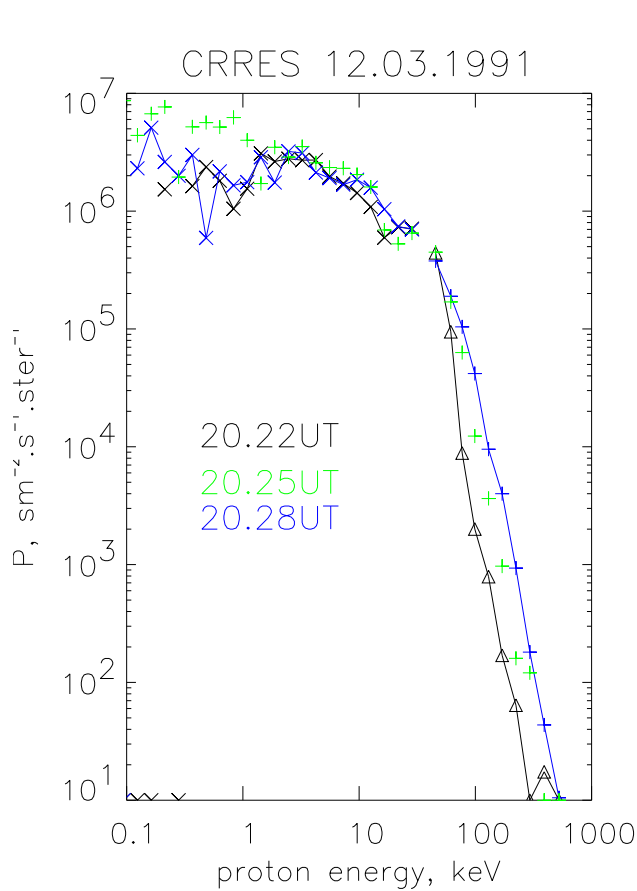


Fig. 18. Auroral ions differential energy spectra of 90 PA for three moments of the late growth phase and substorm onset combined LEPA and EPAS measurements.

until 2100 UT and played an important role in preparation of the local activations. The middle energy ions from 2 - 5 to 20 - 50 keV registered by higher LEPA channels and the first EPAS channel were rather stable during all growth phase and later, during expansion. Possibly this stability can not be interpreted as an absence of the acceleration or other dynamics, but is a product of the spectral shape, which is flat in this interval. For the ions below 30 keV the trapped population was much more intense than field aligned.

The ion flux above 50 keV is highly variable and during growth phase was increasing twice, first around 2024 UT, as shown by PAD figure 17. At 2028 UT one can see new increase of the ions with energy between 100 and 300 keV. Deviation from the smooth spectral shape is seen between 20 and 70 keV which support the idea that presented ion spectrum combines at least two ion populations - low-energy plasmasheet and trapped energetic ions. Quite possible that lowest part of the spectrum from 0.1 to 2 - 5 keV must be considered as a separate one related to (governed by) the ionosphere-magnetosphere interaction.

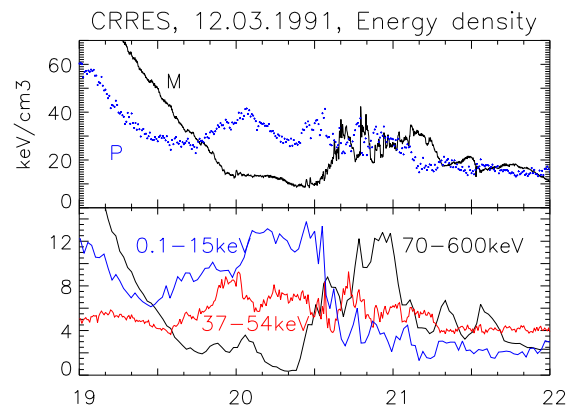


Fig. 19. Magnetic field and total ion (only proton assumed) energy density (upper section) and partial proton energy density for selected energy intervals.

4.3 Magnetic field and particle energy density

The ratio of the magnetic field and particle energy density is an important parameter of the stability of the trapping region. The magnetic field and particle energy density for our event are presented in the upper panel of Figure 19. From 1945 UT to 2005 UT the ion pressure increased and became larger than magnetic field energy pressure. Low and middle energy (< 50 keV) particles are responsible for this effect as illustrated in the bottom panel which shows the input of the energy density by ions for several energy intervals. The decrease of the ion pressure between 2005 UT and 2024 UT was created by high energy ion decrease associated with the PAD dynamics discussed above.

Figure 20 shows extended view of the energy pressure dynamics for the late growth phase and the substorm expansion. After the substorm onset the input of the low-energy ions decreased essentially while energetic ions became primary source of the particle energy density. Along with the freshly accelerated ions the "old" quasitrapped energetic ions are responsible for that increase due to the radial shift of the magnetic drift shells.

At the end of the dipolarization, magnetic energy density became larger than the ion energy density, but before the local activation relation again became reversal.

The vertical dashed lines indicate T0, the beginning of the expansion and of the local activation at 2047-49 UT. If we extract the slow changes of the ion intensity discussed above, one can see density increases before all three moments both on low energy and high energy curves. The middle-energy ions remain unaffected. After onset moments, the low energy part of particle energy density decreases. More fast and large drop of the energy density observed after the local substorm activation at 2047 UT when CRRES was close to the activity center. Just in this time the energy density drop was recorded also in higher energy part.

One finds from Figure 20 that there was one more moment when ion intensity dropped after the previous increase,

Lazutin L. et al.: Case study of multiple-onset substorm of March 12, 1991

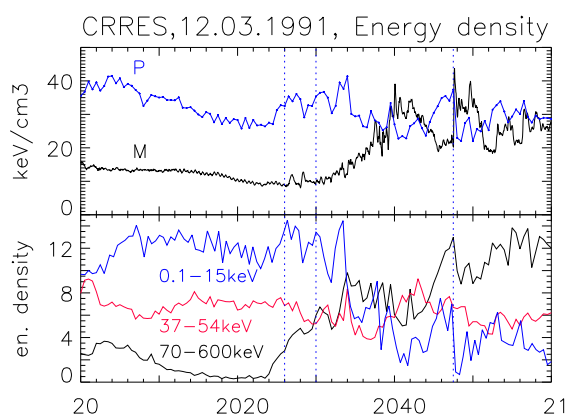


Fig. 20. The same, expanded plots for 2000-2100 UT interval.

namely just before 2034 UT. We returned to auroral TV record and found that indeed there was auroral activation at that moment. Also the Sodankila all-sky data shows some luminosity increase on the south-west at 2034-2035 UT.

4.4 Summary

1. Our data show that in the evening/pre-midnight sector of the magnetosphere at ~ 6.3 Re the electrons in general closely respond to the change of the magnetic field and injections are correlated with dipolarizations while protons arrived before the dipolarization and often are in anticorrelation with electrons. Similar signatures of the injections were observed at the geostationary satellites GEOS-2 and CRRES at ~ 6.6 Re in same sector and described by [Kremser et al. (1982); Rasinkangas et al. (1994); Friedel et al. (1994); Kozelova et al. (1996); Lazutin et al. (1998a)].

Besides our analysis shows that the ion flux and ion energy density increase (decrease) before (after) the substorm onset was observed when CRRES was 20° westward from the onset site. Same, but more fast and large, changes were observed before and after the local activation when CRRES was near (within) the localized active region. Ions with energies from several keV to hundreds keV are involved in such variations with middle energy ions (15 - 50 keV) less active than high and low energy ones. Cited above papers based on CRRES data confirm this conclusion, also Lyons et al. (2003) from Geotail data on $r \sim 10 - 13$ Re found particle pressure decrease during substorm.

2. The leading front of the ion injection before T_0 have several peculiarities:
 - a) - the ion flux increased in restricted pitch angles around 90° with step-like rise of the involved energies over considerably extended region (50 - 450 keV)

- b) -Transformation of the pitch-angle distribution have following sequence: butterfly \Rightarrow head- and-shoulders \Rightarrow pancake \Rightarrow isotropic \Rightarrow pancake.
- c) - filling the butterfly gap in 50 - 200 keV range vent nearly without dispersion.

3. Careful analysis of the optical and magnetic data allow us to claim that fresh ions at 2024 UT do not arrive from the substorm which took place somewhere away (eastward) from the observer. We are sure that there were no breakups earlier than 2026 UT. Besides, comparison of the moments of the ion distribution changes in the magnetosphere described above with moments of auroral and magnetic activity outlined in 1.1 shows that every aspect of the discussed changes in ion fluxes or PAD at $r \sim 6.3$ Re coincide with some elements of the auroral activity. It might be also very important that rather sharp increase of the trapped energetic ion flux 2 minutes before the T_0 coincides with faint auroral luminosity increase at the south part of the sky where breakup initiates later.

5 Electrons

Starting from the first years of direct particle measurements there were introduced several divisions and subdivisions of the electron population in the quasitrapping region. We divide the electron populations into low energy (< 10 keV) and energetic parts, similarly as was done for the ions. The low energy electrons are usually referred to as plasma sheet electrons. They have addition of transient fluxes of low-energy auroral electrons (LAE) accelerated during substorms. Energetic electron populations consists of radiation belt electrons also enriched during substorms by transient energetic auroral electrons (EAE) associated with substorm injections.

Although components are related to each other and mixed during substorm development, it is helpful to have this division in mind. Also it is worth to repeating that the auroral electrons, both low and energetic ones, are registered in a transition region between dipole and taillike magnetic field lines. This region, named previously as a "night casp" or "auroral magnetosphere" [Lazutin (1986)], is located inside the quasitrapping region.

The low energy electrons measured by LEPA are presented in Figure 21. The solid and dashed lines in the figure corresponds to the trapped and field-aligned electron intensities. Electrons with energy below ~ 5 keV and between 5 and 15 keV behave differently during this period. The low energy electrons have trapped PADs before the expansion and are isotropic afterward with bursts of field-aligned fluxes around local activation time. The significant intensity decrease was similar to the decrease of low energy ion flux at that time. The 7-15 keV electrons undertake transition to butterfly distribution between 2015 to 2024 UT and fast return to the trapped distribution at 2024 UT. (Let us remind that similar transformations were recorded for energetic ions. What

Lazutin L. et al.: Case study of multiple-onset substorm of March 12, 1991

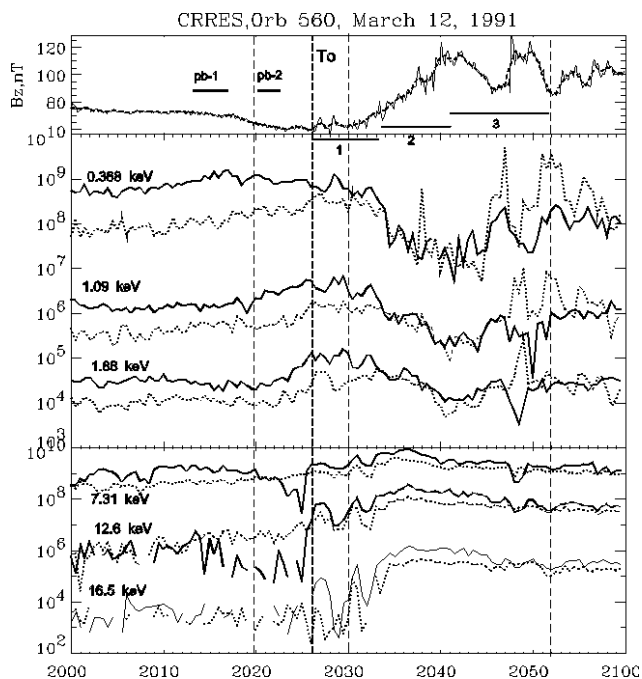


Fig. 21. Magnetic field B_z and low energy LEPA electron measurements, 2000-2100 UT. Solid lines - trapped electrons, dotted lines - field-aligned electrons.

common are between low energy electrons and 50-200 keV protons?).

The energetic electron temporal profiles measured by the CRRES EPAS detectors were shown in Figure 13. In the quasi-trapping region before the substorm only radiation belt electrons are present and after the substorm onset energetic auroral electrons (EAE) appear. We will study this increase of the electron flux known as the injection event in detail, but before that we will summarize main EAE features.

Energetic auroral electrons were identified and studied by balloon-born X-ray detectors [Kremser (1970); Lazutin (1986)]. Later EAE dynamics on the equatorial plane were studied by geostationary and other satellites which spent more time in the auroral magnetosphere than typical duration of the substorm development. It is known that during growth phase energetic electron intensity in the quasitrapping region decreases due to the magnetic field taillike stretching and possibly to adiabatic deceleration and that on the substorm onset intensity increase associated with EAE occurs known as an injection event. In total, electron dynamics is more regular compared to the ions and the relation to the magnetic field variation as can be seen in Figure 13.

Both magnetic field and energetic electron variations registered by geostationary or CRRES satellites depend on the space-time scale of activity region and the satellite position relative to this region. In our case study CRRES was located in vicinity of active region then the dependent was mainly from a scale. For the substorm expansion phase the activity has large scale (7-15 minute duration, $\sim 15\text{-}30^\circ$ longitude sector) where all variations, magnetic field dipolarization,

and electron enhancement are gradual. When the satellite is close to the localized more small scale activation region, which is of several degrees wide and 1-2 minute duration, then both the magnetic field and electron increases may be short and very fast.

Because the substorm expansion consists of several activations, usually CRRES encounters at least one of such localized events. It was the same in substorm observation under discussion and we have opportunity to discuss auroral electron acceleration in details, both mechanisms and sources as well.

As for the source of the EAE there are two electron populations always present here - outer radiation belt and central plasmasheet electrons enriched by freshly accelerated LAE. Radiation belt intensity at the outer decreasing slope which is usual position of the onset region is rather small to be a main source of the injection, although they may be involved into associated variations. Freshly accelerated LAE near the inner edge of the plasmasheet may be a general source of EAE during substorm. The CRRES observations provide the opportunity for detailed investigation of the low and high energy electron related dynamics and electron acceleration.

5.1 Auroral electron injection

The upper panel of Figure 22 shows an extended view of the magnetic field transformation, which can be described as several dipolarizations with different increments and durations (green, blue and red lines); shorter dipolarizations are inserted into a longer one. The energetic electron intensity displays similar direct trends. Fast increases (blue lines) occur when the localized activation was close to the satellite while the gradual trends (green and red lines) are the result of the integrated large scale dipolarization of the substorm expansion phase. Fast and gradual, localize and large scale electron increases are the two main constituents of the electron dynamics during this substorm. Therefore it is interesting to examine these processes in further detail. (As shown above ions are not magnetized their relation to the magnetic field is different, although the longer trends are present in the ion variations as one can see at the figure.)

At first we will examine gradual increase, trend "green lines", which may be regarded as a typical "injection event". The gradual energetic electron acceleration observed between 2030 and 2040 UT was closely correlated with the increase of the magnetic field B_z component as can be seen by comparing the bottom and upper panels in Figure 22.

The temporal evolution of the electron spectra in medium and low energy regions observed between 2030 and 2040 UT are shown in Figure 23 and Figure 24 respectively. The UT times of the recording of the five spectra are shown in the inset panel in Figure 23. In the beginning of this interval two particle populations are present: "old" trapped radiation belt particles and plasmasheet electrons with a typical for CPS 1-3 keV average energy [Weiss et al. (1992)]. Total distribution has quasi-Maxwellian type with a power law high energy tail. Initial spectrum presented on Figure 24 has a maxi-

Lazutin L. et al.: Case study of multiple-onset substorm of March 12, 1991

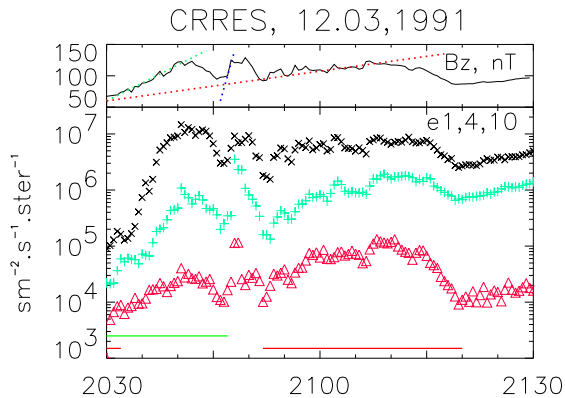


Fig. 22. Magnetic field and electron intensity temporal trends.

mum at ~ 0.4 keV and a power law spectrum ($N = E^{-k}$) with $k \sim 1$ from 1 to 7 keV and $k \sim 9$ between 7 and 15 keV. The higher energy range was occupied by the "old" radiation belt electrons with $k \sim 0.6$. After 6-10 minutes the third population emerges: energetic auroral electrons. The progressive energization of the plasmasheet electrons can be seen in Figure 24 and the resulting increase and softening of the energetic electron spectrum can be seen in Figure 23. The two dotted lines in Figure 24 show the high energy extension of the electron spectrum at the beginning and at the end of the acceleration interval. This figure shows that the LEPA and EPAS measurements are in good correspondence in their region of overlap. This electron enhancement (or injection) presents a clear example of the transition of plasmasheet electrons to the different class of the population, EAE.

Such well known process as a betatron acceleration can be regarded as the explanation. In adiabatic region the perpendicular component of individual particle energy changes proportional to the change of the magnetic field intensity from the starting to the final point of particle trajectory, $\frac{W_1}{W_2} = \frac{B_1}{B_2}$. From 2032 to 2037 UT the characteristic energy of electron distribution increased by factor of 2 (Figure 24) while B_z at the CRRES position changed approximately from 65 to 110 nT. To receive necessary $\frac{B_1}{B_2}$ ratio one can take into account the existence of the cross-tail electric field and electron $E \times B$ drift from 55 nT level, which is about 0.5 Re tailward from the CRRES. Therefore in "injection" events electrons are indeed injected but from short distance and the local betatron acceleration plays a general role.

5.2 Low and high energy electrons during the local substorm activation

One of the substorm intensifications took place near the CRRES longitudes and can be studied in further detail. This intensification occurred at 2045-2049 UT and has most of substorm onset signatures, such as a H-component magnetic bay in several stations, magnetic field dipolarization in the magnetosphere and auroral particle enhancement registered

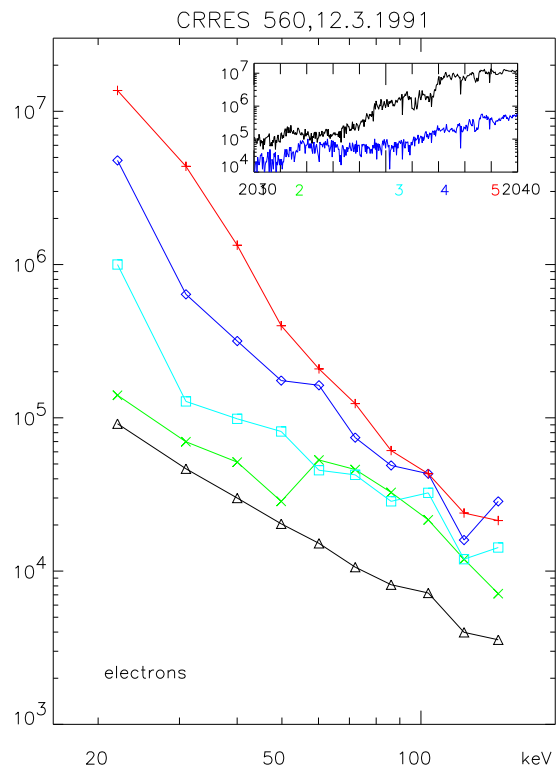


Fig. 23. Energetic electron (EPAS) spectrum transformation during gradual dipolarization. The moments of the spectrum measurements are indicated in the inserted box.

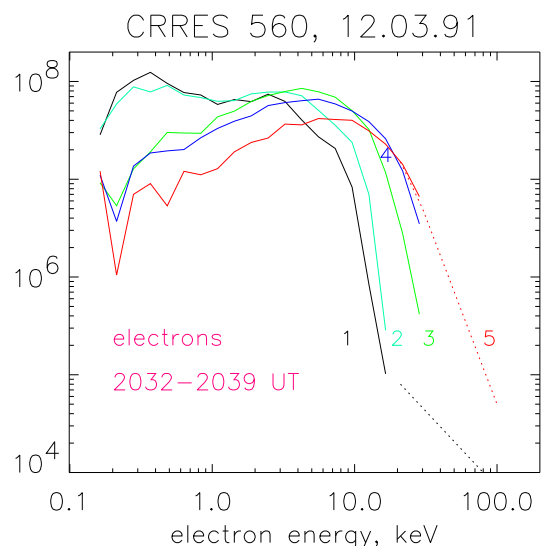


Fig. 24. Low-energy electron (LEPA) spectrum transformation for the same moments as on Figure 23. Dotted lines show spectrum extension to high energy range from EPAS data.

Lazutin L. et al.: Case study of multiple-onset substorm of March 12, 1991

by the CRRES detectors. After 2045 UT the weak N-S type auroral forms appeared above Scandinavia and the upward FAC was located near or eastward of NOR ($\Lambda \sim 108^\circ$). After 2048 UT the typical current picture associated with the leading edge of the SCW appears over the meridian FAR (80°) with CRRES ($\sim 100^\circ$) inside the active region.

After the HD crossing (the interval 2 on Figure 21) the CRRES encountered the large scale region 2 FACs flowing from the ionosphere (see Figure 6). The CRRES was located in this region, when the intensification occurs near the CRRES meridian. The dispersionless injection of electrons 21-150 keV and fast local dipolarization (trend b on Figure 22), which the CRRES observed in this time, were usual features of a local intensification. Let us start with low energy electrons dynamics. Electron pitch-angle distributions before and during the onset of the intensification are shown in Figure 25. Some of the PADs display symmetric up-going and down-going field-aligned electrons so that the summary FAC will be close to zero. Other distributions show asymmetric electron PADs and may be regarded as an indication of the field aligned current development. From Figure 21 and 25 one can see that near the moment of dipolarization the behaviour of the electrons is different in the 0.1 - 1 keV, 1 - 5 keV and 20 - 100 keV ranges. We stress one important fact: low energy 0.368 keV field aligned electron flux was registered from 2045:20 - 2047:00 UT at the end of the magnetic field lines stretching and again after interruption at stretching interval 2048:45-2049 UT (see also Figure 21). Exactly during this interruption a high-energy electron burst and a magnetic field dipolarization were registered with the preferential perpendicular acceleration of the electrons in the 50 - 100 keV energy range. Simultaneously, the sudden increase of 1 - 3 keV field aligned electron flux, was observed.

Thus, low energy 0.368 keV field aligned electron flux increases before fast local dipolarization and drops sharply after one. This drop coincides with the sudden increase of 1 - 3 keV field aligned electron flux and the dispersionless higher energy 50 - 100 keV electron injection. Complicated low energy electron behaviour was mentioned by Arnoldy, Moore, 1983; Klumpar et al. (1988); Kremser et al. (1988); Lui et al. (1992). But we did not find the description of a fine structure in the behaviour of the low energy electrons and relation with higher energy electrons before and after the fast local dipolarization described above.

The energetic auroral electron energy spectrum transformation (Figure 26) during the substorm local intensification differs from the gradual adiabatic acceleration. One can see the preferential acceleration of the electrons with $PA \sim 90^\circ$ in 50 - 100 keV energy ranges. The increase of these electron flux was very fast, ~ 10 sec, and accompanied by large $\frac{\delta B}{\delta t} \sim 7 \frac{nT}{s}$, which is indicative of induced E-field acceleration.

5.3 Summary

We considered details of the electron behaviour during two different types of magnetic field dipolarization, namely grad-

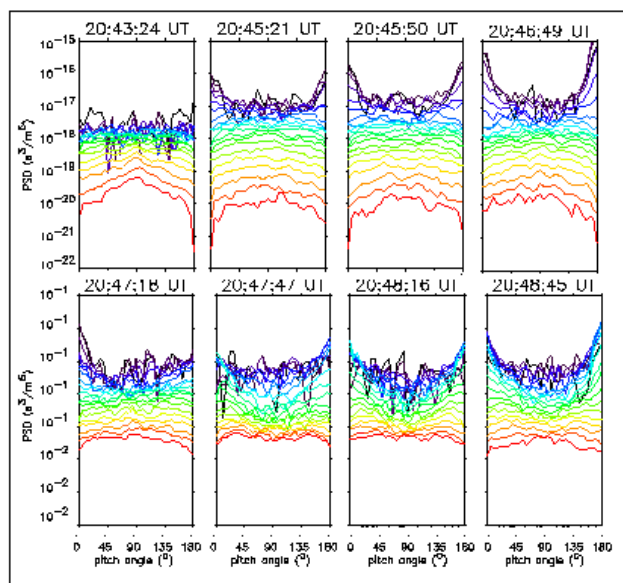


Fig. 25. Auroral electron pitch-angle distributions during the onset of CRRES local intensification. Upper seven lines (black and blue) correspond to 0.16 - 1 keV and bottom three (red) lines to 16 - 30 keV electrons.

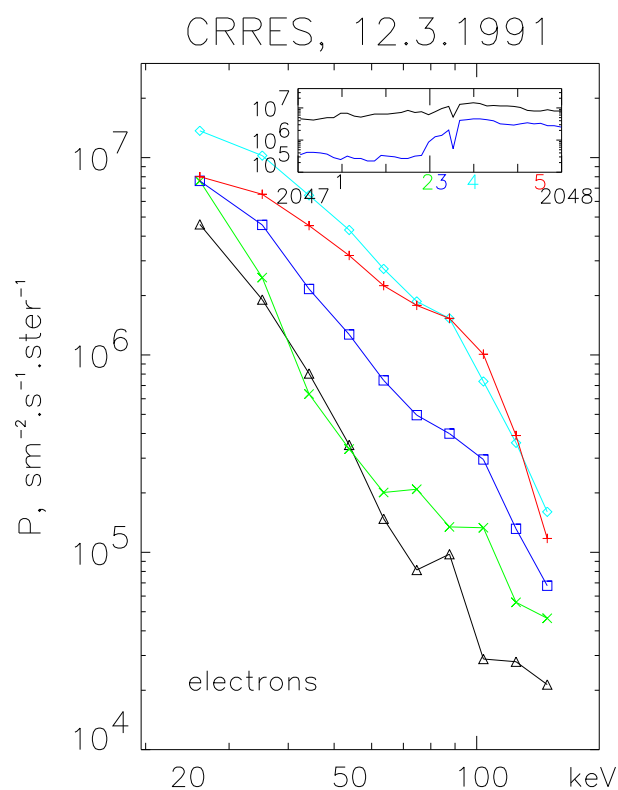


Fig. 26. The same as for Figure 23 for the 2040-47 UT electron acceleration during local activation.

ual dipolarization and fast impulsive one. During the gradual

Lazutin L. et al.: Case study of multiple-onset substorm of March 12, 1991

(7 - 15 min) substorm magnetic field dipolarization typical "injection" event was registered which our study allows to regard as transformation of the central plasmasheet 0.1 - 10 keV electrons into 10 - 100 keV auroral electrons. The accelerated electron spectrum preserves its quasi-exponential shape but the characteristic energy increased. The process of the betatron acceleration represents the main part of the electron injection event in this case. During the sharp magnetic field dipolarization (10 - 20 sec) low energy (< 3 keV) electrons are varying quickly with clear indication of field-aligned acceleration while energetic (21-150 keV) electron perpendicular flux increase most suggests induce acceleration as a most probable source. We find a fine structure in the behaviour of the lower < 3 keV energy electrons with $PA \sim \leq 30^\circ$ near this dipolarization moment: lower energy < 1 keV electron flux increase before this moment and sharp drop after local dipolarization moment. This drop coincides with the sudden increase of 1-3 keV field aligned electron flux and the dispersionless higher energy 50 - 100 keV electron injection.

6 Discussion

6.1 Substorm

Following are the most important features of the 12.03.91 substorm found from ground-based observations:

- 1 - simultaneous or overlapping development of two substorms or substorm intensifications in different longitude sectors is possible.
- 2 - within the same longitude sector near substorm onset poleward evolution of the activation region is observed simultaneously with growth-type southward motion of auroral arc on more high latitude .
- 3 - the chain of activations was observed on the late growth phase with increasing intensity and with decreasing intervals between activations Δt (from 6 to 2 minutes) toward the T_0 .

It difficult to accord this features with the simple isolated substorm model. The substorm model which describes a substorm as a temporal sequence of three phases - growth, active (expansion) and recovery following each other was introduced by S.-I. Akasofu and played an important role in magnetosphere study. It still may be applied to some simple substorm observations from a single station or for global auroral oval records such as obtained by Polar satellite where details are smoothed and resolution is low. But more often substorm activity is partly totally disagree with three phase scheme. Attempts to improve defects of this scheme by introduction of the multiple onset substorms [Rostoker et al. (1980)] is a step in the right direction, and discussion on the loading-unloading relation is the second step [Akasofu (1968); Rostoker et al. (1986)]. As a next step we propose following

approach. Let us consider substorm activity as a superposition of global and local processes (Figure 27) depending on the inner and outer conditions. The growth phase (which is mainly loading) is a global (or more correctly large-scale) process controlled by the solar wind electric field. Recovery is a partially global, partially local process when the magnetosphere returns to the quiet configuration and get rid of the particle superabundance. The global recovery began after the end of the global loading, when the IMF Bz finally reversed to the northward direction. Simultaneously with the global (large-scale) processes several types of localized unloading activity are observed. Undeveloped activations, pseudobreakups and real onsets with following chain of expanding activations are examples of such localized events. Within this approach it is understandable why growth phase may continue in some region while activations are in progress in another one. Substorm usually develops in longitudinal sector two-three hours wide, and in other sectors may continue growth phase and even take place another independent substorm.

Localized activations are similar in definite respects, usually all are impulsive, with certain explosive instability behind each. For example, considerable efforts were spent to find the difference between real breakup and pseudobreakup with the result that there is no difference except the size of the following expansion. But along with similarities, there are also differences between the undeveloped and real activations, spontaneous and triggered ones. For example how they start and obviously why they start, the types of the instability behind might be different. Some of the activations are not strong enough to change situation, other are more important for the conditions in the surrounding sector. The measure of the importance is the volume of the expansion and/or the level of dipolarization. Chain or sequence of the localized activations create large-scale unloading structures such as auroral bulge or westward travelling surge.

In our case we observe at first during late growth phase weak activations followed by more strong ones at T_0 and T_1 and fast expansion. It is a known fact that before the sharp start of the magnetic bay some slow negative deviation (i.e. increase of the electrojet) is often observed. Many authors described pre-expansion activity. For example Voronkov et al. (2002), divided substorm onset into slow and fast parts. Why slow part is important for the substorm development? Our analysis suggests that the most important process during this pre-expansion activity is the acceleration and accumulation of energetic ions. Electrons may be accelerated during pseudobreakup or other pre-expansion activations as well, but they are not significant for the coming expansion, whereas increase of ions flux and ion energy density is most important for the preparation of the onset instability or instabilities.

What prevents initial small activations from consequent expanding? Two reasons are evident : not enough energy was loaded into inner magnetosphere, conditions in the surrounding area are far from the critical ones. Solar wind electric field which is still large at the growth phase may suppress

Lazutin L. et al.: Case study of multiple-onset substorm of March 12, 1991

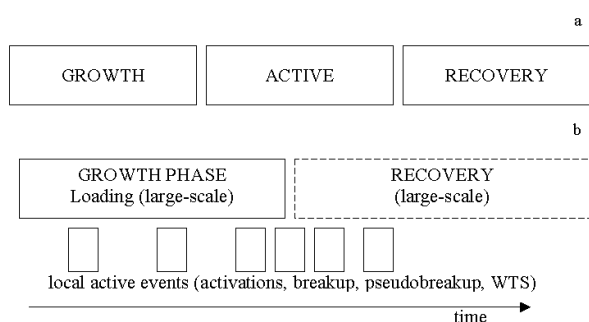


Fig. 27. Scheme of substorm phases relation.

expansion.

During expansion phase critical conditions are prepared rapidly at the expanding area by earlier activations. During the growth phase conditions for the first onset instability are created usually near the most equatorial arc. But it is possible that the second activation is also prepared during the large scale growth phase. Indeed, from our case follows that two auroral arcs were prepared during the late growth phase as a predestinated place for the substorm onset instability and as a result we observe the double onset described above. The first activation begins in the most equatorial arc and second at the next poleward one.

At present onset activation To attracts most attention in a substorm studies and models as a breaking point of the substorm development. Can we say that T1 or growth phase activations are less important for the understanding of the substorm physics? Certainly, no. It is time to administer more attention to individual activations, their fine structure, both optical effects and auroral particle dynamics in conjugated quasitrapping region.

Comparison of different auroral substorm case studies shows that each carefully inspected substorm activity and each auroral activation has an individual way of the development. Quite possible, that such variability, when the common law escapes from observers, is a result of the presence of some invisible agent, which is more important than position of the old arc or arrival of the new active auroral forms. As such possible agent we suspect auroral protons (ions) with energies of ten to hundred keV.

6.2 Particles

Electrons and ions play different roles in substorm development. Ions are important for the dynamics of the magnetosphere configuration as current carriers and as a source of pressure anisotropy. The energy density of the ions may exceed that of the magnetic field which brings closer the instability onset. Electrons are not important for the magnetosphere dynamics, but accelerated auroral electrons create most of the substorm spectacular effects: aurora, ionospheric absorption and electrojet, auroral X-rays, outer radiation belt refreshing etc. From this difference it is not surpris-

ing that auroral ion and electron injections are two different processes. Previously accepted conception of the mutual injection was based on the erroneous assumption of joint particle injection from the magnetotail. Our case study shows that both energetic electrons and ions are accelerated in-situ, by different mechanisms and during different time intervals.

6.3 Ions

Ion behaviour during substorms is not known as well as for the electrons. One reason is the complicated character of the energy spectrum dynamics. Neighbouring energy channels show different temporal behaviour, as observed in our case study. Another reason is poor information on the proton aurora.

Well studied active aurora during substorm expansion is a reflection of the auroral electron activity. The proton aurora is usually not intense enough to record with good time resolution and to separate from the background of the strong nearby electron spectral lines. Moreover, when observations with minute resolution are available, they show that proton aurora weakens at the substorm onset.

Our data show that main features of ion dynamics in the evening sector of the magnetosphere on ~ 6.3 Re in association with substorm 12.03.04 are summarized as follows:

- 1 Ion injection was observed before the dipolarization and electron injection. Similar signatures of the injections were observed at the geostationary satellites GEOS-2 and CRRES at ~ 6.6 Re and described by Kremser et al. (1982); Kozelova et al. (1986); Rasinkangas et al. (1994); Lazutin et al. (1998b, 2002).
- 2 Ions are accelerated in several steps in restricted energy range and restricted pitch angles around 90° . Moments of the ion distribution changes in the magnetosphere coincide with changes of the auroral activity.
- 3 The most fast increase of the perpendicular ion flux with transformation of the PAD from butterfly to isotropic type was observed two minutes before ?? and coincides with beginning of weak auroral luminosity at the following breakup area. Filling the butterfly gap in 50 - 200 keV range occurs nearly without dispersion.
- 4 Two ion populations are predominantly participating in substorm activity: low energy (< 15 keV) and energetic (> 50 keV).
- 5 Ion energy density increase (decrease) before (after) the substorm activation onset. More fast and large drop of the energy density observed after the local substorm activation near the activity center. Just in this time the energy density drop was recorded both in low and in higher energy parts).

More observations are needed for the definite conclusion on the ion acceleration mechanism. We can guess that some

Lazutin L. et al.: Case study of multiple-onset substorm of March 12, 1991

part of energetic acceleration might be of the resonant origin, when only certain group of particles may be accelerated by associated turbulence. Curls or spirals of the aurora as well as the magnetic pulsations observed during the late growth phase indicate on the development of turbulence. Observed on figure 10 azimuthally periodic auroral vortices are regarded as the first step of the substorm onset instability before the substorm expansion [Elphinstone et al. (1996); Maynard et al. (1996); Roux et al. (1991); Voronkov et al. (1999)]. Besides, Perraut et al. (1998) have shown that on Geos-2 the intense high frequency waves ($f > f_{H+}$) with periods of ~ 1 second develop at, and only at, dispersionless energetic ion injection and that their energy is strongly related with the flux and the thermal anisotropy of these protons. From observed characteristics these waves are mode resulted from the coupling between shear Alfvén mode and the slow magnetosonic mode in a finite β plasma.

Other cause of the particle increase may be entrance of the satellite into layer of the enhanced particle population; with single point measurements there is scope for considerable speculation.

Summarized influence of the ion fluxes to substorm activity can be followed by energy density plots on Figures 19 and 20. While CRRES depart from the Earth, energy input of the trapped energetic ions decreases. Low energy ions became most important after 1930 UT when CRRES enters into inner plasma sheet. Possibly remnants of the previous activity were responsible for the fact that the energy density of the ions was larger than that of the magnetic field. Next new increase of particle energy density started at 2024 UT. Energetic ions play a major role, with input increasing from 0.5 to 9 $\frac{\text{keV}}{\text{cm}^3}$. The low energy ion input also increased but with smaller rate.

Ion density increase before the activations and decrease afterward was registered again on 2034 and 2047 UT activations with essential input both of the low energy and energetic components. There are no doubts that this effect is very important for the understanding of the preparation and start of substorm activations. The enhancement of current in the near-Earth region before T_0 is associated with these plasma pressure increase that may create unstable conditions before the substorm onset. For example, one of proposed mechanisms for current discuspion is the ballooning instability [Roux et al. (1991); Korth et al. (1991)]. The condition for its onset is $\frac{L_p}{R_c} < \beta < \frac{2L_p}{R_c}$ (L_p - plasma pressure radial gradient length scale). This condition is fulfilled near-geosynchronous distances [Korth et al. (1991)] but at 8.8 Re possibly not [Lui et al. (1992)]. Ion energy density increase before the current disruption was observed in one example at $r = 8.8$ Re [Lui et al. (1992)]. Lyons et al. (2003) come to the conclusion that a reduction in equatorial pressure is general feature of substorm expansion phase at Geotail at $r \sim 10 - 13$ Re, but concluded that however, how this reduction occurs presents a puzzle. They supposed that pressure reduction may be associated with creation of the substorm current wedge and is initiated by a reduction in the strength of large scale convection.

It is very important to clarify auroral ion dynamics because this population control magnetospheric currents, both field aligned created by the plasma pressure gradients and azimuthal as a main current carriers. Observed in our case evolution of the ion PAD near T_0 agrees with decrease of the current in the magnetosphere. Indeed in stationary plasma the total current j is given by

$$j_{\perp} = c \left(\frac{B \nabla p_{\perp}}{B^2} + \frac{(p_{\parallel} - p_{\perp})}{B^2} [B(b \nabla) b] \right) \quad (1)$$

Here the second term is associated with the pressure anisotropy and the radius of field line curvature. During the interval under discussion, 2020-2024 UT, change from $P_{\parallel} > P_{\perp}$ to $P_{\parallel} = P_{\perp}$ took place and then the current decrease will be resulting, if the change of first term was not strong enough to produce an opposite effect. In summary, 2-3 minutes before T_0 , we can see: in the ionosphere - the slow growth of a weak substorm westward electrojet and auroral activity approximately along $\varphi = 63^{\circ}$ and in the magnetosphere - the current decrease (or appearance of eastward differential perturbation current) on $r \sim 6.3$ Re. Therefore it is possible to assume that equivalent current system of pre-onset perturbation has SCW type form. Therefore, the evolution of the proton PADs in the interval may be consistent with the current decrease.

Another important point to which is necessary to draw attention is that the middle energy ions remain rather stable, passive at the transition growth-onset interval. In fact it is protons or ions above 50 keV or even higher which are actively involved in the process. The difference in the dynamics of the ions of the middle and high energies is possibly a consequence of coexistence of two regimes of particle motion: adiabatic and nonadiabatic. The deviation from adiabaticity is possible because of the low ratio between the field line curvature radius and ion gyroradius [Büchner and Zelenyi (1989)], and when the acceleration region is small and comparable with ion gyroradius. The second reason is more important in quasitrapping region where magnetic field lines are not significantly extended tailward.

Excess of particle over magnetic field energy density which creates unstable conditions before the substorm onset is a result of the increase of high energy ion flux. This means that it is not the plasmashet which is playing main role in onset but, rather, the energetic quasitrapped ions. Therefore MHD approach to the onset and expansion processes is not justified, and the models based on MHD are too simple for a full description.

The concept of the plasma sheet as a single formation from the magnetotail to the inner edge deep in the quasitrapping region needs reexamination. Fast changes of the low-energy ion flux before and after activation can not be related to the processes in the magnetotail. Different energy spectra, pitch angle distributions in a different magnetic field envelope suggest that central plasma sheet and outer plasmashet are different objects. During the growth phase there is relation, certain energy transfer from the magnetotail manifesting by southward moving auroral arcs but during late growth and

Lazutin L. et al.: Case study of multiple-onset substorm of March 12, 1991

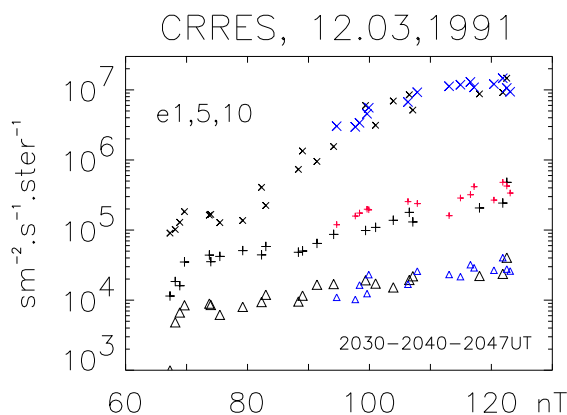


Fig. 28. Electron variations versus magnetic field, short trend 2032-2042 UT.

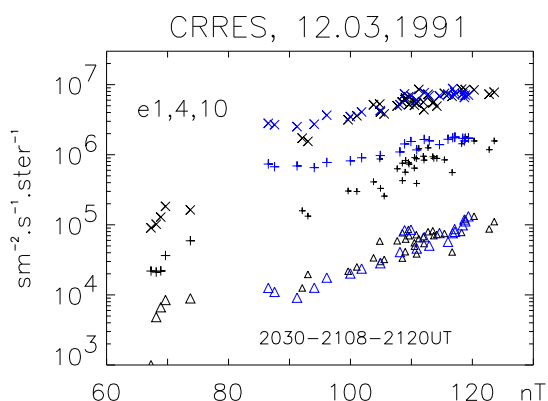


Fig. 29. The same as Figure 23 for the long trend

active phase particle dynamics in the quasitrapping region has independent character.

6.4 Electrons

The CRRES observations demonstrate that a transition region between dipole and tail-like magnetic field lines (or the quasitrapping region) on near geostationary distances is very dynamical structure: electron fluxes and magnetic field exhibit very significant variability at various time scales. This may mean the complex of the acceleration mechanisms during magnetospheric substorm.

The gradual electron flux and magnetic field changes. There are two intervals of magnetic field decrease after the previous increase as shown by the Figure 22, the first after 2030-2040 UT trend and the second after the long trend 2030-2110 UT. Here we can examine the effect of intensity recovery and relative importance of these two processes. Figure 28 shows the electron intensity versus B_z for the short trend, black and red signs corresponds to the increasing and decreasing magnetic field intervals and Figure 29 the same for the long trend. Although the electron intensity is decreasing

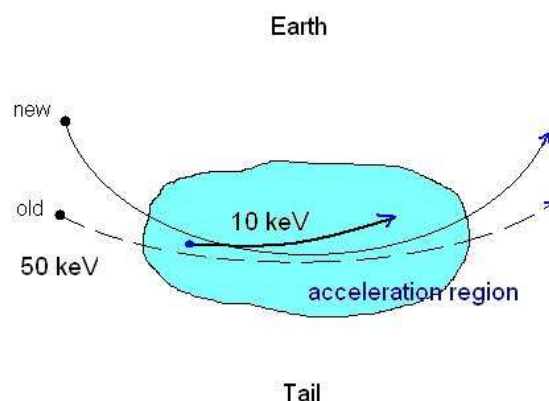


Fig. 30. Sketch of electron dynamics during the "injection" event.

ing in all energy channels with B_z decrease, the positive acceleration effect is obvious for the long trend at the energies up to 90 keV. In high energies total recovery was registered, suggesting that drift shell radial displacement is the main effect for high energy electrons. For the short trend at 2030-2040 UT the effect was the same - high energy intensity plots has no hysteresis while low energy ones reveal net intensity increase after deceleration, although not as large as during the long trend.

The azimuthal dimension of the region where dipolarization is taking place and total duration of the dipolarization impose the upper energy limit for the accelerated particles. Figure 30 shows a scheme of the particle drift during the dipolarization, shaded region is a substorm active sector. Low energy electrons will spend all time inside the acceleration region while high energy ones will drift through with partial or insignificant change of the energy, because the energy gain is proportional to the time spent in active sector. Drift trajectories of the energetic particles before and during dipolarization are shown by dotted and solid lines respectively. In the middle of the active region satellite will register particles coming from the "old" position before the dipolarization, while during dipolarization they will come from the "new" position, where radiation belt maximum is closer and intensity is higher. That creates effect of the particle increase due to the shift of the drift shells without acceleration. During our substorm dipolarization 90 keV was the upper limit of electrons received real acceleration, but if substorm activations follow each other in a short time, which is not a rare occasion, then the upper limit of the energy of accelerated electrons might be as large as several hundreds of keV. For energies higher than 300-700 keV the overall losses due to pitch-angle scattering became more effective than acceleration and geostationary satellites register fast decrease of the intensity during intense substorms and magnetic storms. Subsequently the fluxes of these high energy electrons may increase to levels that exceed the pre-storm level, due to a combination of radial diffusion on magnetic impulses [Tverskiy

Lazutin L. et al.: Case study of multiple-onset substorm of March 12, 1991

(1968)], and local acceleration by resonant wave-particle interactions with whistler mode chorus waves [e.g., Horne and Thorne (1998); Meredith et al. (2003)].

Important remark must be made: the described process does not correspond to the accepted name "particle injection" and moreover "injection from the magnetotail". In-situ magnetic field dipolarization with small radial displacement is sufficient for the explanation of the auroral electron acceleration.

Localized activation

Within the active region the increase of electrons in 50 - 100 keV energy ranges was very fast, 10s, and accompanied by large $\frac{\delta B}{\delta t} \sim 7 \frac{nT}{s}$, which is indicative of large induced E-field acceleration. Restrictions of the temporal resolution of the electric field does not allow to apply this data for the analysis of the acceleration process. We only can say that electric field was strong, detector saturated at more than $10 \frac{mV}{m}$ in all components.

From our substorm study we found that two electron populations are participating in the local activation effects: not only the energetic auroral electron just discussed above, but also low-energy auroral electrons activated by field-aligned acceleration. They are registered nearly simultaneously, but as was shown above (part 4.2), there exist certain difference in temporal and spatial behaviour.

We cannot for sure choose the acceleration mechanism. Model of Heikkila and Pellinen (1977) includes parallel electric field component outside the neutral sheet. This component is a sum of induced and polarization electric fields and accelerates particles along magnetic field lines. Induced field is most possible but not the only one possible source. Electron acceleration along the magnetic field may be associated with the cross-field current instability [Lui et al., 1991], which occurs in the current disruption region. Abel et al. (2002) found that during field-aligned electron events observed by LEPA on CRRES often occurs pitch-angle scattering accompanied by electron acceleration, possibly due to wave-particle interactions. Besides, they suggest that this process provides hot plasmasheet particles from the ionosphere to the equatorial region. Nevertheless no one of the mentioned mechanisms can explain a fine structure in the behaviour of the lower < 3 keV energy electrons with $PA \sim \leq 30^\circ$ near this dipolarization moment.

Relation of the low and high energy auroral electrons remains one of the important but poorly illuminated problem of the substorm science. We here only slightly touched this problem.

Although we do not know exact mechanism of the localized acceleration we can see their role in global substorm acceleration process as a source of the low and middle energy electrons for the further acceleration by betatron described above.

7 Conclusions

We have used ground-based and satellite data to study the substorm structure and particle dynamics in the inner magnetosphere associated with the multiple-onset substorm event of March 12 1991. We describe the substorm growth phase and expansion, auroral dynamics, current development, Harang discontinuity and WTS propagation. With a good temporal and spatial resolution details emerge which are absent from the accepted scheme. The total picture becomes more complicated, with simple local substorms inserted inside each other. We studied auroral and radiation belt electron and ion dynamics in conjugate magnetosphere quasitrapping region associated with substorm development.

Our main conclusions are as follows:

1. We find it difficult to fit our substorm with existing concept of the phases following one another, although it would be possible at lower spatial and temporal resolution. Our proposed scheme is a combination of global processes controlled by solar wind electric field and local activations of different intensity prepared and directed by local conditions.
2. Our scheme may explain observed activity including such findings as
 - Two substorms or substorm intensifications were observed simultaneously in different longitude sectors.
 - Different substorm phase signatures (growth and expansion) were recorded simultaneously within same longitude sector on different latitudes .
3. Transition from the growth phase to the expansion consists of the chain of localized undeveloped activations, pseudobreakups and onsets with increasing intensity near T_0 . and can be divided into two parts: slow and fast poleward expansion. That agree with two-stage substorm onset models proposed earlier.
4. Two auroral arcs prepared during the late growth phase may be a predestinated place for the double substorm onset with first activation on the most equatorial arc and second at the next poleward one. That indicates that toward the end of the growth phase existed at least two regions in magnetosphere where conditions were close to the instability limit. Delay of the north breakup confirm tailward propagation at the activity.
5. Ion and electron substorm injections have different origins. The electron increase closely correlates with the magnetic field dipolarization, whereas the energetic proton increase starts about 2 minutes before the onset and 4-5 minutes before the magnetic field dipolarization.
6. We find that the ion energy density increases several minutes before the local activations and decreases immediately after onset. Low-energy (< 15 keV) and high

Lazutin L. et al.: Case study of multiple-onset substorm of March 12, 1991

energy (>50 keV) ions are two species involved into substorm activity. Middle energy ions remain passive during late growth phase and expansion time. The importance of the quasitrapped ions with energy higher than 50 keV activity deserve special attention. We may suppose that ion acceleration is a result of the resonant interaction with a turbulence come into sight as magnetic pulsations, auroral arc curls or vortexes structures. However, most of the ion dynamics which may be a key to the substorm instability remain a puzzle.

7. Growth phase activations are not just an unsuccessful attempt to start substorm expansion. Their coincidence with step-like auroral ion enhancements with increasing energy of accelerated ions suggests that it is important and possibly necessary process which creates critical conditions for the substorm breakup and expansion.
8. The increase in the auroral electron flux during the substorm expansion, known as an injection, is a composition of field-aligned, inductive and betatron acceleration and magnetic drift shell radial displacement. The latter prevails for the high energy electrons, the pure acceleration effects for the soft particles, and a combination of betatron acceleration and drift shell displacement for the middle-energy auroral electrons. We were able to trace transformation of the central plasmashet 0.1 - 10 keV electrons into 10 - 100 keV auroral electrons which creates most of known precipitation effects and supplies the radiation belts with fresh particle flux.
9. We investigated the fine structure of one of the local activation onset in the vicinity of the CRRES. For the first time we show that keV field-aligned electrons (and upward current) appear before dipolarization and energetic electron increase. The transformation of energy spectrum of the middle-energy electrons differs from the accelerated by betatron mechanism and suggest induced electric field or other types of acceleration.
10. Both ion and electron substorm injections are the result of local acceleration in the quasitrapping region without transport from the magnetotail region. Several steps of the acceleration can be assumed, with the ionosphere and solar wind as an initial source of low energy inner plasmashet population later transformed into auroral and trapped radiation.

Acknowledgements. The authors are grateful to observers and scientist responsible for the ground based magnetic and auroral observations (IMAGE, PGI, AASI). The authors thank the SAMNET team for magnetometer data. SAMNET is a PPARC National Facility operated by Lancaster University. Pi2 pulsations data of the Borok observatory were presented by Dr. S.V.Anisimov. The authors thanks PI and their team for CRRES particle, magnetic and electric field data. TVK and BVK work was supported by the Division of Physical Sciences of the Russian Academy of Sciences (program DPS-18). Presenting of this study at the 31st Annual Meeting on Atmospheric Studies by M.A. Danielides would have not been

possible without the kind support by the University of Oulu and the Finnish EISCAT project by Prof. T. Nygren.

References

- Abel, G. A., A. N. Fazakerley, and A. D. Johnstone, The simultaneous acceleration and pitch angle scattering of field-aligned electrons observed by the LEPA on CRRES, *J. Geophys. Res.*, 107, 112, doi:10.1029/2001JA005090, 2002.
- Akasofu, I., W. Baumjohann, Y. Kamide et al., The roles of direct input of energy from the solar wind and unloading of stored magnetotail energy in driving magnetospheric substorms, *Space Sci. Rev.*, 46, 93-111, 1987.
- Akasofu, S.-I., *Polar and magnetospheric substorms*, Dordrecht-Holland: D.Reidel, 1968.
- Anderson, K.A. and Enemark, D.C. , Balloon observations of X-rays in the auroral zone, *J.Geophys.Res.*, 65, 3521-3541, 1960.
- Arnoldy R. L. and T.E. Moore, Longitudinal structure of substorm injections at synchronous orbit, *J.Geophys.Res.*, 88, A8, 6213-6220, 1983.
- Birn J., M.F. Thomsen, J.E. Borovsky et al., Characteristic plasma properties during dispersionless substorm injections at geosynchronous orbit, *JGR*, 102, A2, 2309-2324, 1997.
- Büchner J., and Zelenyi L.M. , Regular and chaotic particle motion in magnetotail-like field reversals. 1, Basic theory of trapped motion, *J.Geophys.Res.* , 94, 11821-11842, 1989.
- Elphinstone, R.D. , Observations in the vicinity of substorm onset: Implications for the substorm process, *J. Geophys. Res.*, 100, 7937-7969, 1995.
- Elphinstone, R.D., J.S. Murphree, and L.L. Cogger, What is a global auroral substorm?, *Rev. Geophys.*, 34, 2, 169-232, 1996.
- Erickson G.M., Maynard N.C., Wilson G.R. et al., Electromagnetics of substorm onset in the near-geosynchronous plasma sheet, *Substorm-5*, ESA SP-443, 385-388, 2000.
- Fedorova N., V. Tsirs and L. Lazutin, Impulsive increase of the proton aurora brightness before the beginning of the active substorm phase, *Geomagn. and Aeronomy*, 1, 28-87, 1988. (R)
- Friedel R.H.W., A. Korth, G.D. Reeves et al., Origin of energetic particle injections at substorm onset as measured by the CRRES spacecraft between 4 and 7 Re and Los Alamos geostationary satellites, *Proc.of the Second Int.Con.on Subs.* 2, 571-576, 1994.
- Hardy, D. A., D. M. Walton, A. D. Johnstone et al., Low Energy Plasma Analyzer, *IEEE Trans. Nucl. Sci.*, 40, 246-251, 1993.
- Heikkila W.J., and R.J. Pellinen, Localized induced electric field within the magnetotail, *J. Geophys. Res.*, 82, 10, 1610-1614, 1977
- Horne, R.B., and R.M. Thorne, Potential waves for relativistic electron scattering and stochastic acceleration during magnetic storms, *Geophys. Res. Lett.*, 25, 3011- 3014, 1998.
- Isaev S.I. and Pudovkin M.I., *Polar aurora and the Earth magnetosphere processes*, Nauka, 1972. (R)
- Klumpar D. M., J. M. Quinn, and E. G. Shelley et al., Counterstreaming electrons at the geomagnetic equator near 9 Re, *Geophys. Res. Lett.*, 15, 11, 1295-1298, 1988.
- Konradi A., Semar C.L., and Fritz T.A., Substorm -injected protons and electrons and the injection boundary model, *J.Geophys.Res.*, 80, 543-552, 1975.
- Kornilova, T.A., Pudovkin, M.I., and Starkov, G.V. et al., Fine Structure of Aurorae near Polar Boundary of the Auroral Bulge during Breakup Active Phase, *Geomagn. Aeron.*, 30, 150-258, 1990. (R)

Lazutin L. et al.: Case study of multiple-onset substorm of March 12, 1991

- Kornilova, T.A., I.A. Kornilov, Pudovkin, M.I. et al., Two types of auroral breakup, *Substorm-6*, ESA SP-443, 307-311, 2000.
- Kornilova, T.A., I.A. Kornilov, Pudovkin, M.I. et al., Poleward propagation of the aurora during explosive phase, *Geomagn. Aeron.*, 38, 1, 51-90, 1998. (R)
- Kornilova, T.A., Pudovkin, M.I., Kornilov I.A. et al., Auroral arc dynamics during double breakup events, *Geomagn. Aeron.*, 41, 3, 150-258, 2001. (R)
- Korth A., Z.Y. Pu, G. Kremser, and A. Roux, A statistical study of substorm onset conditions at geostationary orbit, ed. by J. R. Kan, T.A. Potemra, S. Kokubun, and T. Iijima, AGU, Washington, DC, p. 343-347, 1991.
- Korth, A., G. Kremser, B. Wilken et al., Electron and proton wide-angle spectrometer (EPAS) on the CRRES spacecraft, *J. Spacecr. Rockets*, 29, 609-614, 1992.
- Kozelova T., L. Lazutin, B. Kozelov et al., Multiple-onset substorm case study: pre-onset, auroral onset and expansion, *Substorm-7*, Helsinki, p. 176-181, 2004.
- Kozelova T. V., V. B. Lyatsky, Field-aligned current at the front of WTS, *Geomagnetism and Aeronomy*, 24, 228- 231, 1984.
- Kozelova T.V., Lazutin L.L., Kozelov B.V. et al., Dynamic injections, reconfiguration of magnetic field and equivalent magnetospheric currents as observed by CRRES, ESA SP-389, 429-434, 1996.
- Kozelova T. V., Lazutin L. L., Pudovkin M. I. et al., The electric field behaviour in the magnetosphere on 6.6 RE within the active region during the substorm, *Geomagnetism and Aeronomy*, 26, 621 - 627, 1986. (R)
- Kozelova T.V., Kozelov B.V., and Lazutin LL. et al., Changes of the magnetospheric cross-field current during substorm expansion phase as observed by CRRES, *Substorms-4*, ESA SP-443, edited by S. Kokubun and Y. Kamide, 393-396, Terra, Tokyo, 1998
- Kozelova T. V., Kozelov B. V., and Lazutin L. L. et al., Particle diamagnetism and local dipolarization, *Geomagnetism and Aeronomy*, 43, 479-488, 2003 (R)
- Kremser, G., On the relationship between auroral zone X-ray bursts and polar magnetic substorms, Ortner J., Maseland H., (ed) *Solar terrestrial relations*, Univ. Calgary, Canada, 415, 1970.
- Kremser, G., Bjordal J., Block L.P. et al., Coordinated balloon-satellite observations of energetic particles at the onset of magnetospheric substorms, *J. Geophys. Res.*, 87, 4445 - 4453, 1982.
- Kremser, G., A. Korth, S. L. Ullaland et al., Field-aligned beams of energetic electrons (16 keV - E- 80 keV) observed at geosynchronous orbit at substorm onsets, *J. Geophys. Res.*, 93, 14,453-14,464, 1988.
- Lazutin, L.L., X-ray emission of auroral electrons and magnetospheric dynamics, *Physics and Chemistry in Space*, v.14, Springer-Verlag, Berlin-Heidelberg, 1986.
- Lazutin L. L. and T. V. Kozelova, The Structure of Substorm Activations in the Quasi-Trapping Region, *Cosmic Research*, 42, 4, 309-331, 2004.
- Lazutin L., T. Kozelova, R. Rasinkangas et al., Radiation belt proton contribution to substorm structure and dynamics, *Substorms-4*, edited by S. Kokubun and Y. Kamide, pp. 547-550, Terra, Tokyo, 1998a.
- Lazutin L. L., R. Rasinkangas, T. V. Kozelova et al., Observations of Substorm Fine Structure, *Ann. Geophysicae*, 16, 775-786, 1998b.
- Lazutin L.L., A. Korth, T. Kozelova et al., Fast Bursts of High Energy Protons and Their Role in Triggering of the Substorm Onset Instability, *Sixth International Conference on Substorms*, March 25-29, 2002 Seattle, Washington, USA, 340-346, 2002.
- Liou K., C.-I. Meng, T.Y. Lui et al., On relative timing in substorm onset signatures, *J. Geophys. Res.*, 104, 22807-22817, 2003.
- Lui, A. T. Y., A synthesis of magnetospheric storm models, *J. Geophys. Res.*, 96, 1849-1856, 1991.
- Lui, A. T. Y., R. E. Lopez, S. M. Krimigis et al., A case study of magnetotail current sheet disruption and diversion, *Geophys. Res. Lett.*, 15, 721-724, 1988.
- Lui, A. T. Y., R. E. Lopez, B. J. Anderson et al., Current disruptions in the near-Earth neutral sheet region, *J. Geophys. Res.*, 97, 1461-1480, 1992.
- Lyons, L.R., I. O. Voronkov, J. M. Ruohoniemi et al., Substorms: Externally Driven Transition to Unstable State a few Minutes Before "Onset", *Substorm-6*, ISC-6, 47 - 54, 2002.
- Lyons L.R., Wang C.-P., Nagai T. et al., Substorm inner plasma particle reduction, *J. Geophys. Res.*, 108, A12,1426 - xxx, 2003.
- MacAulay, A.K., Rankin, R., Frycz et al., Substorm intensifications and resistive shear flow-ballooning instabilities in the near-Earth magnetotail, *Substorm-3*, ESA SP-389, 399-404, 1996.
- Maynard, N.C., Burke, W.J., Basinska et al., Dynamics of the inner magnetosphere near times of substorm onsets, *J. Geophys. Res.*, 101, 7705-7736, 1996.
- Meredith, N.P., M. Cain, R.B. Horne et al., Evidence for chorus-driven electron acceleration to relativistic energies from a survey of geomagnetically disturbed periods, *J. Geophys. Res.*, 108, A6, doi:1248, 2003.
- Oguti, T., Hydrogen emission and electron aurora at the onset of the auroral breakup, *J. Geophys. Res.*, 78, 7543-7547, 1973.
- Ohtani, S., Takahashi, K., Zanetti et al., Initial signatures of magnetic field and energetic particle fluxes at tail reconfiguration: Explosive growth phase, *J. Geophys. Res.*, 97, 19311-19324, 1992.
- Opgenoorth H.J., Bromage B., Fontaine D. et al., Coordinated observations with EISCAT and the Viking satellite: the decay of a westward travelling surge, *Annales Geophysicae*, 7, (5), 479-500, 1989.
- Pellinen, R.J. and W.J. Heikkila, Observations of auroral fading before breakup, *J. Geophys. Res.*, 83, 4207 - 4217, 1978.
- Perraut, S., O. Le Contel, A. Roux et al., Evidence for Substorm Trigger, *Proc. of the International Conference on Substorms-4*, March 9-13, 1998, Lake Hamana, Japan, Terra Scientific Publ. Comp., Tokyo, Japan, and Kluwer Academic Publishers, Norwell, MA, USA, 349-354, 1998.
- Pudovkin, M.I., Zaitseva, S.A., Kornilova, T.A. et al., Dynamics of Aurorae in the Region of Equatorial Edge of Auroral Zone, *Geomagn. Aeron.*, 35, 3, 47-54, 1995.
- Rasinkangas, R., Sergeev, V.A., Kremser et al., Current disruption signatures at substorm onset observed by CRRES, *J. Proceedings of the Second International Conference on Substorms*, edited by Kan, J.R., Craven, J. and Akasofu, S.-I. Alaska: Geophys. Inst. Fairbanks, Alaska, 595-598, 1994.
- Rostoker, G., S.-I. Akasofu, W. Baumjohann et al., The roles of direct input of energy from the solar wind and unloading of stored magnetotail energy in driving magnetospheric substorms, *Space Sci. Rev.*, 46, 93-111, 1986.
- Rostoker, G., Akasofu, S.-I., Foster, J.C. et al., Magnetospheric substorms-definition and signatures, *J. Geophys. Res.*, 85, 1663-1668, 1980.
- Rostoker G., Phenomenology and physics of the magnetospheric substorms, *JGR*, 101, 222-233, 1996.
- Rostoker, G., S.-Roux, A., Perreault et al., Plasma sheet instability related to the westward travelling surge, *J. Geophys. Res.*, 96, 17697-17707, 1991.

Lazutin L. et al.: Case study of multiple-onset substorm of March 12, 1991

Roux, A., Perreault, P., Robert, P., et al., Plasma sheet instability related to the westward travelling surge, *J. Geophys. Res.*, 96, 17697-17707, 1991.

Samson J.C., L.R. Lyons, P.N. Newell et al., Proton aurora and substorm intensifications, *Geophys. Res. Lett.*, 19, 2167 - 2170, 1992.

Singer H.J., W.P. Sullivan, P. Anderson et al., Fluxgate magnetometer instrument on the CRRES, *J. Spacecraft Rockets*, 29, 4, 599-601, 1992.

Tverskoy B.A., Dynamics of the Earth's radiation belts, Nauka, M., 1968. (R)

Vorobiev, V.G. and Rezhnev, Progressive westward displacement of the region of the auroral substorm localizations in: Substorms and magnetospheric disturbances, ed. Isaev S.I., "Nauka", 103-115, 1973. (R)

Voronkov I., R. Rankin, J.C. Samson, et al., Shear flow instability in the dipolar magnetosphere. *J. Geophys. Res.*, 104, A8, 17323-17334, 1999.

Voronkov, I.O., E. F. Donovan, P. Dobias et al., Near-Earth Breakup in Substorms: Empirical and Model Constraints, Substorm-6, ISC-6. Proceedings, 270-277, 2002.

Weiss L.A., P.H. Reiff, R.V. Hilmer et al., Mapping the Auroral Oval into the Magnetotail using Dynamics Explorer Plasma Data, *J. Geomag. Geoelectr.*, 44, 1121-1144, 1992.

AURORA OPTICAL EMISSIONS RELATED TO IMAGING RIOMETER OBSERVATIONS

P H Stoker and J Bijker

Unit for Space Physics, Potchefstroom Campus, North-West University,
POTCHEFSTROOM, South Africa

ABSTRACT

Observations during a substorm expansive phase at the South African Antarctic base SANAE IV (L=4.1) showed that the 630.0 nm aurora spectral line followed closely the variations in the aurora white light (mainly green and blue spectral lines), and preceded the white light variations from about 0 to 5s during the time of observation of the pre-midnight substorm on 19 July, 2003. Absorptions in cosmic radio noise appeared to vary both related and unrelated to optical emissions. Related variations were delayed relative to optical variations from 2 to 12 s. These temporal differences in variations support the idea of a local dispersionless acceleration region associate with the expansion phase of the substorm. The temporal differences suggest an increasing electric field as acceleration mechanism. The unrelated absorptions in cosmic radio noise had then to originate from a different acceleration region.

1. Introduction

At high latitudes energetic electrons and ions are precipitated frequently from the magnetosphere into the Earth's upper atmosphere, in particular during magnetic storms. One of the major effects of precipitation is the excitation and ionization of neutral and ionic species in the upper atmosphere. Medium energy (~0.5 – 20 keV) particles are responsible for visible aurora. More energetic electrons will enhance ionization down into the D-region, which is most effectively recorded by a riometer at ground level as absorption of cosmic radio noise.

The intensity of cosmic radio wave noise of ~10-m wavelength is attenuated in the D and E regions of the ionosphere due to the dominance of electron-neutral collisions. Several authors reported on absorption in the F-region where electron-ion collision dominates. Wang et al. (1994) showed that the combination of high electron density and low electron temperature can result in high electron-ion collision frequency with the consequent increase in absorption as observed by riometer. They reported on an absorption of ~0.3 dB observed with an F region patch of drifting ionization that passed at a height of 300-400 km overhead.

Hartz and Brice (1967) studied the latitudinal and diurnal variations of ten years of aurora data from optical, very high frequency (VHF) radio wave forward scattering and cosmic radio noise absorption (CRNA) observations. During the geomagnetic midnight sector, the CRNA, caused by precipitation of more energetic electrons than for optical aurora, is occasionally observed together with optical aurora.

White light recordings of aurora include mainly the green 557.7 nm line from the O(¹S) excited state and the blue 427.8 nm line from excited N₂⁺. These lines are produced in

E- and F-regions at altitudes above 100 km at night, where the electron collision frequency is sufficient low to expect magnetic-field-aligned currents. Aurora CRNA recordings appeared to be associated with altitudes of the order of 80 km, where the electron collision frequency is great enough for significant cosmic radio wave absorption and where field aligned ionization structures are not expected.

Stoker et al. (1996, 1997) reported on spatial and temporal differences observed between white light aurora emissions and CRNA during magnetic substorms in the local midnight sector. Changes in absorption appeared to be delayed relative to changes in luminosity. In a particular viewing direction the delays appeared to vary between 0 and 60 s. Their main conclusion was that regions of ionospheric absorption are distinctly different from regions of high luminosities. If the latter regions are considered as regions of upward field-aligned currents (e.g. Potemra, 1979), cosmic radio waves appear not to be absorbed strongly in these regions. Furthermore, the existence of these two distinct regions implies two different categories of electron precipitation within different energy ranges, in line with the observations of Hartz and Brice (1967).

In addition to CRNA and white light aurora recordings, we have now recorded also the red 630.0 nm oxygen line, of which emissions are expected to peak above 200 km. In this study the spatial and temporal variations of the red aurora line are compared with variations in the white light aurora and in CRNA during the expansion phase of a substorm. These observations have to be due to an acceleration process associated with the pre-midnight substorm on 19 July, 2003.

2. The instrumental setup for this study

The South African Antarctic research station SANAE IV ($70^{\circ} 40' S$, $02^{\circ} 51' W$, $L=4.1$, corrected magnetic co-ordinates $-60^{\circ} 04'$, $44^{\circ} 33'$) is situated on the equatorial side of the aurora oval well inside the quiet time trapping boundary. During midnight, when the magnetic index $K_p > 3$, this oval starts to overlap the region of the harder precipitation causing aurora CRNA.

Aurora events are studied from video recordings of all-sky optical aurora and the 64 beam imaging riometer at SANAE IV (Wilson and Stoker, 2002). Digitized all-sky low level white light images of optical aurora emissions are mapped onto the angular directivity functions of the 64 beams of the imaging riometer in order to interrelate the spatial structures of optical emissions and CRNA. Now the luminosity of the 630.0 nm red aurora spectral line has been recorded with a narrow angle video camera, having a field of view of 25° . The optical emission of the red oxygen line is expected to peak above 200 km since at lower altitudes the excitation of the $O(^1D)$ state is quenched substantially by collision with other atmospheric constituents, reducing the number of 630.0 nm photons emitted by this state.

Since CRNA and optical aurora are recorded as functions of angular directions, spatial profiles at different altitudes will appear displaced from each other. Thus, CRNA structures at ~ 90 km will be seen displaced relative to those of white light optical emissions at ~ 115 km in directions inclined to zenith. The most inclined imaging riometer beams, projected to 115 km altitude, extend a factor of about 1.26 further away from the zenith than the beams projected to 90 km. These relative displacements are however

too small relative to the beam widths to be taken into account when images of the same angular directions are intercompared (Wilson and Stoker, 2002).

The 630.0 nm red aurora line, emitted at altitudes above 200 km, is recorded by the narrow angle video camera, of which the field of view of 25° covers only the inner 12 beam directions of the imaging riometer. Here again are the relative displacements of the projected images of the 12 inner beams too small to be taken into account.

Electrons are precipitated from the magnetosphere into the ionosphere during a substorm. The signatures of a substorm and the different phases of a substorm are inferred from variations in the three components of the local geomagnetic field and the geomagnetic pulsations at SANAE IV.

3. Substorm initiated temporal and spatial variations on 19 July, 2003

From the CDAWeb Data Explorer on the NASA internet, it appears that the hourly values of the B_z component of the interplanetary magnetic field (IMF) varied between +4 and -4 nT during 19 July, 2003, but at the 21st hour UT the B_z component turned southward to -7 nT, remaining southward the following hour at -9 nT, and turned northward again during the 23rd hour. Strong magnetic pulsation activity started at SANAE at about 23:28 UT. At the same instance small positive precursors appeared on the H, D and Z components of the geomagnetic field, followed by negative magnetic bays in both the H and Z components. These are signatures of the commencement of a substorm (Rostoker et al., 1980). Evidence shows that northward turnings of the IMF after an interval of sustained southward IMF can trigger the onset of major substorm expansive phase effects (Rostoker, 1983).

In Figure 1 the black curves are the one second absorptions of the 38.2 MHz cosmic radio noise in the directions of the inner 16 beams of the 8x8 imaging riometer, plotted from 23:36:00 – 23:45:00 UT on 19 July, 2003. The Y-axes give the absorption in dB. The green curves display the one second convoluted optical intensities in the inner 16 beam directions of the 64 beam imaging riometer for this interval, normalized to the scales of the Y-axes. These optical intensities have been derived by mapping the video cameras' pixel recordings onto the sensitivity functions of the different beam directions defined by the 8x8 crossed dipole antenna array of the imaging riometer (Wilson and Stoker, 2002). Because of the 25° field of view of the lens of the video camera with the red 630.0 nm filter, only the inner 12 beam directions could be convoluted and these were plotted as red curves in Figure 1.

A strong aurora arc appeared at about 23:36:00 UT just North and just East of zenith at SANAE, flaring to a first maximum intensity at 23:36:10 UT in beam directions 21, 29, and 37 of the 64 beam imaging riometer. The second flaring of this arc gave a strong maximum at 23:36:22 in beam direction 29 (see Figure 1). The recording of the narrow angle aurora camera with the red filter started at 23:36:21 UT, close to maximum intensity of this second flaring of the arc.

Only in beam directions 21, 29 and 30 a small well-defined absorption peak was recorded. This peak seems to be associated with the second maximum of the optical emissions with a delay of about 5 ± 3 seconds relative to the second peak in the white

(green curve) and red light recordings. The peaks in the white and red light recordings coincided in time with an uncertainty of 1 second.

This initial strong arc causing luminosity peaks at 23:36:10 and 23:36:22 UT disappeared quickly and an arc of lesser intensity appeared just North-West of zenith about 20 seconds later, giving rise to the first peaks of the optical recordings in beam direction 27, without related increase in absorption in the recordings of the imaging riometer.

A set of well-defined optical and absorption peaks was recorded in the time interval 23:38:11-23:38:28 UT, corresponding to the first broad maximum of 2.4 dB in Figure 2. In this Figure 2 is plotted the one second absorption recorded by the 30 MHz broad beam double dipole riometer. The absorption peak in Figure 1 was delayed by 5 ± 1 s relative to the white light peak in beam directions 21 and 29, and was coincident with the white light peak in beam directions 36, 38 and 45. In beam directions 21, 29, 30, 37 38 and 45 the red light peak was on the average 3 ± 1 s earlier than the white light peak.

The maxima of the last set of well-defined peaks recorded by the imaging riometer were in the interval 23:41:56-23:42:19 UT, corresponding to the appearance of the first 3.4 dB peak in Figure 2. In Figure 1 the delay in absorption maximum of well-defined peaks in seven frames, relative to the white light maximum varied between 2 and 12s, with an average of 7 ± 2 s. The red light peak was earlier than the white light peak by 1 ± 1 s.

Absorption variations (black curve) follow usually, with a few seconds delay, optical variations. A striking exception during the interval of 23:36:00-23:45:00 UT is the large absorption peaks that appeared at 23:43 UT in frames of beam directions of the first column of Figure 1. These peaks are hardly noticeable in beam directions eastward from the first column, that is to the right of this column. The absorptions are even larger in beams to the left (westward) of this column, that is in the direction of the column of the 8 beams numbers 2, 10, 18, 26, 34, 42, 50 and 58, which are adjacent to the column of 8 beams 3, 11, 19, 27, 35, 43, 51 and 59.

The legitimacy of these strong absorption peaks, unaccompanied by increases in optical intensities, is confirmed by the appearance of the last absorption peak of 3.5 dB in Figure 2, which was recorded independently by the 30 MHz broadband riometer. This peak's maximum absorption of 3.5 dB was at 23:43:07 UT. Within the time span of this peak, the imaging riometer observed, as displayed in Figure 1, the maximum absorptions in the beam directions of 19, 27, 35 and 43, respectively, at 23:42:57 (3.1 dB), 23:42:58 (4.4 dB), 23:43:02 (3.9 dB) and 23:43:06 UT (3.2 dB). This absorption event with maximum at 23:43:07 UT was also recorded by the 52.4 MHz crossed dipole broadband riometer.

4. Discussion

The brightest visible feature of the optical aurora is the green line at 557.7 nm which is due to transition of an electron from the 1S excited state to the 1D excited state of atomic oxygen. The 630.0 nm red line is emitted as the 1D state relaxes to the ground state. This excited state is quenched substantially below ~ 200 km by collision with other atmospheric constituents.

It is important that the red line is recorded with a filter of narrow spectral width in order to exclude contamination by other spectral lines. The red line filter we have used on the narrow angle video camera was accurately calibrated. The mean wavelength was 630.3 nm with a full width at half maximum of 2.4 nm. We are therefore confident that the red line recordings were uncontaminated by other strong spectral lines that are in the white light recordings.

Figure 1 images spatial variations that depend on the energy of precipitation electrons. The aurora red (OI) line is due to both the precipitation of low-energy electrons ($\ll 1$ keV) and a process called thermal excitation, peaking well above 150 km, probably at the altitude of 250 km in the upper F-region. The white light recordings are mainly from the green 557.7 nm line from the $O(^1S)$ excited state and the blue 427.8 nm line from excited N_2^+ . These lines are produced in E- and F-regions at altitudes above 100 km at night, by electron precipitation energy ~ 1 to 20 keV. Absorption of cosmic radio noise, recorded by riometers, are mainly due to excess ionization in the D-region below 100 km, by electrons that precipitate from the magnetosphere with energies > 10 keV.

The plots in Figure 1 provide overall a scenario that temporal variations of the red line tend to lead the variations in the white light recordings, preceding the latter variations from 0 to about 5 s. Furthermore, the variations in cosmic noise absorption lag the variations in white light from about 2 to 12 s.

One of the most repeatable features associated with substorms in the near-Earth ($r \leq 10 R_E$) magnetotail is the variation in the flux of energetic particles (Lopez et al., 1989). Sudden increases in particle fluxes observed by satellites on the nightside magnetosphere are associated with the substorm expansion phase (Friedel et al., 1996 and references therein). Yeoman et al. (1994) showed in a statistical study that injection events near geostationary satellites show good correlation with Pi2 pulsations as reliable substorm indicators. Geostationary satellite Goes 8 showed a fast increase of energetic electrons ($E > 2$ MeV) at 23:28 UT on 19 July, 2003, coinciding with onset of strong magnetic pulsation and confirming the substorm onset.

When a geosynchronous satellite observes the substorm onset as perfectly dispersionless, then the satellite can be said to be in or sufficiently close to the particle acceleration region so that drift times are unimportant. Friedel et al. (1996) found that near-dispersionless onsets occur as far in as $L = 4.3$ and are distributed well into the dawn and dusk sectors.

The variations displayed in Figure 1 showed no energy dispersion due to drift times in the sense that variations due to higher precipitation energies did not precede those of lower energies. We may accept, therefore, that the precipitating particles were fresh substorm electrons, which were accelerated locally, possibly by an increasing electric field, arising from a plasma instability associated with the expansion phase of the substorm. This will explain the observations that variations due to precipitation of lower energy electrons lead the variations due to higher energy electrons.

Variations in absorption of cosmic radio noise have also been observed unrelated with optical morphologies. The strong CRNA at 23:43 UT had no related variations in aurora luminosity. The flux of substorm electrons, causing this CNRA, must have been predominantly in the higher energies, larger than 20 keV. Presumably the precipitating

electrons, causing this CRNA, were from another acceleration region than the related variations.

5. Conclusions

The 630.0 nm aurora spectral line followed closely the variations in the aurora white light (mainly green and blue spectral lines) during the pre-midnight expansion phase of a substorm on 19 July, 2003, with delays between zero and up to about 5s. Furthermore, variations in cosmic radio noise absorption lag the variations in white light from about 2 to 12s. In terms of substorm injected electron spectra observed by satellites these variations are dispersionless. The particle acceleration region must, therefore, be sufficient close so that the higher energy particles do not lead the lower energies. The observed delays are presumably due to a local plasma instability, inducing for instance an increasing electric field associated with the expansion phase of the substorm. Variations observed in CRNA unrelated to optical variations, must then originate from a different acceleration region.

Acknowledgments. The data used in this paper was obtained and processed through the financial and logistic support to the South Africa National Antarctic Program by the Department of Environmental Affairs and Tourism. The accurate calibration of the aurora line filters by Dr Chen Chi Chu in the laboratories of the Department of Physics, University of Kwa-Zulu Natal, Durban, is acknowledged.

References

Friedel, R. H. W., A. Korth, and G. Kremser, Substorm onsets observed by CRRES: Determination of energetic particle source regions, *J. Geophys. Res.*, **101**, 13137-13154, 1996.

Hartz, T. R., and N. M. Brice, The general pattern of aurora particle precipitation, *Planet. Space Sci.* **15**, 301-329, 1967.

Lopez, R. E., A. T. Y. Lui, D. G. Sibeck, K. Takahashi, R. W. McEntire, L. J. Zanetti, and S. M. Krimigis, On the relationship between the energetic particle flux morphology and the change in the magnetic field magnitude during substorms, *J. Geophys. Res.*, **94**, 17105-17119, 1989.

Potemra, T.A., Current systems in the Earth's magnetosphere, *Rev. Geophys.* **17**, 640-656, 1979.

Rostoker, G., S. I. Akasofu, J. Foster, R. A. Greenwald, Y. Kamide, K. Kawasaki, A. T. Y. Lui, R.L. McPherron, and C. T. Russell, Magnetospheric Substorms – Definition and Signatures, *J. Geophys. Res.*, **85(A4)**, 1663-1668, 1980.

Rostoker, G., Triggering of expansive phase intensifications of magnetospheric substorms by northward turnings of the interplanetary magnetic field, *J. Geophys. Res.* **88** (A9), 6981-6993, 1983.

Stoker, P. H., M. J. Mathews, and M. W. J. Scourfield, Coordinated measurement of

auroral light intensities and riometric radio-wave absorption, *Geophys. Res. Lett.*, **23(6)**, 641-644, 1996.

Stoker, P. H., M. J. Mathews, and M. W. J. Scourfield, Cosmic radio noise absorption related to structures in aurora luminosity, *J. Geophys. Res.*, **102(A4)**, 7439-7447, 1997.

Wang, Z., T.J. Rosenberg, P. Stauning, S. Bass, and G. Crowley, Calculations of riometer absorption associated with F region plasma structures based on Sondre Stromfjord incoherent scatter radar observations, *Radio Sci.*, **29**, 209-215, 1994.

Wilson, A. and P.H. Stoker, Imaging riometer observations on energetic electron precipitation at SANAE IV, Antarctica, *J. Geophys. Res.*, **107(A10)**, SMP 2-1 – 2-10, 2002.

Yeoman, T.K., M.P. Freeman, G.D. Reeves, M. Lester, and D. Orr, A comparison of midlatitude Pi2 pulsations and geostationary orbit particle injections as substorm indicators, *J. Geophys. Res.*, **99**, 4085-4093, 1994.

CAPTIONS TO FIGURES

Figure 1: One second cosmic radio noise absorptions (black curve) and convoluted optical emissions (green and red curves) plotted from 23:36:00 to 23:45:00 UT for the inner 16 beam directions of the 64 beam imaging riometer at SANA E during the expansion phase of a substorm on 19 July, 2003. The green curves represent the one second optical intensities, convoluted from recordings by the white light all-sky video camera, while the red curves are the corresponding intensities recorded by a narrow angle video camera with a 630.0 nm filter. The scales of the Y-axes of the directional frames give the CRNA in dB, while the scales of the optical emissions are undefined. The frames are ordered with North upwards and East to the right.

Figure 2. The one second absorption plot from the recordings of the double dipole broadbeam 30 MHz riometer from 23:36:00 to 23:45:00 UT, 19 July, 2003. The broadbeam 52.4 MHz riometer showed a similar variation in absorption.

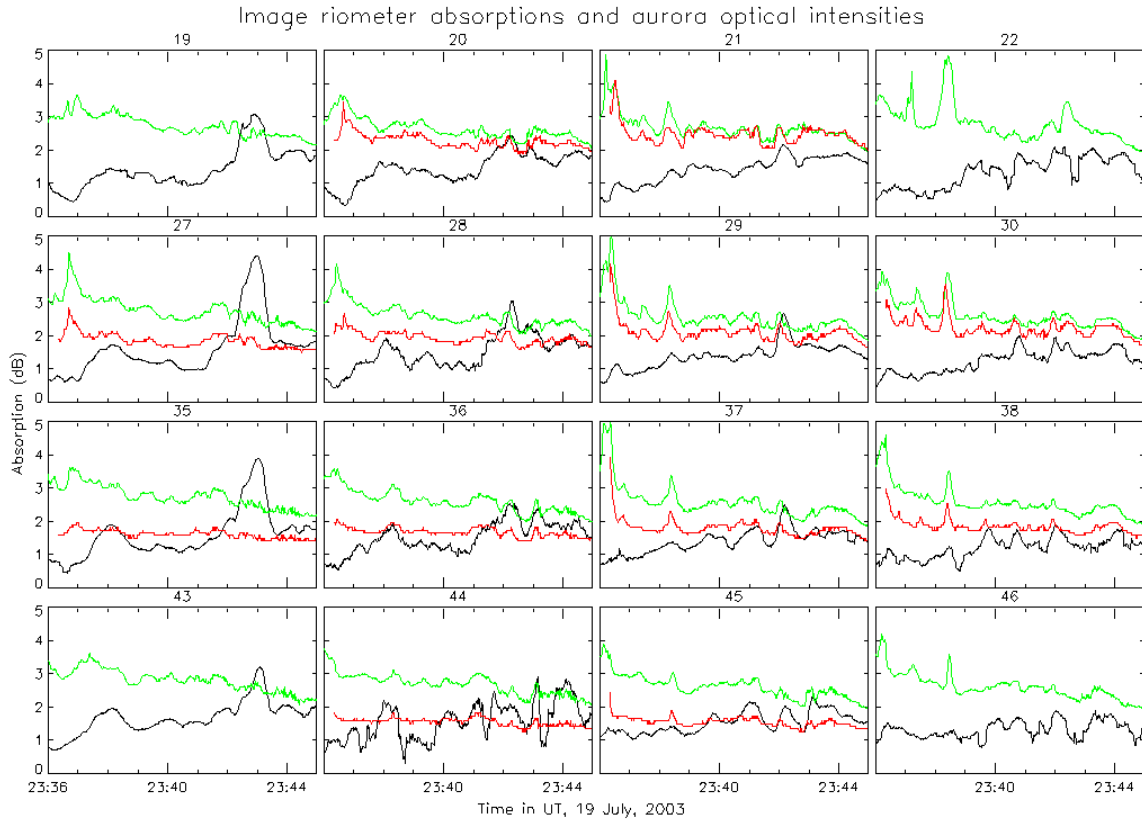


Figure 1

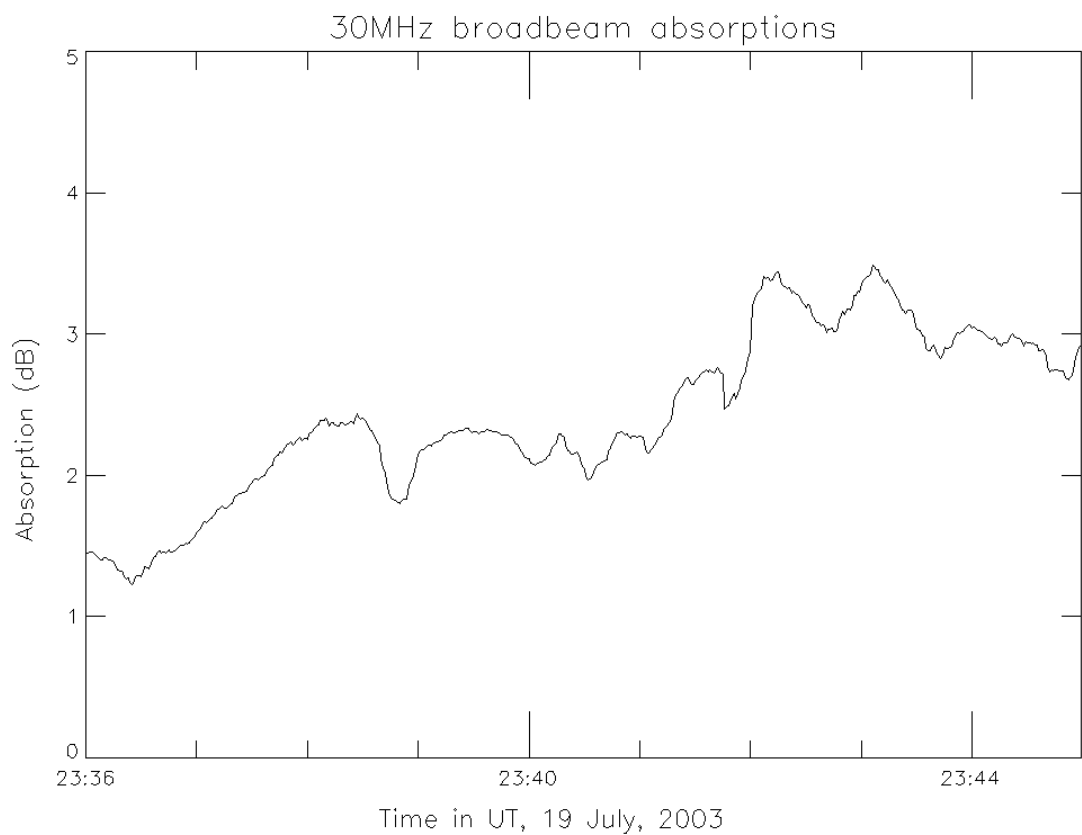


Figure 2

All-Sky camera network management of Finnish Meteorological Institute

Timo Sukuvaara¹, Jyrki Mattanen¹ and Sanna Mäkinen²

[1] {FMI Arctic Research Centre, Tähteläntie 62, FIN-99600 Sodankylä, Finland}

[2] {FMI Space Research, P.O. Box 503, FIN-00101, Helsinki, Finland}

Correspondence to: Timo Sukuvaara (timo.sukuvaara@fmi.fi)

Abstract

Finnish Meteorological Institute (FMI) possesses a network of all-sky cameras in the area of Northern Finland, Northern Sweden and Spitzbergen. The maintenance of this network is arranged by Arctic Research Centre of Finnish Meteorological Institute, located in Sodankylä. This paper gives an overview of the network, its equipment and the maintenance routines needed to upkeep the network.

Keywords: All-Sky Camera, Finnish Meteorological Institute, Auroral images

1 Introduction

The study of the Northern Lights as part of the electric and magnetic phenomena taking place in space close to the Earth provides valuable information on the characteristics and behaviour of the magnetosphere. Alongside traditional optical observation methods, equipment based on sophisticated research principles has been developed, and the FMI has also played an important role in interpreting the measurements obtained with these as part of international co-operation in this field. The Northern Lights are imaged and magnetospheric processes associated with them are observed by satellites. Long term observations continuing from one decade to the next, together with registration of the Earth's magnetic field, provide indirect information on fluctuations in the radiative activity of the sun. Long series of observations by the Finnish Meteorological Institute and its predecessors make a noteworthy contribution to this research topic.

This document concentrates on the FMI's All-sky camera network, providing remarkable part of the FMI's Northern Light research. First we will present the physical locations of cameras, followed by the technical structure of the cameras and the network. Furthermore, we present maintenance and calibration procedures of the network, and finally draw the conclusions. Further details about camera network and the cameras themselves can be found from (S.Mäkinen, 2001) and (M.T. Syrjäso, 1996).

2 The camera network

The camera network (the situation during the winter 2003-2004) is viewed in the Figure 1. The stations were located in Kevo (KEV), Spitzbergen (Longyearbyen LYR), Abisko (ABK), Kilpisjärvi (KIL), Hankasalmi (HAN), Sodankylä (SOD) and Muonio (MUO). It is worth of noting that Sodankylä camera station, unlike other stations, is mainly operated by Sodankylä Geophysical Observatory (SGO). However, both FMI and SGO have their own camera in that station.

The camera network location is changing year by year, as we are developing the system to better correspond to the auroral imaging needs. The changes taken place during this year are moving of the camera from Hankasalmi to Nyrölä (both locations are pretty much in the same neighborhood) and removing of Abisko camera.

3 Technical details of the cameras

Current All-sky cameras (ASC) are developed by KeoConsultants (USA). One camera is viewed in the Figure 2. Each camera has a telecentric optics, and the fish-eye lens without any vignetting. Cameras are controlled by computer with a frame grabber, located in the station. The overview of the camera station can be seen in the Figure 3. Filter consists of maximum of 7 different 2-inch narrow-bandpass filters, one of them typically missing in order to take "non-filtered" images. The imager used by the FMI contains only three filters. The center wavelengths of the filters are 427.8nm (blue colour), 557.7nm (green colour) and 630.0nm (red colour), and the bandpass width is approximately 2nm (FWHM, Full Width at Half Maximum). One All-Sky camera image taken with green filter is viewed in the Figure 4. The

filter-wheel is temperature controlled by an Athena XT16 temperature controller. There are two heater pads mounted inside the wheel housing.

The imager is composed of three parts: optical system, CCD camera and imager control electronics. The optical systems consists of a fish-eye lens, a shutter, telecentric optics in front of filter-wheel, a filter-wheel, an image intensifier, and relay optics.

The front fish-eye lens is a Canon 15mm/F2.8 with a 180° angular field-of-view (FOV). The fish-eye lens is followed by a series of lenses to make the system telecentric.

The shutter protects the filter and the image intensifier from direct sunlight. The shutter is opened before the image capture is started and closed after the frame grabber has acquired an image.

There is also a light sensor added to the camera system to further protect the image intensifier. The sensor is connected to the control electronics of the camera and it automatically cuts the power of the image intensifier if the ambient light level is too high. The image intensifier used is a Varo 25mm MCP Gen II Image Intensifier model 3603.

The output image of the intensifier is passed to the CCD camera through relay optics. The CCD camera is a Pulnix TM-765E with a spatial resolution of 768x512 pixels. The video output is a standard CCIR (composite black&white, 25 frames/s). The camera has an integrating feature which allows image capturing with longer than the video rate exposures. The integration and the image capturing is automatically handled by a computer.

Every aspect of the operation of the ASC is controlled by a computer. The shutter, filter-wheel, image intensifier and the CCD camera can all be operated by a computer along with the image acquiring using a frame grabber.

Each station has also three different interference filters (green, blue and red). Blurred images are amplified before final CCD-imaging and are then digitized to computer. Images are in black-and-white, colors are separated with filters. The use of light amplifiers allows the usage of short exposure times (typically 1000 ms). Cameras are installed to the station building below the transparent dome and controlled by the station computer.

The stations take images every 20 seconds during the dark time (sun is below the horizon). The location of the sun is pre-calculated, based on geographical coordinates, date and time. Imaging parameters are software configured and therefore easily changed. One image takes typically 300 kilobytes.

4 Calibration and management in Sodankylä

Cameras are collected during the spring to the yearly-based service. Cameras are dismantled, and optical elements, filters and shutter are carefully cleaned. Finally cameras are re-calibrated.

Calibration system is build around uniform light source system developed by Labsphere. The calibration environment has been installed into dark laboratory room. The laboratory, viewed in the Figure 5, is equipped with temperature stabilization. During the autumn all the cameras are returned to their measurement locations viewed in the map figure above. The measurements continue throughout the dark season.

The uniform light source used in the ASC calibration is a USS-1200V Uniform Source System manufactured by Labsphere. The system consists of an integrating sphere and a control unit. The output of the sphere can be adjusted by an attenuator attached to the sphere. A reference detector is used to monitor the output of the sphere. The detector reading is displayed by the integrating sphere system control. The calibration system is shown in Figure 6. The uniform light source system can be controlled by a remote computer. This enables adjusting the output of the sphere to a desired value and reading and recording the reference sensor reading by computer software.

The calibration of the all-sky cameras is needed in order to be able to use the acquired data more efficiently. All cameras are individuals with differences in filters, intensifiers and CCD-cameras. If one wants to be able to compare images taken with different cameras, the cameras need to be intensity calibrated in order to find out how measured brightness corresponds to the recorded intensity value.

The cameras also need to be geometrically calibrated. The idea of geometric calibration is to find the orientation of the cameras; the zenith point and the rotation with respect to direction of north. The geometric calibration makes it possible to place the captured images on a map projection and find the geographical location of the aurora. More detailed geometric calibration would allow image distortion correction.

The intensity calibration equipment is shown in Figure 6. The setup consists of a dark-room, a uniform light source, an infrared (IR) filter (and ND (Neutral Density)-filters), a light shield

tube, and the all-sky camera. The uniform light source is an integrating sphere equipped with a reference detector for measuring the luminance of the sphere.

The IR-filter is used to block off the infrared end of the light source's spectrum. Due to the sensitivity of the imager light protection sensor to the infrared region of the light source's spectrum, the IR-filter is used to prevent the sensor from cutting the intensifier power at a too low a light level. The light shield tube is used because the dark room used proved to be not so dark in practice, partly due to the fact that the uniform light source gives off light also to the outside of the sphere. The tube prevents any external light from being detected by the camera system.

For the camera calibration the uniform light source is adjusted to a selected luminance value and several images are captured with each gain setting for each filter. From the captured image the recorded intensity is found by averaging the pixel values from a selected area of the image.

When the light source radiance dependence on the wavelength, the spectral radiance, is known as well as the transmittances of the filters, the relation between the source luminance and the recorded intensity can be found as a function of the exposure time.

By repeating the procedure with different luminance values it is possible to solve the measured intensity as a function of luminance and exposure time for each gain and filter setting. All the cameras can then be scaled to a same reference level with each filter and gain.

The geometric calibration of the ASCs is done using the positions of the stars to find the orientation of the cameras. In the geometric calibration stars are first identified and located from an image of a starry sky. For these stars the azimuth and the altitude are then calculated and these are then used to solve the position and the alignment of the camera.

In order to be able to convert the intensity values measured by the ASC into physical units, the light source has to be calibrated. The calibration was performed at Helsinki University of Technology (HUT) in the Metrology Research Institute which is the Finnish National Standards Laboratory for the measurement of optical quantities.

The light source was calibrated by measuring the source luminance with a luminance meter with a known luminance response and the source spectrum with a spectroradiometer with a known spectral response. The luminance response of the luminance meter can be traced to the

national luminance standard and the response of the spectroradiometer can be traced to the national standard of the spectral irradiance.

5 Conclusions

The ASC network of FMI has been operated now for more than 40 years. The maintenance operations were centralized to Arctic Research Centre at Sodankylä in 1999, and have been there since. The calibration procedure also takes place in Sodankylä, in co-operation between maintenance team and FMI Space Research unit. This article briefly reviews the operations related to the network maintenance.

The FMI ASC network is now operating smoothly, and FMI has remarkably long continuous time series of Auroral images. Even if the network is located into rather large physical area, the maintenance response time is relatively fast due to relatively closely located maintenance team. Therefore the proper operation of the network can be guaranteed all the time, the possible breaks of the imaging operations due to equipment failures are limited to 2-3 days.

The centralization of the large-area network maintenance into one essential location (from the network point of view) has been found to be an optimal solution in order to verify to operations in acceptable level. With the experience of 5 years (and 47 years altogether, although in the beginning there were no centralized maintenance) FMI Space Research and FMI Arctic Research Centre have proven their capability to handle the management and maintenance of described large-area camera network or any correspondent measurement networks.

Acknowledgements

Authors wish to thank Kirsti Kauristie and Osmo Aulamo for useful suggestions and needful support. We thank especially Dr. Mikko Syrjäsuo, whos original work is the very base of this paper.

References

- A. Brekke, "Physics of the upper polar atmosphere", John Wiley & Sons, 1997.
- F. Grum and R. J. Becherer, "Optical Radiation Measurements, Volume 1, Radiometry", Academic Press, Inc., 1979.
- H. J. Holma, K. Kaila and J. R. T. Jussila, "Temperatures, emission heights and energies in discrete auroral forms", *Phys. Chem. Earth (B)*, Vol. 25, nro 5-6, 2000, pp 463-466.
- J. R. Howell, "A catalog of radiation configuration factors", McGraw-Hill, Inc., 1982.
- K. Kaila and H. J. Holma, "Absolute calibration of photometer", *Phys. Chem. Earth (B)*, Vol. 25, nro 5-6, 2000, pp 467-470.
- KEO Consultants, "All-Sky Imaging System for Finnish Meteorological Institute, Instruction Manual", KEO Consultants, 1996.
- Labsphere, "Instruction Manual", Labsphere, 2000.
- S. Mäkinen, "All-Sky Camera Calibration", Master Thesis, Helsinki University of Technology, 2001, 87 pp.
- M.T. Syrjäso, "All-Sky Camera", Master Thesis, Helsinki University of Technology, 1996, 67 pp.
- M.T. Syrjäso, T.I. Pulkkinen, R.J. Pellinen, P. Janhunen, K. Kauristie, A. Viljanen, H.J. Opgenoorth, P. Karlsson, S. Wallman, P. Eglitis, O. Amm, E. Nielsen, and C. Thomas, "Observations of substorm electrodynamics using the MIRACLE network", *Proceedings of the International Conference on Substorms-4*, Editors: S. Kokubun and Y. Kamide, *Astrophysics and Space Science Library*, vol. 238, Terra Scientific Publishing Company/ Kluwer Academic Publishers, 1998, pp. 111-114.
- M.T. Syrjäso, "FMI All-Sky Camera Network", Geophysical Publications, Finnish Meteorological Institute, ISBN 951-697-543-7, ISSN 0782-6087, 2001, 34 pp.
- M.T. Syrjäso, "Auroral monitoring network: from all-sky camera system to automated image analysis", Doctoral Thesis at the Helsinki University of Technology, 2001
- P. Toivanen, J. Holvila, P. Kärhä and E. Ikonen, "Realization of the units of luminance and spectral radiance at the HUT", *Metrologia*, Vol. 37, 2000, pp. 527-530.

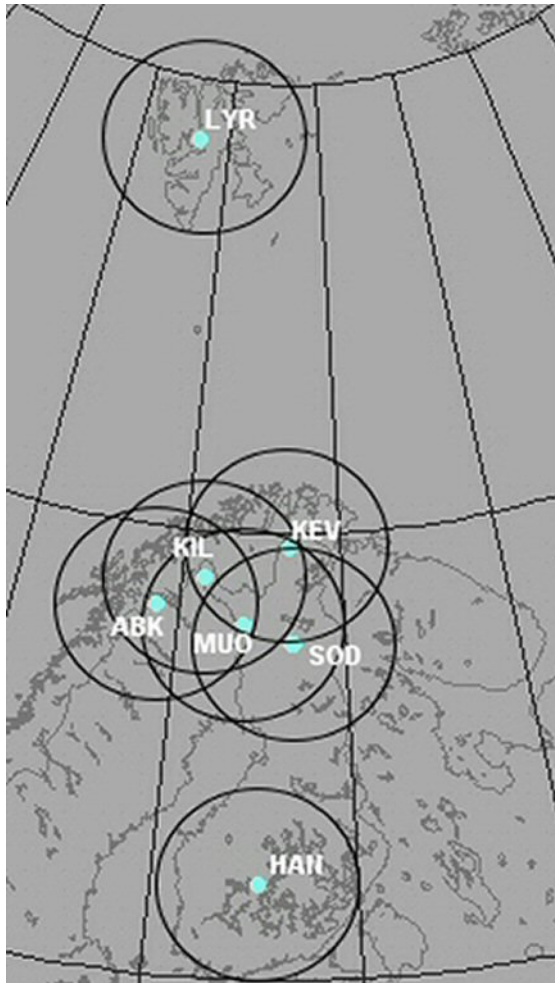


Figure 1. All-Sky Camera Network (the situation during the winter 2003-2004).

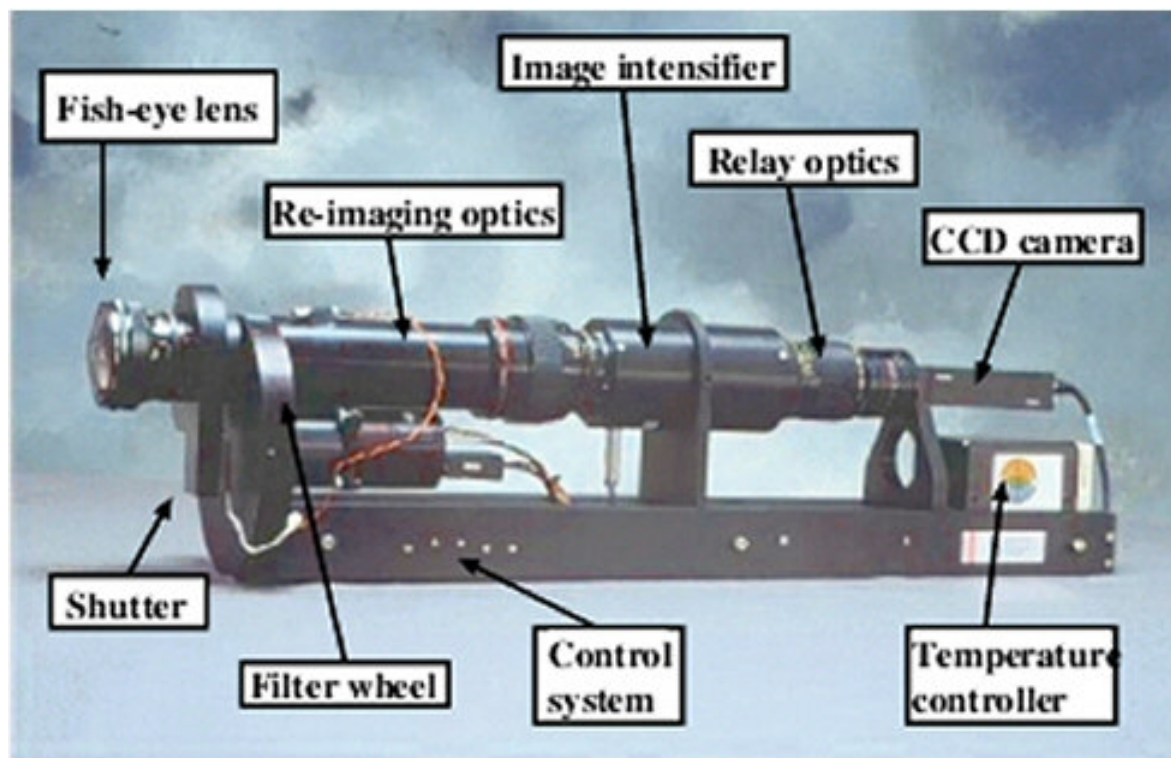


Figure 2. All-Sky Camera.

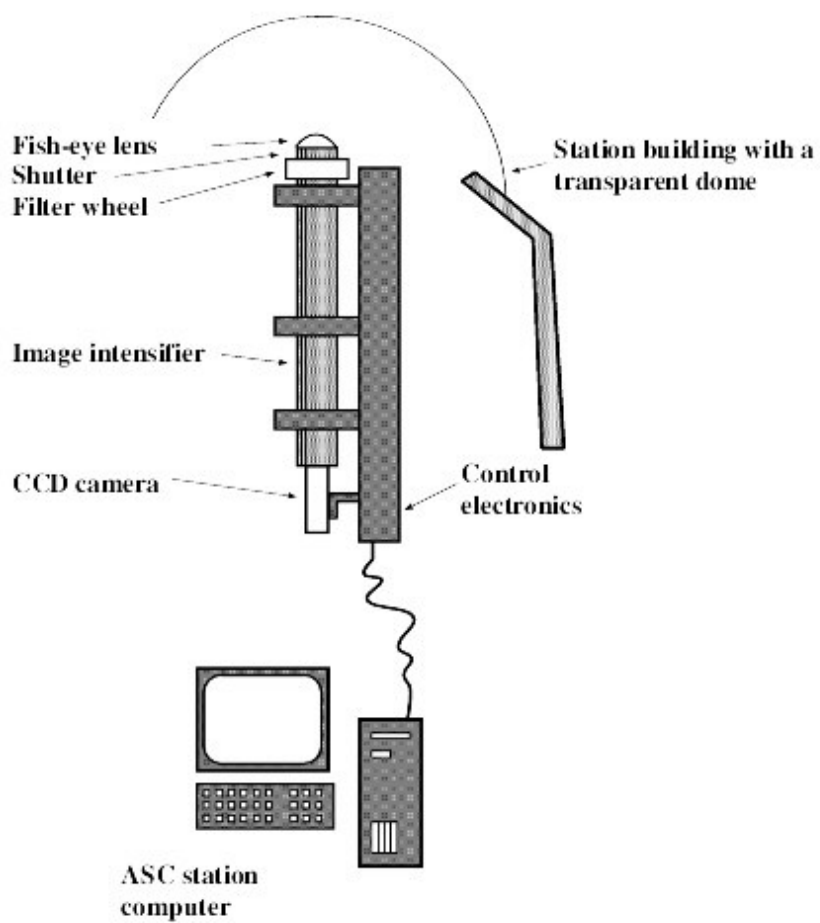


Figure 3. All-Sky Camera station overview.

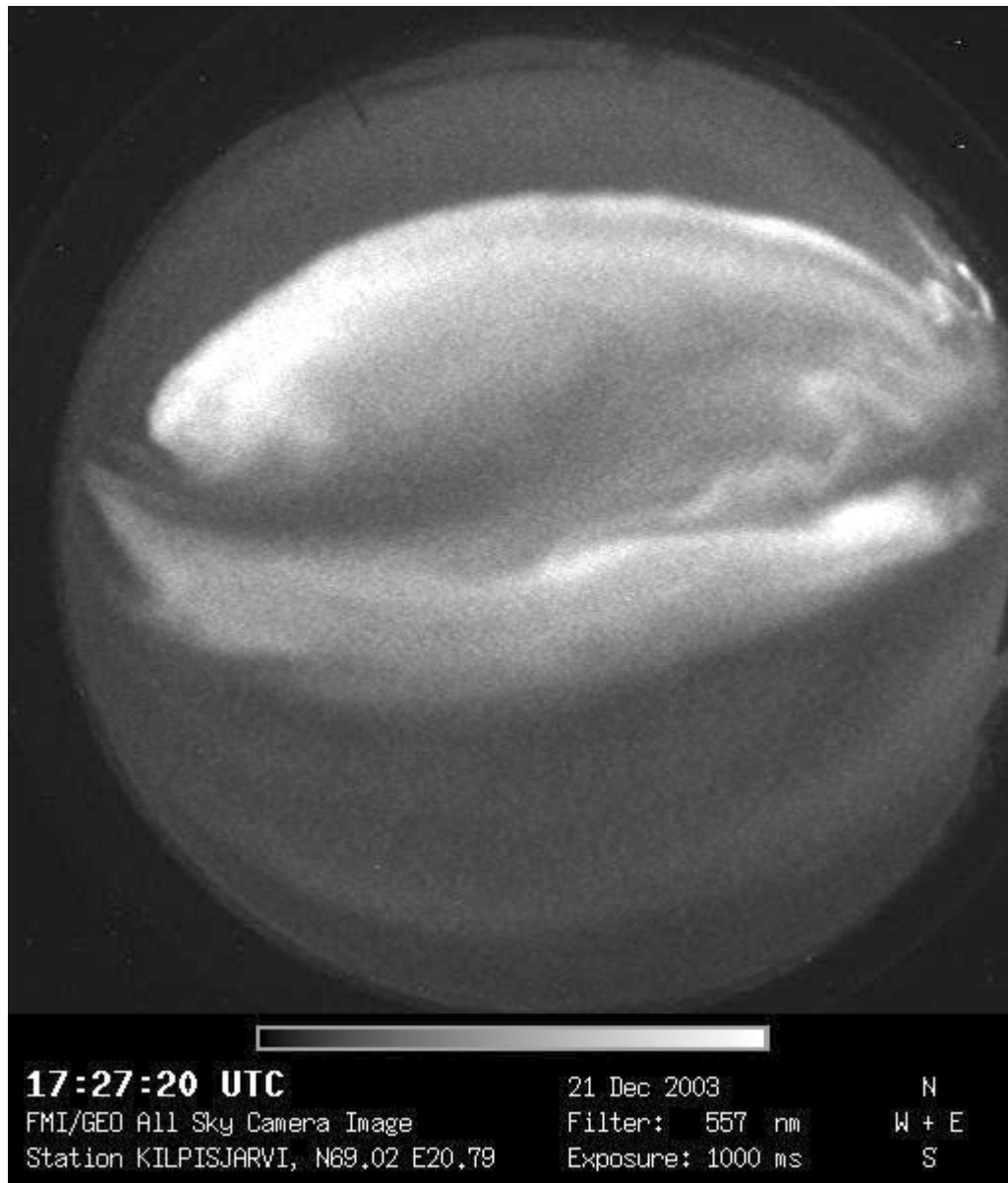


Figure 4. Example All-Sky Camera image (with green filter) from Kilpisjärvi, 21 December 2003.



Figure 5. The dark laboratory room.

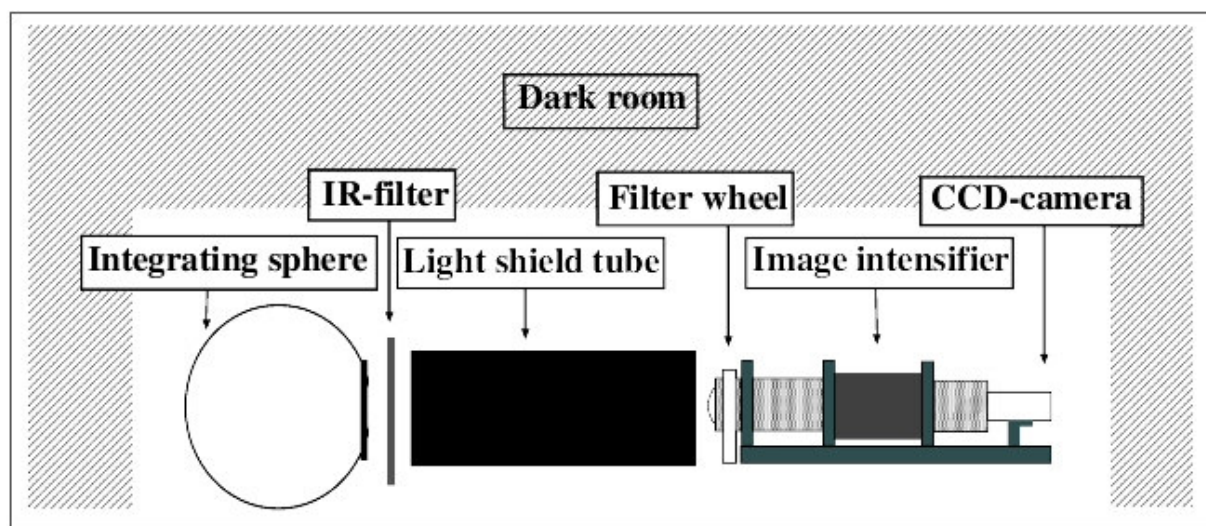


Figure 6. Calibration system in the dark laboratory.